Optical properties and photonic applications of molecular spin-crossover materials

Karl Ridier, Ayman Hoblos, Stéphane Calvez, Maciej Lorenc, William Nicolazzi, Saioa Cobo, L. Salmon, Lucie Routaboul, Gábor Molnár, Azzedine Bousseksou

To cite this version:

Karl Ridier, Ayman Hoblos, Stéphane Calvez, Maciej Lorenc, William Nicolazzi, et al.. Optical properties and photonic applications of molecular spin-crossover materials. Coordination Chemistry Reviews, 2025, 535, pp.216628. ⟨10.1016/j.ccr.2025.216628⟩. ⟨hal-05043620⟩

HAL Id: hal-05043620
https://hal.science/hal-05043620v1

Submitted on 24 Jul 2025

Coordination Chemistry Reviews 535 (2025) 216628

Contents lists available at ScienceDirect

Coordination Chemistry Reviews

journal homepage: www.elsevier.com/locate/ccr

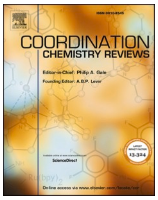

Optical properties and photonic applications of molecular spin-crossover materials

Karl Ridier [a,*], Ayman Hoblos [a], Stéphane Calvez [b], Maciej Lorenc [c], William Nicolazzi [a], Saioa Cobo [a], Lionel Salmon [a], Lucie Routaboul [a], Gábor Molnár [a], Azzedine Bousseksou [a,*]

[a] Laboratoire de Chimie de Coordination, CNRS UPR 8241, Université de Toulouse, 205 route de Narbonne, F-31077 Toulouse, France
[b] Laboratoire d'Analyse et d'Architecture des Systèmes, CNRS UPR 8001, Université de Toulouse, 7 avenue du colonel Roche, F-31400 Toulouse, France
[c] Univ. Rennes, CNRS, IPR (Institut de Physique de Rennes) – UMR 6251, F-35000 Rennes, France

ARTICLE INFO

Keywords:
Spin-crossover materials
Optical properties
Refractive index switching
Optical phase-change materials
Active photonic devices
Strong light-matter coupling

ABSTRACT

We review the current knowledge on the optical properties of molecular spin-crossover (SCO) materials, which exhibit reversible switching between low-spin and high-spin electronic configurations, as well as their use for practical applications in the fields of optics and photonics. We focus on the physical origins and magnitude of the complex refractive index change (both real and imaginary parts) in SCO materials, including a brief excursion to less-studied lower frequency ranges (THz–Hz). Until now, the optical property changes have primarily been used as a means of detection to characterize the SCO phenomenon itself (particularly at the nanometric scale) or to develop optical sensors for monitoring variations in an external stimulus. However, more recently, optical signal processing and modulation have also been explored using SCO nanomaterials as active elements in tunable photonic devices. Herein, we review the current state of the art of such functional devices, showing that molecular SCO compounds are emerging as a promising class of phase-change materials with high potential for specific active photonic applications, particularly in the visible spectral range. Key results on light-induced spin transitions and the photoswitching dynamics of SCO materials are also briefly reviewed in the context of photonic devices. Finally, the results of recent studies reporting strong light-matter coupling phenomena between SCO molecules and confined electromagnetic fields in resonant optical cavities are also discussed, with, in sight, the fascinating perspectives of manipulating the molecular properties using light.

1. A brief introduction to the spin-crossover phenomenon

The spin-crossover (SCO) phenomenon, which occurs in certain molecular complexes and coordination networks of transition metal ions, has been a subject of enduring interest in the fields of coordination chemistry and materials science. SCO compounds certainly constitute one of the most spectacular and fascinating examples of multifunctional, switchable molecular materials, attracting considerable attention for their potential in technological applications. The SCO phenomenon refers to the reversible change of electronic ground state, between the so-called low-spin (LS) and high-spin (HS) configurations, in certain octahedral transition metal ion complexes, which can occur through the application of a variety of external stimuli, including a temperature change, the application of an external pressure, light irradiation, intense magnetic field, electrical current, or even via the adsorption/desorption of gas/vapor molecules [1,2]. In synthetic systems, the SCO phenomenon has been observed since the 1930s when Cambi and coworkers first discovered anomalous magnetic behaviors in Fe^{3+} dithiocarbamate derivatives [3,4]. Since then, the field of SCO research has continued to grow, attracting the interest of chemists, physicists, and theoreticians, as indicated by the increasing number of articles, reviews [5–9], and books [10,11] on the topic.

The SCO phenomenon occurs in certain (pseudo-)octahedral transition metal ion complexes with $3d^4$–$3d^7$ electronic configurations (i.e., Co^{2+}, Co^{3+}, Fe^{2+}, Fe^{3+}, Mn^{2+}, Mn^{3+}, and Cr^{2+}), which are characterized by two low-lying electronic states, close in energy, with different spin multiplicities referred to as the low-spin (LS) and high-spin (HS) states. As can be inferred from ligand field theory [12], these two stable states arise from the fact that two equilibrium configurations are possible for populating the *d* orbitals of the central metal ion. Indeed, as displayed in Fig. 1a, under the perturbation of an octahedral ligand field, the five *d* orbitals of the transition metal ion are split into a low-lying energy

---

* Corresponding authors.
E-mail addresses: karl.ridier@lcc-toulouse.fr (K. Ridier), azzedine.bousseksou@lcc-toulouse.fr (A. Bousseksou).

https://doi.org/10.1016/j.ccr.2025.216628
Received 22 December 2024; Received in revised form 7 March 2025; Accepted 9 March 2025

level, t_{2g}, consisting of a subset of three non-bonding degenerate orbitals (d_{xy}, d_{xz}, and d_{yz}) and a high-lying energy level, e_g, comprising two anti-bonding degenerate orbitals (d_{z2} and d_{x2-y2}). The energy gap between these two levels, which characterizes the strength of the ligand field, is referred to as the ligand field splitting energy, $\Delta_O = E(e_g) - E(t_{2g})$. This quantity is often denoted $10Dq$, where Dq is a parameter that depends on the radial electron density of the d electrons, the charge of the metal ion, and the average metal-ligand distance as $1 / r^n$ (n = 5–6) [12]. Thus, the ligand field strength depends on the specific set of ligands and metal ion, and also (for a given combination of ligands and metal ion) upon the metal-ligand distance.

Due to the partial degeneracy splitting of the d orbitals, two extreme cases can be envisaged for populating the t_{2g} and e_g subshells, depending on the competition between the ligand field strength, $10Dq$, which forces electrons to fill the low-lying t_{2g} level, and the electron-electron repulsion, often represented by the spin-pairing energy Π, which causes electrons to occupy the d orbitals according to Hund's rule. These opposing effects lead to the emergence of two possible ground states. If $10Dq$ is large compared to Π (strong ligand field case), as many electrons as possible will pair up in the t_{2g} subshell, resulting in the so-called LS ground state. On the other hand, if $10Dq$ is small compared to the electron-electron repulsion (weak ligand field case), then electrons will occupy both the t_{2g} and e_g orbitals in a way that maximizes the spin multiplicity, resulting in the HS ground state. As schematically shown in Fig. 1a, in the most widespread case of Fe^{2+} complexes, this competition can result in either a diamagnetic ($S = 0$) LS ground state ($t_{2g}^6 e_g^0$), with the molecular term symbol $^1A_{1g}$, or a paramagnetic ($S = 2$) HS ground state ($t_{2g}^4 e_g^2$), denoted as $^5T_{2g}$.

A thermally induced spin conversion between the LS and HS states is possible only if these two states are sufficiently close in energy. This condition is fulfilled when the zero-point energy difference between the two states, $\Delta E_{HL} = E_{HS} - E_{LS}$, is positive and typically lies between 0 and 2000 cm^{-1} (i.e., comparable to the thermally accessible energy, k_BT). (Note that for higher values of ΔE_{HL} (> 2000 cm^{-1}), the HS state may become thermally inaccessible at temperatures that guarantee the structural integrity of the compound.) In the specific case of Fe^{2+} complexes, it has been shown that, for ΔE_{HL} to be of the order of thermal energies, the ligand field strengths must be significantly different in the two spin states, with $10Dq^{LS}$ = 19,000–22,000 cm^{-1} in the LS state and $10Dq^{HS}$ = 11,000–12,500 cm^{-1} in the HS state (see Fig. 1a) [12]. Under these conditions, at elevated temperatures, the HS state may become the thermodynamic ground state due to its higher entropy, $\Delta S_{HL} = S_{HS} - S_{LS} > 0$, which results from a greater spin multiplicity and a higher vibrational density of states [13]. Calorimetric measurements indeed show that the total entropy change between the HS and LS states, ΔS_{HL}, typically ranges from 40 to 90 J K^{-1} mol^{-1} for the vast majority of SCO compounds [13–16].

As a matter of fact, the change of the molecular ground state from the LS to the HS state is accompanied by a drastic decrease in the ligand field strength (by a factor of ~1.75), which is associated with a significant increase in the metal-ligand distance r, according to the relation:

$$\frac{10Dq^{LS}}{10Dq^{HS}} = \left(\frac{r_{HS}}{r_{LS}}\right)^n \tag{1}$$

where n = 5–6 [12]. As an example, in the case of the most widespread $Fe^{2+}N_6$ coordination core, the length of the Fe-ligand bonds exhibits a substantial elongation of ~10 %, increasing from 1.95–2.00 to 2.10–2.20 Å ($\Delta r_{HL} = r_{HS} - r_{LS} \approx 0.2$ Å) when switching from the LS to the HS state [17]. This dramatic increase in r is understandable since the HS state is characterized by a greater occupancy of the anti-bonding e_g orbitals. Such a drastic modification of $10Dq$ upon the spin-state switching has also important consequences on the optical properties of SCO compounds. Indeed, for many transition metal coordination complexes, the ligand-field transitions between d orbitals of the metal ion occur in the visible spectrum, which gives the compounds their color. For this reason, the spin-state transition is often accompanied by a noticeable color change of the material.

In a sense, the SCO phenomenon can be considered as an example of bond-stretch isomerization reaction [18], i.e., a 'chemical' equilibrium between two (LS and HS) isomeric molecular forms, which essentially differ in the length of the metal-ligand bonds. This bond length, r, thus constitutes the most relevant nuclear coordinate to describe the equilibrium between the two spin states. As shown in Fig. 1b, SCO systems can be described by a ground-state potential energy surface, which displays two local minima (close in energy) as a function of the average metal-ligand distance, corresponding to the two stable LS and HS states. The two potential wells are displaced relative to each other, both horizontally (by Δr_{HL}) and vertically (by ΔE_{HL}), and they are separated by an intramolecular potential energy barrier, which arises from the large difference in metal-ligand bond length between the two spin states.

Importantly, the LS and HS states are also characterized by a significant difference in the volume of the material. This difference primarily arises from the substantial elongation of the metal-ligand bond lengths when switching from the LS to the HS state (up to 10 % in the case of Fe^{2+} complexes), which results in a notable swelling of the volume of the coordination octahedron by ~25 % [15,17]. As a consequence, the difference in unit-cell volume, $\Delta V_{HL} = V_{HS} - V_{LS}$, between the LS and HS phases (which reflects the macroscopic change) is always noteworthy, even though it can vary considerably from one SCO material to another [19]. For most SCO compounds, the relative change in unit-cell volume, $\Delta V_{HL} / V_{LS}$, typically ranges from 1 % to 10 % [19–21], although it can sometimes reach higher values, up to 22 % [22]. As we will discuss later, this significant macroscopic volume change has also important consequences on the optical properties of SCO materials, particularly with regard to the evolution of the refractive index in the

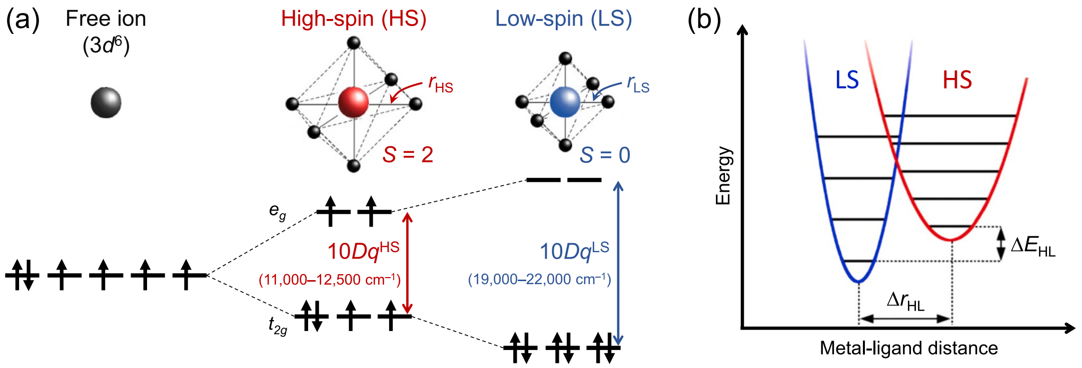

Fig. 1. (a) HS and LS electron configurations of an octahedral $3d^6$ SCO complex. (b) Schematic configurational diagram of a SCO system at $T = 0$ and $p = 0$, showing the potential wells of the LS and HS states in the harmonic approximation along the symmetric metal-ligand stretching coordinate. The LS and HS electronic states are separated in energy by ΔE_{HL}.

visible spectrum upon the molecular spin-state switching.

Depending on the temperature, which promotes the HS state due to its higher entropy, and the pressure, which stabilizes the LS state due to its reduced volume, the thermodynamic ground state can be either the HS or the LS state. The considerable changes in entropy (ΔS_{HL}) and volume (ΔV_{HL}) are, respectively, the driving forces of the thermally induced and pressure-induced spin-state conversion. From basic thermodynamic considerations [23], the transition temperature, $T_{1/2}$, defined as the temperature at which the proportion of molecules in the LS and HS states within the system is statistically the same, is given by:

$$T_{1/2} = \frac{\Delta E_{HL} + p\Delta V_{HL}}{\Delta S_{HL}} = \frac{\Delta H_{HL}}{\Delta S_{HL}} \tag{2}$$

where $\Delta H_{\mathrm{HL}} = H_{\mathrm{HS}} - H_{\mathrm{LS}} = \Delta E_{\mathrm{HL}} + p\Delta V_{\mathrm{HL}}$ is the enthalpy change of the system when going from the LS to the HS state. ΔH_{HL} corresponds to the energy gap between the LS and HS states at external pressure p and zero temperature. Note that at atmospheric pressure, the term $p\Delta V_{\mathrm{HL}}$ is generally small compared to ΔE_{HL}, so that $\Delta H_{\mathrm{HL}} \approx \Delta E_{\mathrm{HL}}$. The equilibrium temperature $T_{1/2}$ is thus a measure of the zero-point energy difference, ΔE_{HL}, between the two states. For a complex exhibiting SCO at room temperature ($T_{1/2} \approx 300$ K), the zero-point energy difference between the HS and LS ground states is typically of the order of $\Delta E_{\mathrm{HL}} \approx 1500$ cm^{-1} [24]. As indicated in Eq. (2), the application of an external pressure can significantly modify the switching temperature, with a typical rate of $\Delta V_{\mathrm{HL}} / \Delta S_{\mathrm{HL}} \approx$ 10–20 K kbar^{-1}.

The transition between the LS and HS molecular states can also occur under steady thermodynamic conditions (where one state is stable and the other metastable), through light irradiation. This phenomenon is exemplified by the well-studied light-induced excited spin-state trapping (LIESST) effect, whereby the metastable HS state can be efficiently populated by irradiating the sample with light of an appropriate wavelength, tuned to specific metal-centered absorption bands of the LS species. The first observations of the LIESST effect were reported in 1982 by McGarvey and Lawthers [25] in Fe^{2+} SCO compounds in solution, and later in 1984 in solid-state materials by Decurtins et al. [26]. Undoubtedly, the discovery of this effect marked a turning point in the SCO field, allowing for major advances in understanding the fundamental mechanisms underlying the LS/HS switching process [27,28], and opening up exciting prospects for using SCO complexes in ultrafast, optically addressed switching devices as well.

Although the SCO phenomenon is innately a molecular-level process, it appears that the manifestation of this phenomenon is largely influenced by interactions between molecules. Indeed, in solid-state materials, collective effects are known to arise from the complex interplay of short- and long-range elastic interactions between SCO molecules in different spin states. These interactions, mediated by the crystal lattice, result from the significant change in molecular volume, as well as the drastic modifications in elastic constants (i.e., lattice stiffness) that accompany the spin-state switching [29]. In the SCO field, these collective effects are usually referred to under the general concept of *cooperativity* [30]. The physical origins of these cooperative effects have been successfully described using continuum elasticity theory [31,32], and many microscopic models have also been developed to conceptualize the mechanisms of elastic intermolecular interactions [33]. It is noteworthy that in nanoscale SCO materials, in addition to the cooperative effects between neighboring metal centers, the influence of surface/interface properties needs also to be taken into account [8,34]. Overall, all these effects lead to modifications in the thermodynamic stability between the LS and HS phases, as well as in the dynamics of the switching process. As such, the thermally induced SCO process between the LS and HS states may take different forms, ranging from gradual spin conversions in weakly cooperative systems (e.g., regular solutions, diluted solids), characterized by a homogeneous and progressive transformation of the material, to genuine first-order spin transitions in highly cooperative solids, which are abrupt and accompanied by hysteresis (memory effect) and phase separation phenomena [35]. Undeniably, the possibility of a molecular memory effect working at room temperature has been a major driving force behind SCO research in recent decades [36].

An important characteristic of SCO compounds is that the spin-state switching event is accompanied by significant changes in nearly all the physical properties of the material. These highly tunable properties of SCO materials make them attractive for a broad range of practical applications, which require smart, functional materials as sensors, actuators, displays, switches, and information storage devices [7,8,37]. Particularly, in addition to changes in magnetic (magnetic susceptibility), thermal (heat capacity), and mechanical (elastic constants) properties, SCO materials are known to exhibit significant changes in their optical properties. Among these, the most spectacular and well-known property is, undoubtedly, the color change of SCO materials accompanying the molecular spin-state switching. This property was used in the very first SCO-based applications developed by Kahn et al. [38,39] more than 30 years ago, which consisted in information storage and optical display devices. Since then, several application ideas (mainly for optical sensing purposes) have been proposed and developed by researchers. On the other hand, less well recognized is the concomitant change in the refractive index of SCO materials across wide spectral ranges. Although less well studied, this property opens up interesting prospects for manipulating and modulating light propagation in switch-type devices, particularly at nanometric scales where the color change contrast of SCO materials often becomes negligible.

In this review, we provide a state-of-the-art overview of current knowledge on the optical properties of SCO materials, focusing on changes in both the optical absorption properties – i.e., the imaginary part of the complex refractive index – as well as the real part, across different spectral ranges. We highlight the use of these optical changes for detection applications, not only for probing the SCO phenomenon itself, but also for the development of various optically readable sensors. Additionally, we present an overview of the current applications of optical property changes in the recent development of SCO-based photonic switching devices within the emerging field of active photonics, with particular emphasis on photoinduced spin transitions, which are of paramount importance for the realization of all-optical switches. Finally, we extend this review to the intriguing phenomenon of strong light-matter coupling in resonant optical cavities, which opens up fascinating perspectives in the field of polaritonic chemistry for manipulating molecular properties through confined light modes. As a guide for the reader, the structures of the ligands for all SCO compounds referenced in this article are provided in the Supplementary Material (Fig. S1).

2. Optical properties of spin-crossover materials

2.1. The complex refractive index: Definition and basic concepts

One of the most remarkable properties of the SCO phenomenon is the change in the complex refractive index of the material, defined as:

$$n^* = n + ik \tag{3}$$

upon the molecular spin-state switching. This modification involves changes in both the real part of n^*, referred to as the refractive index (n), and the imaginary part (k), known as the extinction coefficient. In optics, the complex refractive index is a macroscopic, dimensionless quantity that governs the characteristics of light propagation in a given medium. Briefly, the electric field $\boldsymbol{E}$ associated with electromagnetic radiation of frequency ω, propagating in a medium with a complex refractive index n^* along the positive z-axis, can be expressed as a monochromatic plane wave, which can be represented in complex exponential form as:

$$\boldsymbol{E} = \boldsymbol{E}_0 exp\left[-i\omega\left(t - \frac{n^*}{c}z\right)\right] \tag{4}$$

where i is the imaginary unit ($i^2 = -1$), c is the speed of light in vacuum, $\boldsymbol{E}_0$ is the amplitude of the propagating wave, and t is the time. Note that the angular frequency ω and the wavelength (in vacuum) λ_0 of the electromagnetic radiation are linked by the relationship:

$$\omega = \frac{2\pi c}{\lambda_0} \tag{5}$$

If we neglect any magnetic interactions between the medium and the magnetic field of the radiation (which is generally a good approximation for non-ferromagnetic or ferrimagnetic materials), the complex refractive index that appears in Eq. (4) is directly related to the complex relative permittivity of the material ε_r* by the relation:

$$(n^*)^2 = \varepsilon_r^* \tag{6}$$

where ε_r* is a complex number that can be expressed in the general form:

$$\varepsilon_r^* = \varepsilon_r' + i\varepsilon_r'' \tag{7}$$

The real part of ε_r*, also known as the dielectric constant, quantifies the ability of a material to acquire polarization density, and thus store electric energy, in response to an applied electric field. This property is related to the intrinsic microscopic polarizability of atoms and molecules. The imaginary part, ε_r", corresponds to a phase shift of the polarization density $\boldsymbol{P}$ relative to $\boldsymbol{E}$. This phase shift causes a certain amount of electromagnetic energy to be dissipated as the wave propagates through the medium, resulting in attenuation of the traveling fields. According to Eq. (6), the real and imaginary parts of n* and ε_r* are linked by the following relationships:

$$\varepsilon_r' = n^2 - k^2 \tag{8}$$

$$\varepsilon_r'' = 2nk \tag{9}$$

These relations can also be inverted to express n and k as functions of ε_r' and ε_r":

$$n = \sqrt{\frac{1}{2}\left(\sqrt{\varepsilon_r'^2 + \varepsilon_r''^2} + \varepsilon_r'\right)} \tag{10}$$

$$k = \sqrt{\frac{1}{2}\left(\sqrt{\varepsilon_r'^2 + \varepsilon_r''^2} - \varepsilon_r'\right)} \tag{11}$$

Substituting Eq. (3) into Eq. (4), the complex exponential form of the electric field becomes:

$$\boldsymbol{E} = \boldsymbol{E}_0 exp\left(-\frac{\omega k}{c}z\right) exp\left[-i\omega\left(t - \frac{n}{c}z\right)\right] \tag{12}$$

It is immediately apparent from Eq. (12) that the real part of n* affects only the phase of the light wave propagating through the medium, while the imaginary part, k, affects only its amplitude. As indicated in Eq. (12), the radiation propagates in the material with a phase velocity v_ϕ, which is no longer equal to c, as in vacuum, but rather c / n. Thus, the refractive index (real part) can be seen as the factor by which the phase velocity (and the wavelength) of the electromagnetic radiation is reduced with respect to its value in vacuum:

$$n = \frac{c}{v_\phi} \tag{13}$$

The refractive index is a dimensionless, macroscopic quantity that describes how the phase of a light wave is altered as it propagates through the material. More specifically, Eq. (12) shows that any variation in the refractive index of a material, Δn, over a path length ℓ, results in a change in the optical phase, $\Delta\phi$, of the propagating wave, given by:

$$\Delta\phi = \frac{\omega\ell\Delta n}{c} = \frac{2\pi\ell\Delta n}{\lambda_0} \tag{14}$$

Thus, any change in the refractive index of a medium allows for the modulation of the phase of electromagnetic waves propagating through it, thereby also affecting all related interference and diffraction phenomena.

From a microscopic point of view, the refractive index arises from the polarization of atoms and molecules by the electric field of the incident optical wave. The primary effect of the propagating radiation is indeed exerted by the electric field, which causes the electric charges in the medium to oscillate at the same frequency as the light wave. These oscillating charges (or dipoles) subsequently produce a new electromagnetic field (the secondary field) that oscillates at the same frequency as the primary wave but with a phase delay. As a result, the light wave traveling through the medium, which is the macroscopic superposition of all the waves radiated by the moving charges, propagates with a phase velocity reduced by a factor n (the refractive index) compared to the phase velocity of the same wave in vacuum. Importantly, both n* and ε_r*, which characterize the response of a material in terms of polarization density, depend on the frequency ω (or equivalently, the wavelength λ_0) of the incident field. This frequency dependence simply reflects the fact that a material cannot polarize instantaneously in response to an applied field, but does so with a certain time delay. This phenomenon is known as dispersion. Since the refractive index dictates the phase velocity of the optical wave within the medium, this dispersion property implies that the phase velocity of the radiation also depends on its frequency. Finally, it is important to note that the refractive index also determines the amount of light that is transmitted or reflected at the interface between two media. The ratio of reflected to transmitted light is described by the so-called Fresnel coefficients, which depend on the refractive indices of the two media, as well as the incident angle and the polarization of the incoming wave.

While the real part of n* affects the phase of light radiation, the imaginary part, k, influences the amplitude of the electromagnetic wave propagating through the material and quantifies the amount of attenuation due to optical absorption. As shown in Eq. (12), the amplitude of the light wave decreases exponentially as it propagates, following exp ($-\omega kz/c$). Consequently, the intensity I of the electromagnetic radiation (sometimes also called irradiance), which is proportional to the square of the amplitude of the electric field, varies as:

$$I(z) = I_0\left[exp\left(-\frac{\omega k}{c}z\right)\right]^2 = I_0 exp(-\alpha z) \tag{15}$$

where I_0 is the intensity of the incident light (at $z = 0$), and α is the absorption coefficient of the material (with units of inverse length, typically expressed in cm^{-1}). As indicated in Eq. (15), the absorption coefficient α is directly related to the extinction coefficient, k, through the following relationship:

$$\alpha = \frac{2\omega k}{c} = \frac{4\pi k}{\lambda_0} \tag{16}$$

Note that, instead of the absorption coefficient α, some authors prefer using the molar absorption coefficient ε (in L mol^{-1} cm^{-1}), sometimes also referred to as the molar extinction coefficient, which is defined by:

$$\varepsilon = \frac{\alpha}{C} \tag{17}$$

where C (in mol L^{-1}) is the molar concentration of absorbing species in the material. The relationship expressed in Eq. (15) is known as the Beer-Lambert law. This relation indicates that the intensity of light radiation decreases exponentially as it propagates through the material because the wave concedes part of its energy to the medium via optical absorption. It is important to note that this relationship neglects all other sources of wave attenuation, such as reflection or scattering. Moreover, it is important to stress that deviations from the Beer-Lambert law can occur in non-homogeneous media or in cases of high concentrations of absorbing species.

The ratio of transmitted to incident light intensity through a sample with a path length ℓ is called transmittance T, and, according to the Beer-Lambert law, it is given by:

$$T = \frac{I(\ell)}{I_0} = exp(-\alpha\ell) \tag{18}$$

Since transmittance diminishes exponentially with the thickness of the studied sample, another commonly used quantity of interest, called absorbance A (or sometimes optical density), is defined as the logarithm of T, such that:

$$A = -log_{10}(T) = \frac{\alpha\ell}{ln(10)} \tag{19}$$

As indicated in Eq. (19), absorbance A is a dimensionless quantity, which is directly proportional to the sample thickness and the absorption coefficient (i.e., the concentration of absorbing species). Let us mention that in certain fields, such as telecommunications or electronics, transmission is often expressed in logarithmic units of decibels (dB). This quantity is related to transmittance, T, and absorbance, A, by the formula:

$$T_{dB} = 10\ log_{10}(T) = -10A \tag{20}$$

Attenuation (or transmission loss) in dB is then simply given by $A_{\mathrm{dB}} = -T_{\mathrm{dB}}$. Therefore, an attenuation of X dB corresponds to a decrease in light intensity by a factor of $10^{\mathrm{X}/10}$.

From a microscopic point of view, optical absorption arises from the emergence of a phase shift between the induced dipole moments in the medium and the exciting field (absorption is maximum when the two are in phase quadrature). However, this phase shift, which results from the non-instantaneous response of the medium, is intrinsically linked to the phenomenon of dispersion, i.e., the dependence of n on the frequency ω. Thus, there is an inherent connection between the phenomena of dispersion and absorption in the medium, i.e., between $n(\omega)$ and $k(\omega)$. In fact, it can be shown that the real and imaginary parts of the complex refractive index are analytically related through the Kramers-Kronig dispersion relations [40]:

$$n(\omega) = n_\infty + \frac{2}{\pi} P \int_0^\infty \frac{\Omega\, k(\Omega)}{\Omega^2 - \omega^2} d\Omega \tag{21}$$

$$k(\omega) = -\frac{2\omega}{\pi} P \int_0^\infty \frac{n(\Omega) - n_\infty}{\Omega^2 - \omega^2} d\Omega \tag{22}$$

where P denotes the Cauchy principal value of the integral (which is a method for assigning values to integrals at singularities), Ω is the angular frequency running through the whole integration range, and n_∞ is the high-frequency refractive index. The Kramers-Kronig relations can be employed to determine the spectral variation of the refractive index $n(\omega)$ from a measured absorption spectrum (over a broad spectral range), and vice versa. However, note that, in practice, it is only possible to measure the absorption spectrum over a finite range of frequencies. As such, n_∞ is not necessarily equal to unity depending on the spectral range considered.

2.2. *Changes in optical absorption of spin-crossover materials*

As the SCO phenomenon involves a change in the electronic ground state, and thereby a significant modification of the electronic density of states (DOS) of the compound, an appealing feature of the spin transition is the concomitant, substantial change in the electronic absorption spectrum of the material in the UV–vis-NIR domains. Indeed, most SCO compounds exhibit specific electronic absorption bands in these spectral ranges, associated with ligand-field and/or charge-transfer (metal-to-ligand or ligand-to-metal) transitions, which appear at different wavelengths in the LS and HS states [28]. As a consequence, one of the most spectacular and well-known properties of the spin transition is the perceptible color change of the material, a property which is referred to as thermochromism, piezochromism, magnetochromism or photochromism (depending on whether the SCO is triggered thermally, by an applied pressure, a magnetic field, or light irradiation, respectively).

The color change is a characteristic feature of all types of SCO compounds, but it is particularly well characterized for the vast family of Fe^{2+} SCO complexes [1,41]. As an example, Fig. 2 presents the absorption spectra of a single crystal of the widely known compound $[Fe(ptz)_6](BF_4)_2$ in both spin states [42], as well as photographs of the crystal showing the corresponding color change, from pink in the LS state to colorless in the HS state [28]. In the LS state, the spectrum exhibits two spin-allowed ligand-field absorption bands, $^1A_{1g} \rightarrow {}^1T_{1g}$ and $^1A_{1g} \rightarrow {}^1T_{2g}$ (see Fig. 2a), the former appearing in the visible range (18,200 cm^{-1}, $\lambda_0 \approx 550$ nm), while the latter is in the UV region (26,400 cm^{-1}, $\lambda_0 \approx 380$ nm). Therefore, as the crystal in the LS state predominantly absorbs green light from the visible spectrum, it appears in the complementary color, i.e., pink (Fig. 2b). When switching the crystal into the HS state, the spectrum features only one ligand-field absorption band in the NIR region (11,800 cm^{-1}, $\lambda_0 \approx 850$ nm), corresponding to the spin-allowed $^5T_{2g} \rightarrow {}^5E_g$ transition. Since no significant absorption occurs in the visible range in the HS state, the crystal appears colorless.

These absorption bands are referred to as ligand-field (*d*–*d*) bands because they involve direct transitions between the split *d* orbitals of the metal ion. Consequently, the significant spectral modifications of these *d*–*d* transitions upon the SCO are directly related to the substantial change in the ligand field strength (10*Dq*) of the complex. In fact, the energy difference between the $^5T_{2g}$ ($t_{2g}^4e_g^2$) and ^5E_g ($t_{2g}^3e_g^3$) states directly gives the ligand field strength of HS molecules, i.e., $10Dq^{HS} = E(^5E_g) - E(^5T_{2g}) = 11{,}800\ cm^{-1}$ in the case of $[Fe(ptz)_6](BF_4)_2$ [42]. As the HS-to-LS switching is accompanied by a dramatic increase of 10*Dq*, ligand-field transitions generally appear at higher energies in the LS state. For LS Fe^{2+} complexes, the ligand field strength can be estimated from the energy levels of the $^1T_{1g}$ and $^1T_{2g}$ states through the formula $10Dq^{LS} = E(^1T_{1g}) - E(^1A_{1g}) + \{E(^1T_{2g}) - E(^1T_{1g})\}\ /\ 4$, giving $10Dq^{LS} \approx 20{,}200\ cm^{-1}$ for $[Fe(ptz)_6](BF_4)_2$ [42]. As an illustration, the values of the 10*Dq* parameter in the two spin states of the compound $[Fe(ptz)_6](BF_4)_2$ are indicated in the Tanabe-Sugano diagram for an Fe^{2+} ($3d^6$) ion (Fig. 2c). This diagram depicts the electronic energy of the excited ligand-field states relative to the ground state, plotted as a function of the octahedral ligand field strength, 10*Dq*. The energies are expressed in units of the Racah parameter ($B \approx 740\ cm^{-1}$ for $[Fe(ptz)_6](BF_4)_2$ [28]), which quantifies the electron-electron repulsion energy. For each spin state, the observed ligand-field transitions are indicated by vertical arrows.

It is important to notice that, regardless of the transition metal ion considered, the occurrence of the thermally induced SCO phenomenon is expected only for a narrow range of ligand field strengths. Consequently, the color (change) of SCO compounds generated by ligand-field transitions is often similar for a given metal ion. As discussed by Hauser [28], the expected range of ligand field strengths and the nature of the spin-allowed *d*–*d* transitions in the visible spectral range (listed in Table 1) can be predicted on the basis of the Tanabe-Sugano diagram associated with each SCO-active metal ion [43,44]. As such, the energy of these transitions, and the resulting color, can also be predicted to a good approximation. Interestingly, it turns out that SCO complexes generally exhibit fewer ligand-field *d*–*d* transitions (which are likely to appear in the visible spectrum) in the HS state compared to the LS state (Table 1). This is because the number of accessible electronic states is generally lower for high spin multiplicities. Consequently, as a rule of thumb, SCO complexes often appear less intensely colored in the HS state than in the LS state. This trend is commonly observed in the wide

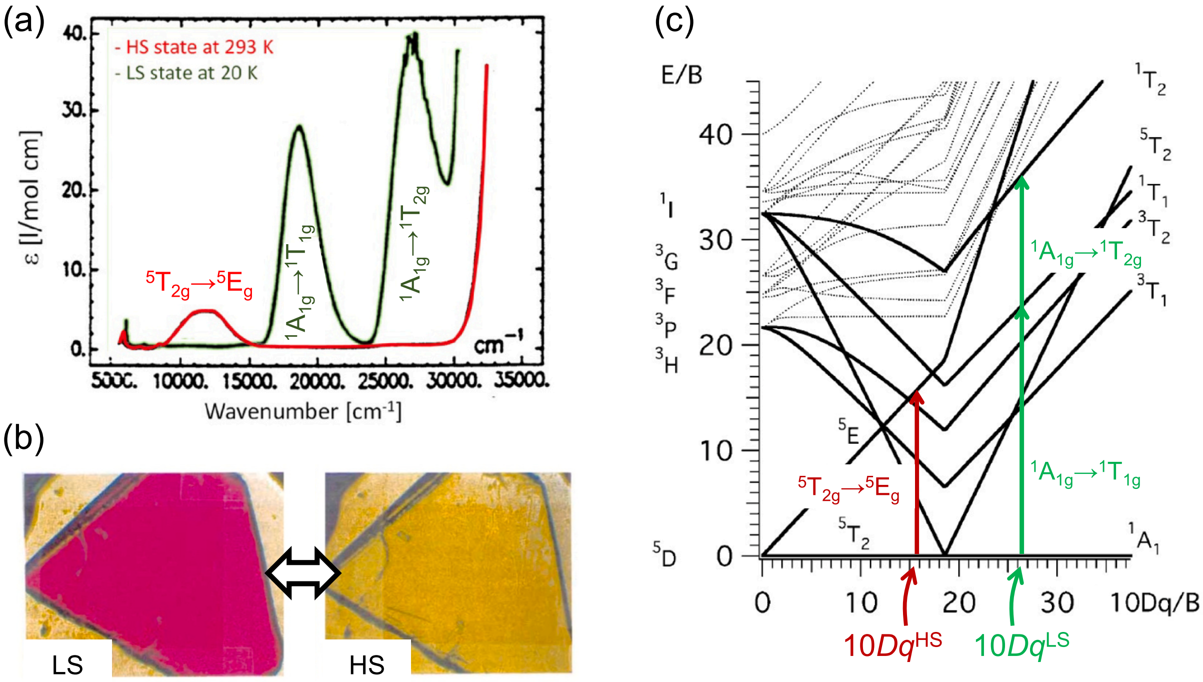

Fig. 2. (a) Optical absorption spectra of a single crystal of the Fe^{2+} SCO complex $[Fe(ptz)_6](BF_4)_2$ at 20 K (LS state) and 293 K (HS state). (b) Photographs of the single crystal in the two spin states, showing the color change from pink in the LS state (*left*) to colorless in the HS state (*right*). Adapted with permission from Ref. [28]. (c) Tanabe-Sugano diagram for an Fe^{2+} ($3d^6$) ion, showing the energy *E* of the excited ligand-field states relative to the ground state as a function of the ligand field strength 10*Dq*. Both *E* and 10*Dq* are expressed in units of the Racah parameter *B*. The vertical arrows indicate the ligand-field transitions observed for the compound $[Fe(ptz)_6](BF_4)_2$ in the two spin states and the corresponding value of 10*Dq*. Adapted with permission from Ref. [12]. (For interpretation of the references to color in this figure legend, the reader is referred to the web version of this article.)

Table 1

Lowest-lying, spin-allowed ligand-field transitions for octahedral d^4–d^7 complexes in their LS and HS states, extracted from the Tanabe-Sugano diagrams associated with each metal ion [44], which are expected to occur in the visible spectral range.

d^4 (Cr^{2+}, Mn^{3+})		d^5 (Mn^{2+}, Fe^{3+})		d^6 (Fe^{2+}, Co^{3+})		d^7 (Co^{2+})	
LS	**HS**	**LS**	**HS**	**LS**	**HS**	**LS**	**HS**
$^3T_{1g}\rightarrow{}^3E_g$ $^3T_{1g}\rightarrow{}^3T_{2g}$ $^3T_{1g}\rightarrow{}^3A_{1g}$ $^3T_{1g}\rightarrow{}^3A_{2g}$	$^5E_g\rightarrow{}^5T_{2g}$	$^2T_{2g}\rightarrow{}^2T_{1g}$ $^2T_{2g}\rightarrow{}^2A_{2g}$ $^2T_{2g}\rightarrow{}^2E_g$	N/A	$^1A_{1g}\rightarrow{}^1T_{1g}$ $^1A_{1g}\rightarrow{}^1T_{2g}$	$^5T_{2g}\rightarrow{}^5E_g$	$^2E_g\rightarrow{}^2T_{1g}$ $^2E_g\rightarrow{}^2T_{2g}$	$^4T_{1g}\rightarrow{}^4T_{2g}$ $^4T_{1g}\rightarrow{}^4A_{2g}$ $^4T_{1g}\rightarrow{}^4T_{1g}$

family of Fe^{2+} SCO complexes ($3d^6$), but this may also be particularly remarkable for Fe^{3+} and Mn^{2+} complexes, since the latter do not exhibit *d*–*d* transitions in the HS state (owing to their $3d^5$ electronic configuration), which implies that they must appear colorless – provided, of course, that no other absorption bands (e.g., intra-ligand or charge-transfer bands) fall in the visible range.

The intensity of absorption bands can be explained by examining the relevant selection rules, which define the transition probabilities between quantum states. Although the ligand-field transitions listed in Table 1 are spin-allowed – since the spin quantum number remains unchanged ($\Delta S = 0$) – they are, however, forbidden according to the Laporte (orbital) rule because these transitions involve *d* orbital states of the same parity. Consequently, the molar absorption coefficients associated with these *d*–*d* transitions are generally low, typically in the range $\varepsilon = 5$–100 L mol^{-1} cm^{-1} (as shown, for example, in Fig. 2a), which corresponds to absorption coefficients of the order of $\alpha = 10$–200 cm^{-1}, i.e., extinction coefficients (imaginary part of n^*) such that $k < 10^{-3}$. For this reason, SCO compounds such as $[Fe(ptz)_6](BF_4)_2$, which exhibit only *d*–*d* ligand-field transitions in the visible spectral range, appear colored in at least one spin state; however, they are generally not fully opaque, even for crystals of micrometric or millimetric thickness. One may nevertheless ask why *d*–*d* transitions are observable at all if they are forbidden? The reasons are multiple. The most important is that some degree of mixing between *d* and *p* orbitals occurs whenever the metal ion is not located at a center of symmetry, leading to a deviation from perfect octahedral symmetry. This can arise due to the presence of different ligands, the Jahn-Teller effect, or vibronic coupling [45]. Note that these phenomena, which allow for the "relaxation" of the Laporte rule, are also manifested by band polarization, splitting, and asymmetry.

For completeness, it is worth mentioning that other weaker ligand-field *d*–*d* transitions (not listed in Table 1) can also be observed between states with different spin multiplicities. For instance, Fe^{2+} complexes in the LS state also display spin-forbidden singlet → triplet transitions, such as $^1A_{1g}\rightarrow{}^3T_{1g}$ and $^1A_{1g}\rightarrow{}^3T_{2g}$, which generally occur at longer wavelengths compared to the spin-allowed transitions (980 and 670 nm, respectively, for $[Fe(ptz)_6](BF_4)_2$ [42]). However, as these transitions are both spin-forbidden and Laporte-forbidden, they are extremely weak ($\alpha < 1$ cm^{-1}, $k < 10^{-5}$) and therefore have a negligible influence on optical properties in most cases. The different mechanisms behind the appearance of such spin-forbidden bands include spin-orbit coupling, magnetic coupling, spin-flip or magnetic dipole transitions [45].

Besides metal-centered ligand-field transitions, the electronic spectra of SCO complexes also comprise transitions between the metal ion and the ligands – either metal-to-ligand (MLCT) or ligand-to-metal (LMCT) charge-transfer transitions – as well as ligand-centered (L–L) transitions. These bands are generally very intense, often overshadowing the much weaker ligand-field transitions. Ligand-centered absorptions (L–L) are typically associated with organic molecules containing delocalized electrons, resulting in intense π–π* transitions. These intra-ligand absorptions usually occur in the UV spectral region but can, in some cases, shift into the visible part of the spectrum, thus significantly contributing to the color of the complex. On the other hand, in general, these bands are only weakly affected by the spin-state change of the metal ion.

What makes the color changes of SCO complexes less predictable is the presence of intense charge-transfer (MLCT or LMCT) absorption bands, which can appear from the UV to the NIR spectral range [28]. The absorption coefficients associated with these charge-transfer transitions typically fall in the range $\alpha = 10^4$–10^5 cm^{-1}, corresponding to extinction coefficients k between 0.05 and 0.5. These transitions are 10^2 to 10^3 times more intense than *d*–*d* transitions since they are both spin-allowed and Laporte-allowed. Because of the simultaneous changes in the population of *d* orbitals and metal-ligand distances, the energy and intensity of MLCT and LMCT bands are significantly modified upon the SCO process. These spectral changes primarily arise from the increased metal-ligand bond lengths in the HS state, which results in poorer overlap between the metal-centered and ligand-centered orbitals compared to the LS state. However, other factors must also come into play, such as the ionization energy and/or electron affinity of the metal ion and ligands (i.e., their redox properties), which should depend on the molecular spin state as well. Contrary to *d*–*d* transitions, charge-transfer transitions cannot be predicted using Tanabe-Sugano diagrams. To this aim, proper molecular orbital (MO) diagrams must be drawn. As an illustration, Fig. 3 presents a schematic MO diagram for an octahedral ML_6 complex, highlighting the different types of possible electronic transitions. Notably, it appears that various g → u MLCT and u → g LMCT transitions are allowed as they satisfy the Laporte rule. However, to be fully allowed, these transitions must of course also preserve the spin multiplicity between the ground and excited states.

For many SCO materials, these charge-transfer absorption bands occur in the UV spectral region in both spin states, so they do not contribute to the color (change) of the compound. This is the case, for example, for the Fe^{2+} SCO complex [Fe(HB(1,2,4-triazol-1-yl)$_3$)$_2$]. As shown by spectrophotometric measurements carried out in a 100-nm-thick film of this complex (Fig. 4a), intense charge-transfer bands are observed around 300 nm in the LS state (with a maximum absorption coefficient of α = 65,000 cm^{-1}), which are completely bleached when switching the molecules into the HS state [46]. Note that this compound also exhibits a ligand-field *d*–*d* transition at 535 nm in the LS state, which, however, remains undetectable by spectrophotometry in such nanometric thin films. As shown in the inset photograph of Fig. 4a, the film is fully transparent to the eye in both spin states. On the other hand, for many other SCO compounds (e.g., those formed from ligands with extended π-systems), such intense charge-transfer transitions may instead appear in the visible wavelength range, making the compound highly absorbing (in the visible) and thus intensely colored in at least one spin state. This example is illustrated in the case of the 3D-Hoffman metal-organic framework (MOF) [Fe(pyrazine)Pt(CN)$_4$]•2.6 H$_2$O (Fig. 4b), whose absorption spectrum in the LS state is dominated by two intense MLCT bands around 500 and 535 nm [47]. Upon the LS-to-HS switching, these two bands disappear and are replaced by a new one that emerges around 450 nm. Consequently, as shown in Fig. 4b, the compound, which appears pink-red in the LS state, changes to a yellowish color in the HS state.

Overall, it turns out that SCO compounds exhibiting charge-transfer bands in the visible spectral range are intensely colored and nearly opaque, even for thicknesses as small as 1 μm. On the other hand, in sub-micrometer-thick samples, these absorption bands can be readily probed using transmission spectroscopy techniques, for instance, to monitor the SCO phenomenon in nanometer-sized objects. However, it is undeniable that the metal-centered ligand-field absorption bands are too weak to be detected in sub-micrometer-thick samples, even though the concentration of absorbing metal centers is high (e.g., pure, non-diluted solid-state compounds).

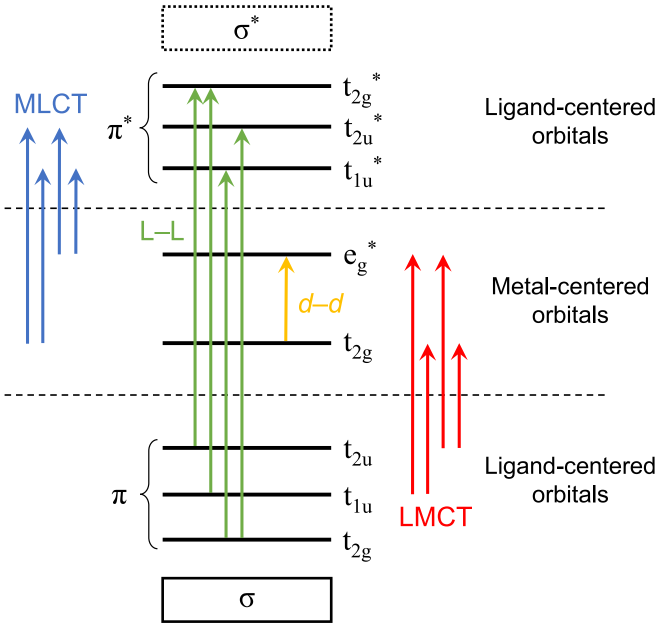

Fig. 3. Simplified molecular orbital diagram for an octahedral ML_6 complex with partially occupied metal-centered t_{2g} and e_g orbitals, and empty ligand π* orbitals, schematically showing different types of electronic transitions (*d*–*d* in yellow, MLCT in blue, LMCT in red, and L–L in green). (For interpretation of the references to color in this figure legend, the reader is referred to the web version of this article.)

2.3. Changes in the refractive index of spin-crossover materials

Besides the change in the extinction coefficient, *k*, it is less commonly acknowledged that the real part, *n*, of the complex refractive index of SCO compounds also undergoes significant variations across different spectral regions. Up to now, only a few studies were dedicated to the refractive index switching of SCO compounds. To the best of our knowledge, the first investigation of refractive index changes during the SCO process was reported by Hauser [48], who studied transient phase gratings, generated by means of four-wave-mixing, in single crystals of the compound [Zn$_{0.9}$Fe$_{0.1}$(ptz)$_6$](BF$_4$)$_2$. He concluded that the observed refractive index change primarily reflects the mass density variation brought into by the spin-state switching. Later, the refractive index of different SCO compounds was assessed in the UV–vis-NIR spectral ranges in both spin states using spectroscopic ellipsometry (Fig. 5) and other optical characterization techniques (see Table 2) [49–56]. From these available experimental data, several remarks can be made.

First, like most organic molecular materials, the refractive index of SCO materials in the vis-NIR regions always lies, unsurprisingly, in the range between 1.5 and 1.8. Second, as *n* and *k* are connected through the Kramers-Kronig relations (Eqs. (21) and (22)), any significant variation in *k* (i.e., the optical absorption of the material) between the two spin states within a given wavelength domain inevitably leads to corresponding substantial changes in *n* within the same spectral range. This effect is clearly observed, for instance, in the compounds [Fe(NH$_2$-trz)$_3$](Br$_2$) (Fig. 5a) [49] and [Fe(HB(1,2,4-triazol-1-yl)$_3$)$_2$] (Fig. 5b) [56], which both exhibit intense spin-state-dependent charge-transfer absorption bands in the UV range (around 300 nm) in the LS state, resulting in sharp spectral variations in *n* in this wavelength domain. As these absorption bands are absent in the HS state, large variations in the refractive index (typically of the order of 0.1–0.2) can thus be observed

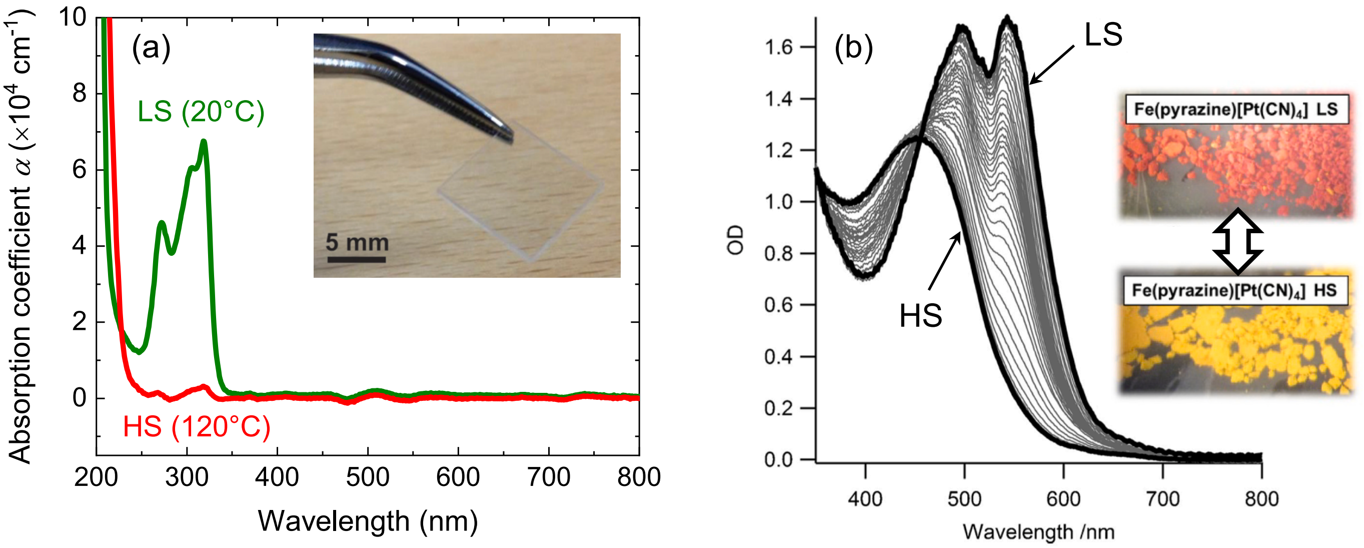

Fig. 4. (a) Optical absorption spectra of a 100-nm-thick film of the SCO complex [Fe(HB(1,2,4-triazol-1-yl)$_3$)$_2$] acquired at 20 °C (LS state) and 120 °C (HS state). A maximum absorption coefficient of $\alpha = 65{,}000$ cm^{-1} is observed around 300 nm in the LS state, associated with the presence of charge-transfer bands. Inset: photograph of the film at room temperature (LS state) deposited on a fused-silica substrate. Reproduced with permission from Ref. [46]. (b) Variable-temperature absorption spectra of a microcrystalline powder of the compound [Fe(pyrazine)Pt(CN)$_4$]•2.6 H$_2$O, dispersed in a KBr pellet, acquired between 300 K (HS state) and 10 K (LS state). Adapted with permission from Ref. [47].

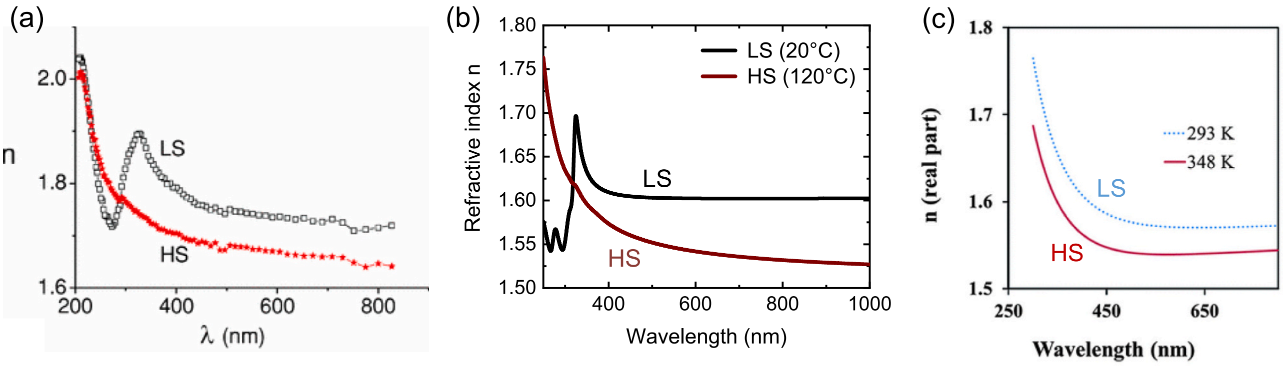

Fig. 5. Refractive index spectra in the UV–vis wavelength ranges, extracted from spectroscopic ellipsometry measurements for the SCO compounds (a) [Fe(NH$_2$-trz)$_3$](Br$_2$), (b) [Fe(HB(1,2,4-triazol-1-yl)$_3$)$_2$] and (c) [Fe(hptrz)$_3$](OTs)$_2$, in both spin states. Reproduced with permission from Ref. [49,51,56].

Table 2
Refractive index measured in different SCO compounds in the visible spectral range in the two spin states, and comparison with the unit-cell volume change upon the spin transition.

SCO compound	n_{LS}	n_{HS}	$\Delta n_{HL} = n_{HS} - n_{LS}$	Δn_{HL} / (1 − n_{LS})	Method of investigation	ΔV_{HL} / V_{LS}	Reference
[Fe(NH$_2$-trz)$_3$](Br$_2$)	1.74 (500 nm) 1.71–1.76 (550 nm)	1.68 (500 nm) 1.57–1.63 (550 nm)	−0.06 (500 nm) −0.11 (550 nm)	8.1 % 14.5 %	Spectroscopic ellipsometry (powder) Minimum deviation method (nanoparticles in solution)	Not reported	[49] [53]
{Fe(bpac)[Pt(CN)$_4$]}	1.75 (650 nm)	1.67 (650 nm)	−0.08 (650 nm)	10.7 %	Optical diffraction on gratings (thin film)	9.8 %	[52]
[Fe(hptrz)$_3$](OTs)$_2$	1.58 (660 nm) 1.57 (visible)	1.57 (660 nm) 1.55 (visible)	−0.01 (660 nm) −0.02 (visible)	1.7 % 3.5 %	Ellipsometry and SPR spectroscopy (thin film) Spectroscopic ellipsometry (thin film)	Not reported	[50] [51]
[Fe(Htrz)$_2$(trz)](BF$_4$)	~1.7 (vis-NIR)	~1.6 (vis-NIR)	−0.10 (vis-NIR)	14 %	LSPR spectroscopy (Au@SCO nanoparticles)	11.5 %	[54]
[Fe(HB(1,2,4-triazol-1-yl)$_3$)$_2$]	1.62 (500 nm)	1.57 (500 nm)	−0.05 (500 nm)	8.1 %	Spectroscopic ellipsometry (thin film)	4.5 %	[55]

upon the molecular spin-state change in the UV (see Fig. 5a and b). In these spectral ranges, the refractive index may be higher in either the HS or LS state, depending on which spin state is the most absorbing.

Third and most importantly, a substantial broadband change in n also occurs in many SCO compounds within the vis-NIR regions, i.e., in spectral windows away from intense absorption bands. As shown in Fig. 5 and Table 2, the experimental data for all the studied compounds consistently reveal that the refractive index decreases by ca. 0.01–0.1 over the entire vis-NIR range when going from the LS to the HS state. For example, spectroscopic ellipsometry measurements performed on the SCO compound $[Fe(NH_2\text{-trz})_3](Br_2)$ (in pellet form) revealed a notable decrease in the refractive index, $\Delta n_{HL} = n_{HS} - n_{LS} \approx -0.06$, in the whole visible domain upon the LS-to-HS transition (Fig. 5a) [49]. The refractive index of the same compound, studied under the form of nanoparticles dispersed in solution, was also estimated using the minimum deviation method, which consists in measuring the minimum angle of deviation of light through a prism filled with the investigated microemulsion [53]. In this case, a notable refractive index change from 1.76 (LS state) to 1.63 (HS state) was reported at 550 nm. Similarly, spectrophotometric and ellipsometric investigations revealed a well-reversible change in the refractive index upon the SCO in vacuum thermally deposited thin films of the Fe^{2+} complex $[Fe(HB(1,2,4\text{-triazol-}1\text{-yl})_3)_2]$ in the whole visible spectral range (see Fig. 5b), with Δn_{HL} reaching -0.05 at 500 nm, between 1.62 (LS state) and 1.57 (HS state) [55,56]. As for thin films of the complex $[Fe(hptrz)_3](OTs)_2$, a smaller variation in the refractive index ($\Delta n_{HL} = -0.02$) was derived across the visible range using spectroscopic ellipsometry (Fig. 5c) [51].

Importantly, as summarized in Table 2, for most of the SCO compounds studied, the relative change in the refractive index, expressed as $\Delta n_{HL} / (1 - n_{LS})$, is found to approximately match the relative volume expansion, $\Delta V_{HL} / V_{LS}$, observed during the LS-to-HS transition. This observation agrees with the empirical Gladstone-Dale relation [57]:

$$\frac{\Delta n_{HL}}{1 - n_{LS}} = \frac{\Delta V_{HL}}{V_{LS}} \tag{23}$$

which indeed predicts a decrease in the refractive index, $\Delta n_{HL} = n_{HS} - n_{LS}$, ranging from -0.01 to -0.1 for each SCO compound due to the relative volume change, $\Delta V_{HL} / V_{LS} = 1$–$10$ %, typically accompanying the LS-to-HS transition. This important observation indicates that the molecular volume (or mass density) change of SCO materials is the main factor at the origin of the refractive index modulation in the vis-NIR spectral ranges. As mentioned above, this volume change primarily results from the substantial elongation of the metal-ligand bond lengths when switching from the LS to the HS state, due to the larger occupancy of the anti-bonding e_g orbitals of the metal ion in the HS state.

Interestingly, this change in n occurs in (quasi-)transparent wavelength windows of the material, where absorption remains extremely low in both spin states. For example, Fe^{2+} SCO compounds, such as $[Fe(HB(1,2,4\text{-triazol-}1\text{-yl})_3)_2]$ and $[Fe(Htrz)_2(trz)](BF_4)$, exhibit only weak ligand-field d–d absorption bands centered around 540 nm ($^1A_{1g} \rightarrow {}^1T_{1g}$) in the LS state and around 830 nm ($^5T_{2g} \rightarrow {}^5E_g$) in the HS state, associated with low absorption coefficients ($\alpha < 200$ cm^{-1}, $k < 10^{-3}$). Therefore, a remarkable feature of many SCO materials is that they can display significant changes in n over broad spectral ranges, while the extinction coefficient remains extremely low and virtually unchanged in both spin states (k and $\Delta k < 10^{-3}$). As we will see later, this property turns out to be very useful for specific applications that aim to manipulate the phase of optical waves without altering their amplitude. It should be stressed that this change in n, which occurs *independently* of any variation in k, remains consistent with the Kramers-Kronig relations (Eq. (21) and (22)). Indeed, this modulation of the refractive index is not related to a change in the electronic polarizability of the molecules. Instead, it results from a change in the number of (electronic) oscillators per unit volume in the material caused by the spin-state switching, which generates a global modification of n over the whole spectrum. (In fact, this phenomenon is similar to the decrease in n observed in most materials when the temperature rises due to ordinary thermal expansion.) This effect can be accounted for within the framework of the Kramers-Kronig relations through a change in n_∞ (high-frequency refractive index) upon the spin transition.

As indicated in Table 2, the studies dedicated to the refractive index change of SCO materials have mainly been carried out on powders, nanoparticles dispersed in solution, or polycrystalline thin films, but never on single crystals. Such investigations would, however, be very instructive, for example, for exploring the anisotropy of the refractive index and the associated birefringence effects (as well as their evolution upon spin-state switching), since the volume change of SCO materials can be highly anisotropic in some cases [19]. This question remains totally unexplored until now. Another question arises regarding a possible variation in the refractive index with size reduction, particularly at ultra-small sizes (< 10 nm). From currently available data, no significant change in the refractive index of SCO materials has been reported in nano-objects, compared to bulk materials [52]. However, this issue will certainly require more detailed and specific studies in the future.

At this point, it may be worth mentioning that the dielectric properties of SCO materials have also been investigated in other spectral ranges, from the THz (far infrared) domain [58–60], through the GHz (microwave) range [61,62], and down to the domain of radio and quasi-static frequencies (Hz–MHz) [63–73]. As illustrated schematically in Fig. 6, different microscopic mechanisms of polarizability take place across various frequency ranges, resulting in a pronounced frequency dependence of the complex relative permittivity and refractive index. As the excitation frequency is lowered, more and more different mechanisms can contribute to the overall polarization of the material. These different polarizability processes are associated with well distinct characteristic (relaxation or resonance) frequencies, beyond which they can no longer contribute to the permittivity because they are unable to follow the frequency of the electric field. Consequently, these relaxation or resonance processes are characterized by a dissipation peak in the imaginary part, ε_r'', as well as a step-like decrease in the real part, ε_r', of the complex relative permittivity.

As shown in Fig. 6, the only microscopic mechanism involved in polarizability in the UV–vis-NIR spectral ranges is of electronic origin. Indeed, electronic polarizability accounts for the relative tendency of electron clouds of atoms and molecules to be distorted from their normal shape by an external electric field, inducing local dipole moments.

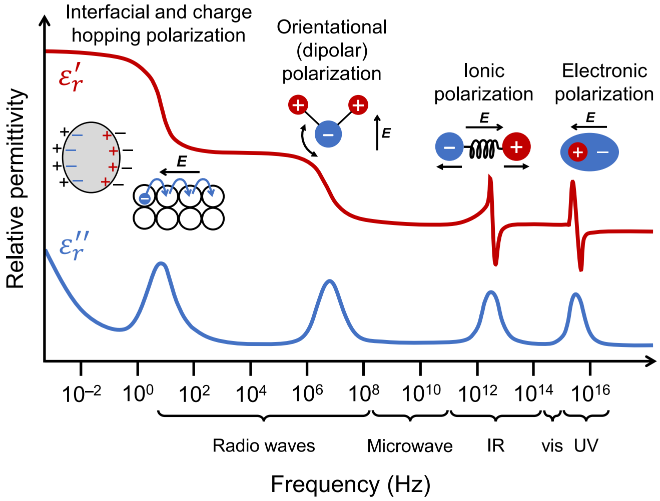

Fig. 6. Dielectric spectral response of materials, showing the typical evolution of the real (ε_r') and imaginary (ε_r'') parts of the complex relative permittivity over a wide range of frequencies. The various microscopic mechanisms at the origin of the dielectric response are depicted.

Because of the larger volume of HS molecules, which may favor larger deformation of electron clouds (particularly of the metal ion), a higher electronic polarizability might be expected in the HS state in comparison with the LS state. However, as mentioned above, experimental data show that the variation in electronic polarizability between the LS and HS states is, in fact, relatively small. Instead, the main contribution to Δn_{HL} simply arises from the reduction in the number of electronic oscillators per unit volume upon the LS-to-HS switching, associated with the crystal lattice volume expansion of the material.

At lower frequencies, from the infrared spectral region and below, another contribution, referred to as ionic (or atomic) polarizability, strongly contributes to the relative permittivity (Fig. 6). This contribution originates from the displacement of ions and atoms relative to the crystal lattice under the influence of an external electric field, which gives rise to net dipole moments. Typically, the ionic polarizability varies as $1 / \omega_e^2$, where ω_e is the harmonic natural frequency of the bond between two atoms [74]. Interestingly, the few experimental data available in the THz and GHz ranges (obtained only for SCO compounds of the Fe-triazole family) reveal that the relative permittivity systematically exhibits opposite behavior compared to the vis-NIR response, i.e., it increases upon the LS-to-HS switching [58–62]. For example, the refractive index of the SCO compound [Fe(NH$_2$-trz)$_3$](Br$_2$) increases from 1.70 to 1.84 ($\Delta n_{\mathrm{HL}} = +0.14$) at 0.6 THz when going from the LS to the HS state, and from 2.42 to 2.50 ($\Delta n_{\mathrm{HL}} = +0.08$) at 37 GHz (see Table 3) [60,62]. A similar evolution was also reported for the related compound [Fe(NH$_2$-trz)$_3$](NO$_3$)$_2$ [60,62]. This change in the sign of Δn_{HL} in the THz and GHz regions suggests that the dielectric response of the material is no longer dominated by variations in mass density (as in the vis-NIR ranges), but rather by the contribution of ionic polarizability. Indeed, ionic polarizability is expected to be greater in the HS state due to the significant decrease in the frequency ω_e of certain vibrational modes – particularly those associated with the coordination octahedron – during the LS-to-HS transition. We can thus postulate that this reduction in bond rigidity facilitates the displacement of atoms under the influence of an applied electric field, leading to increased ionic polarizabilities in the HS state.

As an example, and to illustrate the typical frequency evolution of the dielectric response of SCO materials, Table 3 summarizes the values of the complex relative permittivity and refractive index of the SCO compound [Fe(NH$_2$-trz)$_3$](Br$_2$) measured across different frequency ranges, from visible to GHz [49,60,62]. While $\Delta n_{\mathrm{HL}} = n_{\mathrm{HS}} - n_{\mathrm{LS}}$ is negative in the visible spectral range, a change in the sign of Δn_{HL} is observed in the THz–GHz domains, accompanied by substantial variations in n of the order of 0.1 upon the SCO.

Then, at even lower frequencies (< 1 MHz), other mechanisms come into play, such as the orientational polarization of permanent dipole moments (if existing) and the polarization associated with site-to-site charge hopping phenomena, which contribute to the electrical conductivity of the material (Fig. 6). The relaxation processes associated with these polarization mechanisms, which contribute to the imaginary part of ε_r^*, are known to be thermally activated, so that their relaxation frequencies generally depend on temperature. As with ionic polarizability, a higher orientational (dipolar) polarizability can be expected in the HS state because the larger lattice volume can facilitate the reorientation of polar entities (e.g., solvent molecules) with the applied electric field as molecular mobility increases. Regarding electrical conductivity, in low-mobility solids such as molecular SCO compounds, charge transport occurs via charge hopping conduction between localized sites [75]. The hopping motion of an electrical charge involves a dielectric relaxation, as it is inherently associated with a redistribution of counter charges within the material. Owing to higher phonon frequencies in the LS state, experimental data consistently show larger electrical conductivity of SCO compounds in the LS state due to higher hopping rates. Hence, an increased conductivity relaxation frequency can also be expected in the LS state [70].

Table 3
Evolution of the complex relative permittivity and refractive index of the SCO compound [Fe(NH$_2$-trz)$_3$](Br$_2$) in the two spin states, recorded across different frequency ranges from the microwave to the visible domain.

	Visible (600 THz) [49] $\lambda_0 = 500$ nm		Far infrared (0.6 THz) [60] $\lambda_0 = 500$ µm		Microwave (37 GHz) [62] $\lambda_0 = 8.1$ mm	
	LS	HS	LS	HS	LS	HS
n	1.74	1.68	1.70	1.84	2.42	2.50
Δn_{HL}	−0.06		+0.14		+0.08	
k	$\approx 10^{-3}$	≈ 0	0.44	0.42	0.02	0.06
Δk_{HL}	$\approx -10^{-3}$		−0.02		+0.04	
ε_r'	3.03	2.82	2.70	3.21	5.86	6.19
ε_r''	≈ 0	≈ 0	1.50	1.55	0.12	0.32

At very low frequencies (Hz–MHz), all the contributions mentioned above may contribute to the total dielectric response (relative permittivity) of the material. As such, it turns out that very different behaviors can be observed from one compound to another. In some SCO materials, the LS-to-HS transition is accompanied by an increase in the real part ε_r' [63–65,68,69,72,73], which seems to indicate that the contributions of ionic (and even dipolar) polarizabilities still dominate the overall dielectric response of the material at these excitation frequencies. On the other hand, other compounds show the opposite behavior, with a decrease in ε_r' in the HS state [66,67,70,71]. In the case of the SCO compound [Fe(Htrz)$_2$(trz)](BF$_4$), this drop in ε_r' upon the LS-to-HS switching was attributed to a significant contribution from charge transport relaxation to the permittivity [67,70], since a sharp decrease in electrical conductivity (by $\sim$2 orders of magnitude) is observed in this compound in the HS state [76]. Finally, it should be mentioned that extrinsic contributions to the polarization can also arise due to the presence of electrical charges trapped by inhomogeneities in the material and structural interfaces. Thus, the region at very low frequencies is generally dominated by significant dispersion caused by interfacial polarization (e.g., electrode polarization), which, however, is not purely a material property. This contribution can obviously vary significantly depending on experimental conditions.

3. The (complex) refractive index change of spin-crossover materials as a means of optical detection

Taking advantage of the significant changes in the complex refractive index, n^*, of SCO materials across broad spectral ranges, numerous experimental optical or photonic detection methods can be used to probe and characterize the SCO phenomenon. As we shall see in this section, these photonic detection methods turn out to be particularly powerful for characterizing the spin transition in nanometric thin films and nanopatterns, down to the scale of individual nano-objects. Furthermore, as the spin-state equilibrium is sensitive to a variety of physicochemical parameters of the external environment, considerable efforts have been devoted to the development of diverse optical sensing applications based on the complex refractive index change of SCO (nano)materials.

3.1. Detecting and investigating the spin-crossover phenomenon

3.1.1. Detection based on optical absorption change

One of the simplest and most straightforward methods for characterizing the SCO phenomenon is to monitor the color change (i.e., the absorbance change) of the compound. Following this principle, a common way to quantitatively determine the LS and HS fractions in non-opaque, homogeneous SCO samples – such as single crystals, thin films, or solutions – is to measure the optical absorbance of the sample in the UV–vis-NIR spectral domains using a spectrophotometer. (N.B. Strictly speaking, the definition of absorbance, $A = -\log_{10}(T)$ (Eq. (19)), neglects losses due to reflection and scattering of light.) Indeed, according to the Beer-Lambert law (Eq. (15)), since A is proportional to the

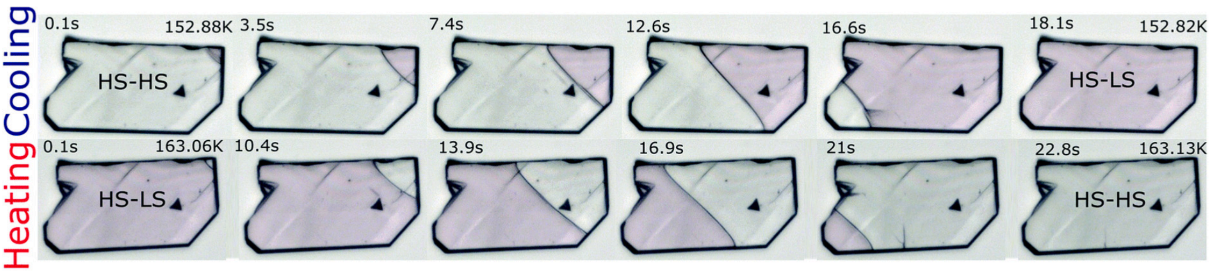

Fig. 7. Time-resolved optical transmission microscopy snapshots of a SCO single crystal of $[Fe(2\text{-}pytrz)_2\{Pd(CN)_4\}]\cdot 3H_2O$ during the thermally induced spin transition upon cooling and heating. The images reveal that the spin-state switching occurs through a nucleation and growth process, whereby the new stable phase nucleates from the top right corner of the crystal before growing via the propagation of a phase boundary. Reproduced with permission from Ref. [84].

concentration of absorbing species in the sample, the absorbance measured at a well-chosen wavelength (within a spin-state-dependent absorption band) merely scales with the fraction of LS or HS molecules. Based on this principle, time-resolved optical transmission microscopy has emerged as a powerful, non-invasive imaging tool for the spatiotemporal observation of the spin transition in micrometric SCO single crystals [77–85] (see Fig. 7). The fraction of HS molecules, $X_{HS}(x, t)$, at position x and time t, can be deduced from the measured absorbance images, $A(x,t)$, using the following formula:

$$X_{HS}(x,t) = \frac{A(x,t) - A_{LS}}{A_{HS} - A_{LS}} \tag{24}$$

where A_{LS} and A_{HS} are the absorbances of the sample in the full LS and HS states, respectively. These investigations have made it possible to monitor, quantitatively, the evolution of the fraction of HS molecules with μm spatial and μs temporal resolution (for instance, by using a pump-probe approach [86]), leading to significant advances in understanding the transition mechanisms and the underlying switching dynamics of individual SCO single crystals [35]. In a fairly similar approach, the use of ultrashort pulsed lasers allows the LS/HS fraction (and, subsequently, the ultrafast spin-transition dynamics) to be monitored with sub-picosecond time resolution through pump-probe optical absorption techniques [46,87–93].

In micrometer-sized crystals, optical detection can typically be achieved by monitoring a ligand-field *d*–*d* transition band (usually in the vis-NIR spectral ranges), where the change in the absorption coefficient upon spin-state switching is ordinarily of the order of $\Delta\alpha = 100\ \text{cm}^{-1}$. As an example, for a 50-μm-thick crystal, this change in α corresponds to a variation in optical absorbance of $\Delta A \approx 0.22$, which is readily detectable by any optical detection device. However, since absorbance is proportional to the path length, the optical contrast between the two spin states often becomes extremely low in nanometer-sized samples. To illustrate this shortcoming, the absorbance change in a 50-nm-thick SCO sample associated with a ligand-field band is expected to be $\Delta A \approx 10^{-4}$, which is below the detection limit of most standard commercial spectrophotometers. For such small-sized samples, it is often possible, however, to detect and characterize the spin transition by instead probing charge-transfer bands (typically in the UV spectral range, but sometimes in the visible domain for certain compounds), whose variations in the absorption coefficient ($\Delta\alpha \approx 10^4$–$10^5\ \text{cm}^{-1}$) lead to absorbance changes ($\Delta A \approx 0.02$–0.2 for a 50-nm-thick film) that are large enough to be detected [94–97]. For this reason, UV–vis spectrophotometry is a technique of choice to quantitatively characterize the molecular spin-state switching in nanometric thin-film samples.

For example, Fig. 8a displays temperature-dependent UV–vis absorption spectra of a 130-nm-thick film of the Fe^{2+} SCO complex $[Fe(HB(3,5\text{-}(CH_3)_2\text{-}pz)_3)_2]$ deposited by thermal evaporation [98]. At 325 K (HS state), the spectrum is essentially featureless except at wavelengths below 250 nm, where strong UV absorption bands attributed to intraligand and charge-transfer transitions of the HS species are observed. Upon cooling the film down to 103 K, two well-resolved absorption bands appear at 349 and 278 nm, corresponding to MLCT absorptions of molecules in the LS state. Therefore, as shown in Fig. 8b, monitoring the temperature dependence of these MLCT bands allows for a quantitative determination of the thermal spin-transition curve, revealing, in the case of thin films of $[Fe(HB(3,5\text{-}(CH_3)_2\text{-}pz)_3)_2]$, a pronounced asymmetric thermal hysteresis loop, as well as varying completeness of the spin transition at low temperatures depending on the film preparation method (as-deposited or annealed). However, it should be noted that such quantitative characterization is only feasible with homogeneous, high-quality thin films that exhibit minimal light scattering. In some

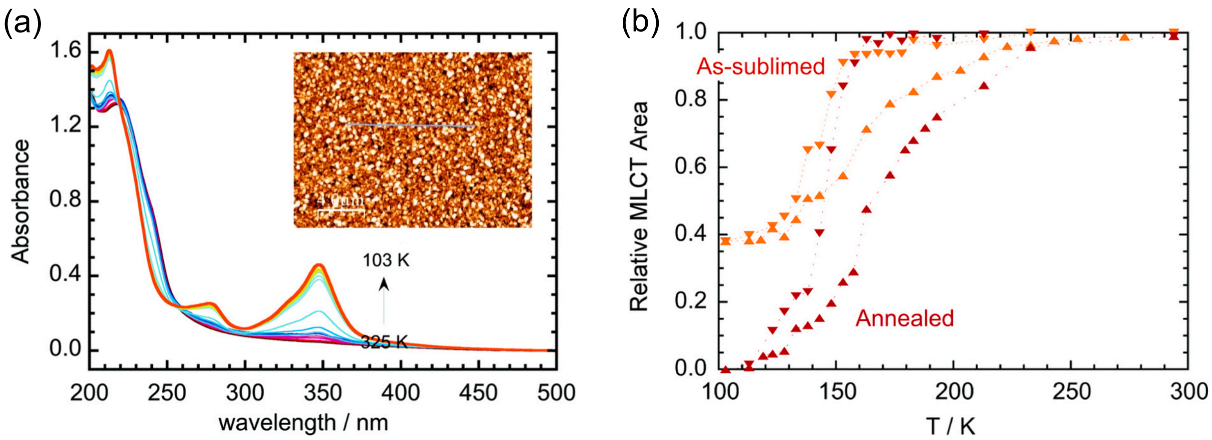

Fig. 8. (a) Absorption spectra of an as-deposited 130-nm-thick film of the Fe^{2+} SCO complex $[Fe(HB(3,5\text{-}(CH_3)_2\text{-}pz)_3)_2]$, recorded upon cooling from 325 to 103 K. The inset displays an AFM topography image of the film. (b) Spin-transition curves of the as-deposited and annealed films, extracted from the temperature dependence of the MLCT absorption band at 349 nm. Reproduced with permission from Ref. [98].

instances, this technique can also be applied to ‘heterogeneous’ systems (e.g., SCO nanoparticles embedded in a transparent polymer matrix), provided the heterogeneity size (e.g., particle size) is much smaller than the optical wavelength, thereby minimizing scattering losses.

3.1.2. *Detection based on synergetic luminescent properties*

In a few cases, the absorbance change was also used in a less direct way, through luminescent doping, as fluorescence is a highly sensitive technique (ideally down to single-molecule detection) that allows for higher signal-to-noise ratios and, consequently, higher contrast. The basic idea is to choose a luminophore whose emission and/or excitation spectra show a suitable overlap with the characteristic HS or LS absorption bands of the SCO material, enabling selective quenching of the luminescence in a given spin state of the metal centers. The luminescence response primarily results from the opening or closing of non-radiative relaxation channels for the luminophore in the excited state, which occurs either due to spin-state-dependent changes in the spectral overlap between the luminophore and the SCO molecules, or as a result of the structural changes accompanying the spin transition [99]. Consequently, a relatively large modulation of luminescence intensity could be achieved as a function of the spin state of the metal centers [100]. For instance, a modulation of the luminescence signal has been reported in thin films of $[Fe(NH_2\text{-trz})_3](OTs)_2$ nanoparticles doped with rhodamine-110 [101], or through the use of a luminophore grafted onto the surface of SCO nanoparticles [102]. Following this approach, various studies have been conducted using different types of grafted fluorophores, including organic molecules, lanthanide complexes, and quantum dots [100]. These investigations provide a deeper understanding of the energy transfer mechanisms involved in these hybrid compounds. For example, when pyrene molecules are grafted onto the surface of the silica shell of SCO@shell particles (see Fig. 9a), the spin-state sensitivity of the excimer emission was attributed not only to radiative energy transfer mechanisms but also to non-radiative effects, which are related to changes in the pyrene-pyrene distance induced by the spontaneous mechanical strain accompanying the spin transition [103]. Interestingly, it should be emphasized that such a large modulation of luminescence occurs even if the emission and/or excitation bands of the luminophore are combined with the weak ligand-field *d*–*d* absorption bands of the complex, enabling SCO detection to be achieved in individual nano-objects using visible light. As an example, the SCO properties of single fluorescent nanodots of the $[Fe(hptrz)_3](OTs)_2$ derivative, doped with acridine orange and fabricated using a soft lithography approach, could be readily determined by fluorescence microscopy at around 550 nm (Fig. 9b) [104].

On the other hand, some compounds intrinsically exhibit SCO-dependent fluorescence properties – without the need for luminophore doping – which can be achieved through the use of specific ligands, the synthesis of lanthanide-based heterodinuclear complexes (Ln-Fe), or the encapsulation of guests [105–111]. For example, the spin-transition curve of the dinuclear complex $[Fe_2(L1)_5(NCS)_4]\cdot 4MeOH$ (L1 = *N*-salicylidene-4-amino-1,2,4-triazole) could be successfully tracked via fluorescence by following the temperature-dependent shifts of emission bands associated with the radiative relaxation of intra-ligand electronic transitions [112]. More recently, Piguet et al. [113] reported the monitoring of the Fe^{2+} spin state through Eu^{3+} fluorescence in heterodinuclear complexes. The resulting temperature-dependent Eu^{3+}-centered emission observed for $[EuFe\text{-}(L)_3](CF_3SO_3)_5$ (where L stands for various ligands containing benzimidazole-2-yl-pyridine units) provides unambiguous evidence for the indirect lanthanide-based optical detection of SCO.

3.1.3. *Detection based on refractive index change*

Beyond changes in the optical absorption (or emission) properties of spin-transition materials, the modification of the real part, *n*, of the complex refractive index can also be used to probe the SCO phenomenon, particularly in nanostructures and nanometric thin films. As mentioned in the previous section, spectroscopic ellipsometry (Fig. 5) is a powerful, dedicated method for probing changes in *n* over broad spectral ranges, and thereby detecting the molecular spin-state switching [49,51,55]. However, other refractive-index-sensitive methods can

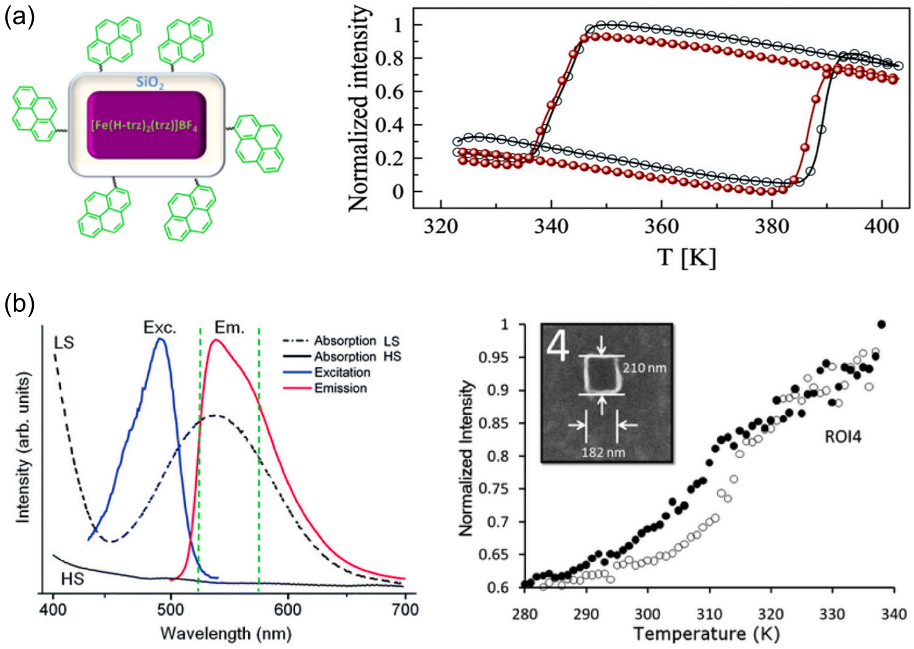

Fig. 9. (a) (*left panel*) Pyrene-grafted $[Fe(Htrz)_2(trz)](BF_4)@SiO_2$ core-shell particles and (*right panel*) their normalized excimer luminescence intensity recorded at 550 nm for two successive thermal cycles. Reproduced with permission from Ref. [103]. (b) (*left panel*) Normalized excitation (blue curve) and emission (red curve) spectra of the complex $[Fe(hptrz)_3](OTs)_2$ doped with acridine orange in the solid state. The black lines depict the absorption spectra of an undoped chloroform solution of the SCO complex in both spin states. The vertical dashed lines indicate the spectral pass band (around 550 nm) used in fluorescence microscopy experiments to acquire the thermal variation of the luminescence for a selected nanodot (*right panel*). The inset shows a magnified SEM image of the studied nanodot. Reproduced with permission from Ref. [104].

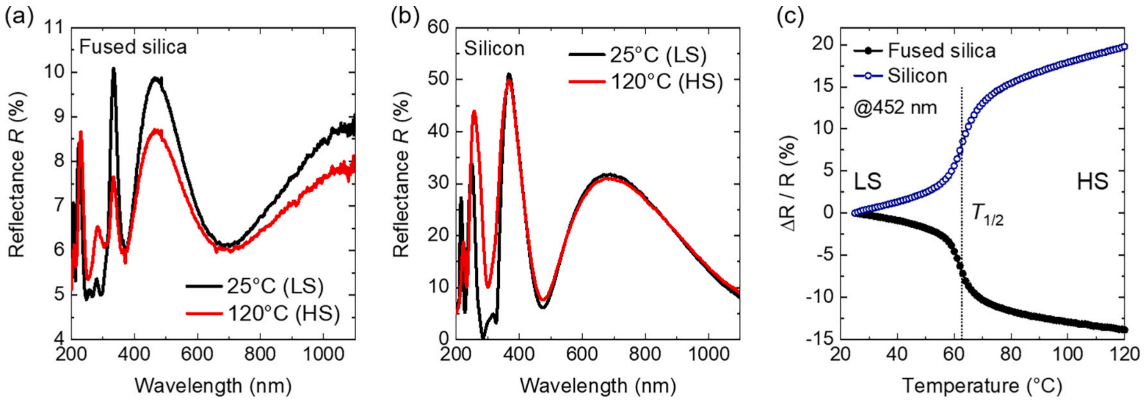

Fig. 10. Reflectance spectra of a 215-nm-thick film of the SCO complex [Fe(HB(1,2,4-triazol-1-yl)$_3$)$_2$] recorded at normal incidence on (a) fused-silica and (b) silicon substrates. (c) Corresponding relative variation of optical reflectance, $\Delta R / R$, at 452 nm as a function of temperature. The dotted vertical line indicates the spin-transition temperature ($T_{1/2}$) of the SCO film.

also be employed.

First, since changes in n affect the refraction and reflection conditions at interfaces, a straightforward manner to study the spin transition is to measure the specular reflection of (high-quality, low-roughness) thin films or single crystals. Indeed, even in spectral ranges far from the intense absorption bands of the compound, large and reproducible variations in the specular reflectance can be observed in SCO nanometric thin films, of the order of $\Delta R / R \approx 10$–20 %, due to the refractive index modulation (Fig. 10), thus allowing for a quantitative characterization of the SCO phenomenon [97,114]. Special attention must be paid to the wavelength of study, since the reflectance spectra of thin films exhibit oscillations caused by constructive and destructive interference between the beams reflected at the air/film and film/substrate interfaces. Thus, at certain specific wavelengths, the change in R will be almost zero. An example is shown in Fig. 10a for a 215-nm-thick film of the SCO complex [Fe(HB(1,2,4-triazol-1-yl)$_3$)$_2$] on a fused-silica substrate. On this substrate, the reflectance level is low (between 5 % and 10 % over the entire spectrum), but a substantial relative decrease in R (e.g., by $\Delta R_{\mathrm{HL}} / R_{\mathrm{LS}} \approx -13$ % at 452 nm, see Fig. 10c) can be observed in many spectral ranges when switching the film into the HS state. In this compound, the LS-to-HS transition, which is accompanied by a drop in the refractive index from 1.62 to 1.57 in the visible range (see Table 2), leads to a reduced refractive index mismatch with air ($n_{\mathrm{air}} = 1$) and with the substrate ($n_{\mathrm{sub}} \approx 1.46$), resulting in a decrease in the amplitude of the oscillations of R in the HS state. Obviously, both the level of optical reflectance and the spin-state-dependent changes strongly depend on the nature of the substrate. Nevertheless, regardless of the substrate, a significant relative variation in R is also always evidenced in the UV spectral region, where the SCO film exhibits large optical absorption changes. As shown in Fig. 10a and b, a considerable increase in optical reflectance is observed around 300 nm (by $\Delta R_{\mathrm{HL}} / R_{\mathrm{LS}} = +20$ % and $+205$ % on fused-silica and silicon substrates, respectively) when going from the LS to the HS state, because the intense charge-transfer bands of the SCO compound result in low specular reflectance in the LS state.

Beyond specular reflection, which is effective only for high-quality, low-roughness thin films or single crystals, it should be noted that the SCO phenomenon can also be routinely detected and monitored by diffuse reflection on polycrystalline samples, such as powders. In this case, the most general mechanism responsible for diffuse reflection does not solely involve the refractive index contrast at the external surfaces of the probed material, but rather all the scattering centers within it (e.g., grain boundaries, crystallite surfaces, internal defects, etc.), which generate a series of scattered (primary, secondary, etc.) rays in random directions. In addition, as light enters the material, the diffused rays will lose some wavelengths during their path though the material due to absorption, and will thus emerge colored. Therefore, because of the color change of spin-transition materials, the SCO phenomenon can be readily monitored by diffuse reflection (or diffuse scattering) in a large variety of samples in different forms. However, it should be underlined that this characterization method is not truly quantitative, since it is nearly impossible to deduce the exact fraction of LS or HS molecules within the sample, the level of scattering intensity (and its variation) depending on many other parameters.

As an alternative experimental method, the detection of the spin transition was also demonstrated in micrometric surface-relief gratings made of a SCO material, by means of optical diffraction [51,52]. In these gratings, fabricated via lithographic methods, the modulation of the molecular spin state leads to a spatially periodic change in the refractive index, which, in turn, induces a substantial modification of the diffraction pattern acquired by transmission microscopy. For example, SCO detection was demonstrated on gratings of the compound [Fe(hptrz)$_3$](OTs)$_2$ by measuring the change in the first-order diffraction intensity (relative to the zero-order signal) with temperature [51], revealing a refractive index change of $\Delta n_{\mathrm{HL}} \approx -0.02$ at $\lambda_0 = 700$ nm induced by the spin-state switching.

The possibility to monitor the SCO phenomenon through refractive index changes has also been demonstrated using surface plasmon resonance (SPR) spectroscopy [50,52,54,115]. Surface plasmons – sometimes also called surface plasmon polaritons (SPPs) – correspond to a fundamental electromagnetic mode that can propagate along the interface between a metallic material (containing free charge carriers) and a dielectric medium. This excitation, which involves a guided electromagnetic wave (polariton) coupled with the collective oscillation of surface charges in the metal (surface plasmons), can be described as a quasiparticle with discrete energy and momentum. SPP waves can be excited by incident light only under simultaneous wavevector and frequency matching conditions, which are conventionally achieved using the Kretschmann configuration [116], employing a prism as a coupling medium. For a specific combination of wavelength, incident angle, and polarization of the incident light beam, a resonance is observed, characterized by a minimum in reflectance as a function of the angle (for a given wavelength) or as a function of the wavelength (for a given incident angle). Importantly, the angular (or spectral) position of the resonance peak depends on both the refractive index and the thickness of the dielectric layer. The first experimental proof was reported by Félix et al. [50] in 2011, using a multilayer structure Ti (5 nm)/Au (45 nm)/[Fe(hptrz)$_3$](OTs)$_2$ (30 nm) deposited on a glass prism (Fig. 11a). When switching the SCO film from the LS to the HS state, the associated decrease in n leads to a shift of the SPR peak to lower angles (Fig. 11b), allowing the spin-transition curve of the film to be monitored (Fig. 11c). However, as shown in Fig. 11c, the observed SPR angular shift is the result of the combined effect of ordinary thermal expansion (as revealed by the linear slopes of the SPR angle with temperature) and the SCO (as evidenced by the change of slope around 320 K and the presence of a 3-

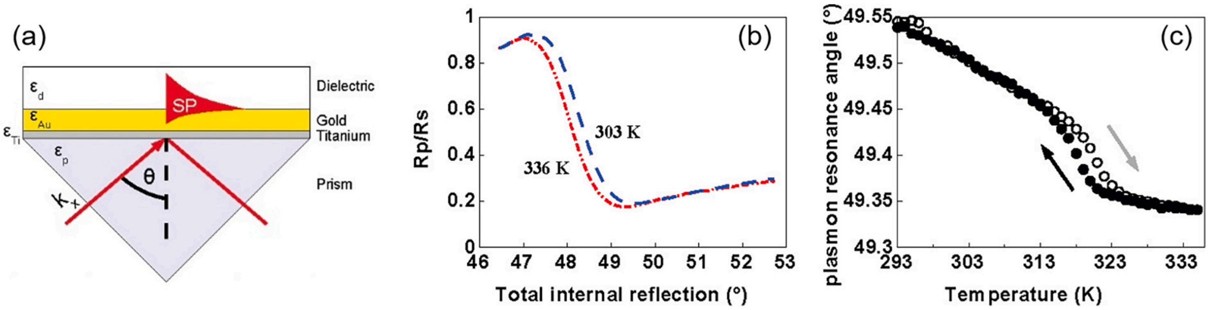

Fig. 11. (a) Schematic of a SPR device consisting in a multilayer structure Ti (5 nm)/Au (45 nm)/[Fe(hptrz)$_3$](OTs)$_2$ (30 nm) deposited on a glass prism. (b) Angle-dependent reflectance spectra of the multilayer at 303 K (LS state) and 336 K (HS state) at $\lambda_0 = 660$ nm. (c) Temperature dependence of the SPR angle (reflectance minima) in both heating and cooling modes, revealing the spin-transition curve of the SCO film. Reproduced with permission from Ref. [50].

K-wide hysteresis loop).

A similar effect was demonstrated in lithographically patterned gold nanorod arrays coated with SCO thin films [52,115], using localized surface plasmon resonance (LSPR) spectroscopy, where reversible spectral shifts of the LSPR wavelength by 2–3 nm were reported upon SCO. More recently, making use of the high refractive index change in the SCO coordination polymer [Fe(Htrz)$_2$(trz)](BF$_4$), modulation of the LSPR by up to ca. 35 nm was achieved in chemically synthesized Au@SCO core-shell nanocomposite systems [54]. By the same token, taking advantage of the capability of Au nanoparticles to efficiently convert light into heat through plasmonic heating (due to the non-radiative decay of localized surface plasmons), these authors and others [117–119] have also demonstrated a significant enhancement of the LS-to-HS photothermal switching efficiency in these systems, compared to pristine SCO particles, when exciting the SPR of the gold nanorods with low-power laser beams. Overall, these investigations based on SPR techniques – due to their high sensitivity to refractive index changes – have proven to be extremely promising for detecting and investigating the SCO phenomenon in nanoparticles and ultra-thin films down to ~10 nm in thickness, i.e., a size scale where most other characterization techniques fail.

Finally, since the vast majority of studies are conducted on large ensembles of particles or crystallites, which inevitably leads to undesired averaging effects that can blur (or hinder) some essential features, it appears crucial to investigate the SCO properties at the scale of individual, isolated nano-objects. To this aim, the use of optical microscopy techniques based on refractive index contrast, employing either interferometric (phase shift) or plasmonic principles, turns out to be very promising [120–122]. These studies are of paramount importance for a deeper understanding of the mechanisms of spin-state switching at the most fundamental level. For example, the refractive index change of the SCO compound [Fe(NH$_2$-trz)$_3$](Br$_2$)•H$_2$O (see Fig. 5a) was exploited to detect the occurrence of SCO in single microparticles (5–10 μm in size) using differential interference contrast (DIC) microscopy [120]. This technique works on the principle of interferometry between two light beams, which are spatially displaced at the sample position and recombined after transmission through the sample, to gain information about the optical path length of the studied particle. The differential signal measured in transmission is indeed proportional to the optical path length difference, i.e., to the refractive index and the geometric path length (thickness and volume) of the investigated object. Following a similar approach, even more impressive results were recently obtained by Liu et al. [121] who could study and image individual SCO nanoparticles by using surface plasmon resonance microscopy (SPRM). In this setup, a low-power 680-nm beam was used, in a Kretschmann configuration through the objective of an inverted optical microscope, to excite SPPs at the interface of a gold-coated coverslip (Fig. 12a). As shown in Fig. 12b, the interaction between the SPPs and the nanoparticle deposited on the gold surface creates a wave-like pattern in the reflected beam, which was collected using a CCD camera, and whose

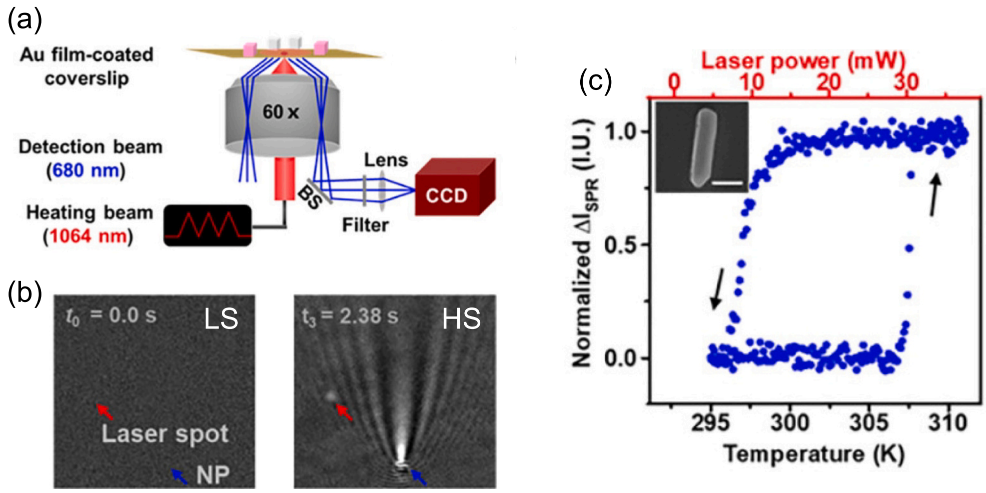

Fig. 12. (a) Schematic illustration of the surface plasmon resonance microscopy (SPRM) technique used to monitor the thermally induced spin transition of single SCO nanoparticles. A focused 1064-nm laser beam was employed to regulate the local temperature (via photoheating) of the gold surface, while detection was performed at 680 nm. (b) SPRM images of a single nanoparticle (indicated by the blue arrow) in the LS (*left*) and HS (*right*) states. (c) SPRM intensity as a function of heating laser power (*upper axis*), and the associated temperature of the particle (*lower axis*), showing a hysteresis loop between the LS and HS states. A SEM image of the studied SCO nanoparticle is shown in the inset (scale bar, 500 nm). Reproduced with permission from Ref. [121]. (For interpretation of the references to color in this figure legend, the reader is referred to the web version of this article.)

intensity depends quantitatively on the refractive index and volume of the nano-object. In this way, the SCO phenomenon could be detected and studied in single sub-micrometer-sized particles of the compounds [Fe(NH_2-trz)$_3$](Br_2) and [Fe(Htrz)$_2$(trz)](BF_4), revealing well-defined thermal hysteresis loops between the LS and HS states (Fig. 12c). Notably, this technique allowed the authors to carry out unique studies on the stability, cyclability, and spin-transition dynamics at the level of single SCO nanoparticles.

3.1.4. Additional remarks

At this stage, we shall make three important remarks. First, the relationship between the refractive index change and the fraction of LS/HS molecules might not be that simple. Obviously, the most straightforward way to relate these two quantities is to consider a linear evolution of the (measured) effective refractive index of the material, n_{eff}, with the fraction of molecules in the LS or HS state, following a simple mixing law of the form:

$$n_{eff} = X_{HS} n_{HS} + (1 - X_{HS}) n_{LS} \tag{25}$$

where X_{HS} is the fraction of HS molecules, and n_{HS} and n_{LS} are the refractive indices of the material in the HS and LS states, respectively. In fact, different effective medium theories have been developed to describe the evolution of the effective refractive index, n_{eff}, of a composite material composed of different constituents with distinct indices. The most often used theory is the Maxwell-Garnett approximation, which describes the effective index of a medium containing a collection of impurities (whose size must be small compared to the wavelength of the light) homogeneously distributed within a host matrix [123,124]. Following this simple model, it may be reasonable to describe the evolution of the effective index n_{eff} of SCO materials during the spin transition (e.g., from LS to HS) by considering the HS molecules as small inclusions (with a varying volume fraction) in a LS matrix. Within the framework of this theory, it can be shown that a linear variation of n_{eff} as a function of X_{HS} (as described in Eq. (25)) is a good approximation, provided that the difference in refractive index between the LS and HS states is not too large – which is generally the case for SCO materials. However, while the Maxwell-Garnett effective medium theory is a priori valid for SCO compounds exhibiting spatially homogenous spin conversions, it should remain a crude approach if phase separation occurs, which is typically the case for cooperative SCO solids displaying first-order spin transitions and associated hysteresis behaviors.

Second, unlike the variation in optical absorbance, which, to a good approximation, depends only on the concentration of absorbing (LS or HS) species in the material, the refractive index may change not only due to the molecular spin-state switching, but also due to ordinary thermal expansion. Indeed, to the first order of approximation, and over a small range of temperature variation (ΔT), the change in the refractive index can be written as:

$$\Delta n(T, X_{HS}) = \left(\frac{\partial n}{\partial T}\right) \Delta T + \left(\frac{\partial n}{\partial X_{HS}}\right) \Delta X_{HS} \tag{26}$$

where the first term, $\partial n / \partial T$, stands for the variation rate of the refractive index due to ordinary thermal expansion, while $\partial n / \partial X_{HS}$ denotes the variation rate of n due to SCO. The first contribution, related to ordinary thermal expansion, generally causes the measured spin-transition curves to exhibit a linear slope with temperature (as shown in Fig. 10c and 11c, for example). Therefore, to quantitatively extract the thermal evolution of X_{HS} from a refractive-index-sensitive technique, it is often necessary to correct the data for thermal expansion, which can be done by measuring the signal in the two spin states over a wide temperature range, far from the spin-transition temperature.

Finally, as a third remark, it is worth mentioning that many other optical characterization techniques can be employed to detect the SCO phenomenon [125]. Similar to UV–vis spectrophotometry, Fourier-transform infrared spectroscopy (FTIR) is commonly used to probe vibrational absorption bands in the near- and mid-infrared spectral regions. In fact, certain vibrational modes of SCO materials exhibit a significant spectral shift during the spin transition, particularly those associated with the coordination octahedron, owing to the considerable elongation of the metal-ligand bond lengths in the HS state [29]. These modes generally appear at energies below 600 cm^{-1}. Another spectroscopic technique commonly used in the SCO field is Raman spectroscopy [126], which also allows for probing vibrational changes in SCO compounds. Interestingly, it has been shown that Raman spectroscopy can be advantageously employed to investigate SCO ultra-thin films in close contact with gold nanostructures, in which case a strong exaltation of the Raman signal can be achieved through local electric-field enhancement (e.g., localized surface plasmons), a technique known as surface-enhanced Raman spectroscopy (SERS) [127]. Other spectroscopy techniques operating in different spectral ranges can also be used, such as dielectric spectroscopy [64,70] and X-ray absorption (XAS) spectroscopy [125]. Finally, it is worth noting that near-field scanning optical microscopy (NSOM) has also been employed to monitor the spin transition with high (sub-micrometer) spatial resolution, i.e., beyond the optical diffraction limit [128].

3.2. Towards photonic-based sensing applications

3.2.1. Colorimetric sensors

Since the SCO phenomenon can be triggered by a range of external stimuli, it offers significant potential for the development of diverse sensor devices based on optical detection, with the aim of monitoring changes in the physicochemical properties of the surrounding environment. Unsurprisingly, numerous applications have been proposed in the literature that exploit the color change associated with the spin-transition process. For instance, the thermo-, piezo-, vapor-, and solvato-chromic behaviors of SCO materials open up possibilities for designing smart paints, coatings, and colorimetric sensors. This scope is further amplified by the fact that the spin transition can occur gradually or abruptly, with or without hysteresis (memory effect), offering ample opportunities for innovation in practical applications [129,130]. These include real-time monitoring of the external environment (e.g., temperature, pressure, or gas/vapor concentration) or control of sample history relying on a memory effect (e.g., cold chain [131], post-hoc detection of overheating or mechanical shocks on fragile valuable objects [132], etc.).

However, although numerous preliminary studies and claims can be found in the literature, real examples of the integration of SCO materials into functional (temperature, pressure, or gas sensing) devices for quantitative measurements remain scarce [8]. For example, among the most notable achievements, one can mention the development of thermochromic sensor arrays, made from SCO-polymer nanocomposites, for the rapid visual detection of temperature variations [133]. Following the same idea, colorimetric sensors were fabricated for the real-time detection (with the naked eye) of various volatile organic compounds and hazardous gases under ambient conditions [134–138]. These chemosensors are based on the vapochromic response of various Fe^{2+} complexes, which undergo spin-state switching upon guest adsorption, inducing specific and distinguishable color changes (characterized by spectral shifts or intensity changes in optical absorption bands) depending on the guest molecules (Fig. 13a). Through quantitative color analysis – using recorded RGB (red, green, and blue) and HSB (hue, saturation, and brightness) values – the selective detection of a wide range of volatile organic molecules was demonstrated, along with the quantitative determination of their concentration levels in the atmosphere (Fig. 13) [136]. These examples highlight the potential of such SCO-based colorimetric sensors for the quantitative recognition of hazardous gases or toxic industrial chemicals (such as NH_3, HCl, HBr, and N_2H_4). Similarly, some authors have also demonstrated the fabrication of a 2D codebar (readable using a simple CMOS camera) patterned with micrometric particles of the SCO complex [Fe(L)$_2$] (LH = 2-(pyrazol-1-

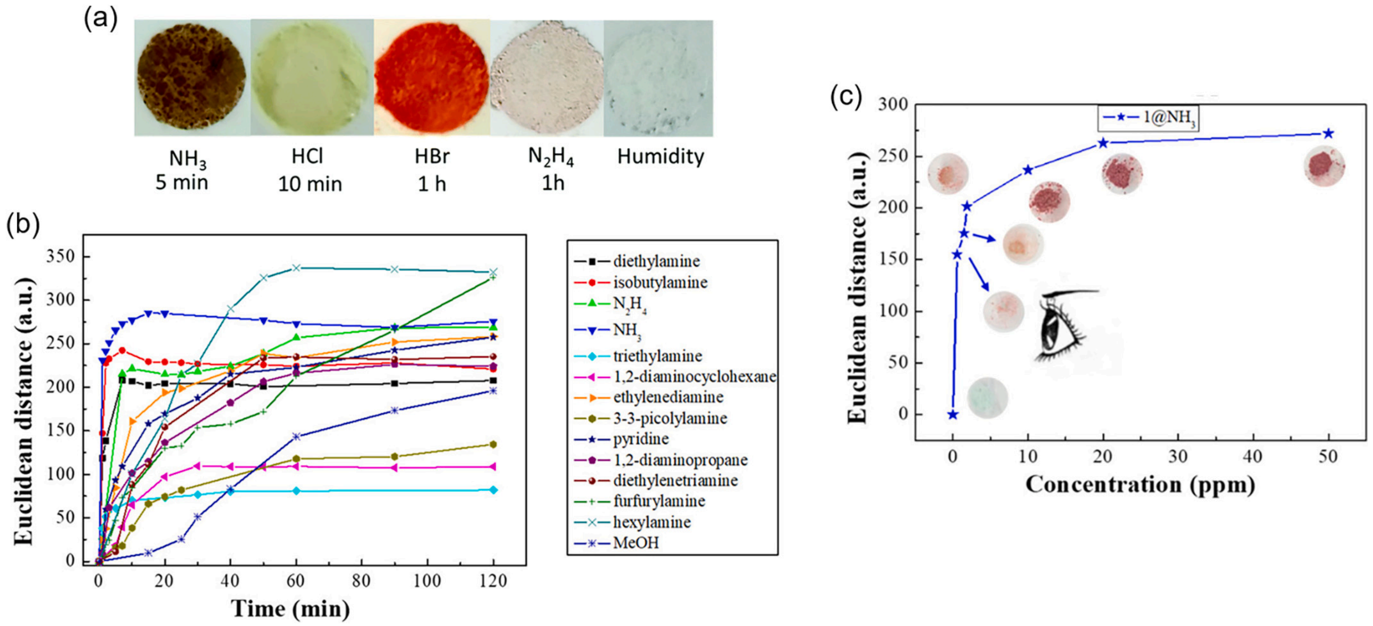

Fig. 13. (a) Images showing the vapochromic transformation of a colorimetric sensor based on the SCO complex $[Fe(trz\text{-}tet)_2(H_2O)_4]\bullet 2H_2O$ upon exposure to four toxic industrial chemicals (NH_3, HCl, HBr, and N_2H_4). Reproduced with permission from Ref. [135]. (b) Color change of the sensor over time for 14 representative volatile organic compounds at saturated concentrations, and (c) color change as a function of NH_3 concentration over 10 min at room temperature. The color changes of the sensors were quantified by recording RGB (red, green, and blue) and HSB (hue, saturation, and brightness) values, resulting in a six-dimensional color vector. The color analysis was performed by calculating the Euclidean distance (total length) between these vectors in the six-dimensional value space. The inset images in (c) illustrate the vapochromic transformation upon exposure to NH_3 at different concentrations. Reproduced with permission from Ref. [136]. (For interpretation of the references to color in this figure legend, the reader is referred to the web version of this article.)

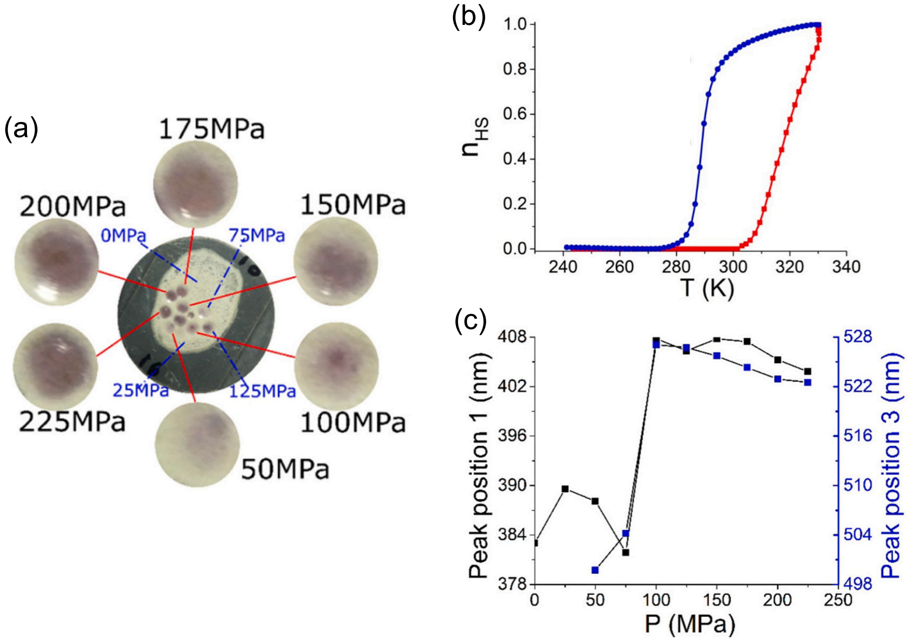

Fig. 14. (a) Selected snapshots showing the color change (from white to purple) induced by the application of local contact pressures on the SCO colorimetric sensor, resulting from the HS-to-LS transition at room temperature within the hysteresis loop shown in (b). The powder appears white in the HS state and purple/violet in the LS state. (c) Contact-pressure dependence of the spectral position of two *d*–*d* absorption bands derived from room-temperature diffuse reflection spectra, showing a sharp change around 87 MPa. Reproduced with permission from Ref. [132]. (For interpretation of the references to color in this figure legend, the reader is referred to the web version of this article.)

yl)-6-(1*H*-tetrazol-5-yl)pyridine), whose solvatochromic property was used to detect selectively ethanol and methanol [139].

Similar colorimetric sensors were also implemented to visually detect contact pressures, for example, induced by local mechanical impacts [132,140]. Such pressure sensing devices were demonstrated using the SCO complex $[Fe(hyetrz)_3]I_2{\cdot}0.5EtOH$, which exhibits a spin transition with a wide thermal hysteresis loop centered at room temperature. As shown in Fig. 14, while the sample is initially prepared in the HS state (white color), the application of an external contact pressure (above a threshold pressure value) changes the color of the sample to purple due to the HS-to-LS transition [132]. A quantitative determination of the applied pressure can be deduced from a calibration analysis (based on diffuse reflectance measurements) of the spectral position and intensity of the ligand-field *d–d* absorption bands, which are affected by the pressure impact (Fig. 14c). Moreover, since the color change is permanent (as it occurs within the thermal hysteresis loop), it allows for the localization and determination of the applied contact pressure afterward.

3.2.2. Refractive-index-based sensors

Such colorimetric approaches are generally effective at the macroscopic scale; however, their applicability diminishes at smaller size scales due to the typically low absorption coefficients of SCO compounds in the visible spectrum. For this reason, it appears that the most promising strategies for detection applications at the nanometric scale involve either refractive index sensing or luminescent doping. Recently, practical applications of SCO-induced refractive index modulation have been demonstrated for microthermometry purposes, based on the principle of thermoreflectance imaging (i.e., the change in specular optical reflection with temperature) of surfaces coated with SCO nanometric thin films. As shown in Fig. 15, this thermometric application was demonstrated using SCO thin films deposited on metallic microwires, heated by Joule effect [97,101,114,141,142]. Notably, the use of different complexes with distinct SCO behaviors allows for the development of diverse thermometric functions and thermal imaging approaches, depending on the abruptness of the thermally induced spin-state conversion or the presence/absence of a thermal hysteresis loop (memory effect).

As an example, a thin film of the SCO compound $[Fe(Htrz)_2(trz)](BF_4)$, which exhibits a large thermal hysteresis loop, was used to acquire ex situ images of fast (μs) transient heating events by optical reflectivity (Fig. 15a) [141]. In this context, the thermal memory effect is particularly advantageous because it allows for the detection of temperature changes retrospectively using high-resolution imaging techniques. This approach is ideal for investigating rapid and spatially localized transient thermal events that are difficult to capture with real-time optical methods. Conversely, the absence of a thermal hysteresis loop allows for real-time thermometry applications. In this case, employing a SCO film with an abrupt thermal transition enables real-time binary detection of the surface temperature, as a sudden change in optical reflectivity occurs at the spin-transition temperature, thereby defining a clearly delineated isotherm. As shown in Fig. 15b, this approach was demonstrated using vacuum deposited thin films of the SCO complex $[Fe(HB(1,2,4\text{-triazol-1-yl})_3)_2]$, which displays an abrupt spin transition centered at 64 °C, allowing clear-cut isotherms to be displayed on the surface [114]. As demonstrated in this study, this approach can be used to record real-time contour maps of the surface temperature without the need for any prior thermal calibration of the surface reflectivity. Finally, using another SCO complex, $[Fe(HB(1,2,3\text{-triazol-1-yl})_3)_2]$, exhibiting a gradual thermal SCO, continuous and real-time mapping of the surface temperature was achieved (Fig. 15c), provided that careful thermal calibration of the optical reflectivity change was performed beforehand [97]. Overall, based on this SCO-enhanced thermoreflectance approach, the capability to map surface temperature distributions with sub-μm spatial resolution, μs temporal resolution, and 1 °C thermal resolution has been demonstrated [97,114]. In all these examples, and in contrast to conventional thermoreflectance microscopy techniques, the presence of the SCO thin layer on the studied surface significantly increases the relative change in optical reflectivity with temperature, $\Delta R/R$, due to the modification of the refractive index upon the SCO, even within the visible spectral range. In other words, the SCO film leads to a significant enhancement of the thermoreflectance coefficient, $\kappa = \mathrm{d}(\Delta R/R)/\mathrm{d}T$, (i.e., the thermal sensitivity), by up to a factor of ten compared to uncoated surfaces [97]. This gain in sensitivity offers the possibility of mapping surface temperature distributions using a simple CCD-based optical detection system, making this SCO-based approach a versatile and cost-effective thermal imaging method. Note that this microthermometry application was also demonstrated using thin films of various SCO complexes from the Fe-triazole family doped with organic luminophores, where the detection was instead based on the modulation of the luminescence signal induced by the spin transition [101,143].

As certain SCO compounds (such as porous MOFs) exhibit a shift in the spin-state equilibrium upon the absorption/desorption of guest molecules, they can also be implemented for chemical sensing applications [144,145]. The development of gas sensor materials holds significant relevance owing to their potential applications in various fields, such as environmental monitoring, home safety, the automotive industry, and indoor air quality management. Following this idea, tunable micrometric gratings of microporous SCO MOFs were fabricated using a combination of photolithography and multilayer assembly methods to quantitatively follow the concentration of different analyte molecules [51,146]. The detection is achieved by monitoring the first-order diffraction efficiency change of the SCO grating in response to refractive index variations and/or grating geometry modulation caused by the guest-induced change of the molecular spin state. As an example, as shown in Fig. 16, lithographically patterned diffraction gratings of the SCO compound $\{Fe(bpac)[Pt(CN)_4]\}$ were successfully developed to assess the atmospheric concentration of different halogenobenzene molecules [146].

It is worth noting that the inclusion of guest molecules into the porous MOF structure inherently leads to a rise in the mass density of the system, so that the refractive index increases accordingly. This effect, which obviously also occurs in SCO-inactive materials, forms the basis of the operational principles of many diffraction-based sensors. In this context, SCO materials may offer several advantages, including enhanced selectivity and improved sensitivity, due to the substantial change in the refractive index upon the spin-state switching [146].

4. Spin-crossover-based tunable photonic devices

The previous section was dedicated to photonic-based sensing devices, which rely on the modification of the complex refractive index of SCO materials to quantitatively detect and monitor physicochemical changes in the external environment. Conversely, an applied perturbation can also be used to trigger the SCO phenomenon, with the aim of inducing a controlled modulation of a light signal between an optical OFF-state and an optical ON-state in a photonic switch-type device. In fact, in the vast fields of optics and photonics, this tunability turns out to be a major asset, which is highly demanded for various applications [147,148]. These include, for example, dynamic displays, optical memories, spatial light modulators (e.g., beam steering, holographic displays, distortion correction) [149], photonic integrated circuits (e.g., optical switches, modulators, filters, limiters) [150], optical neural networks, and other approaches for optical computing and telecommunication. To achieve these active functionalities, there is currently a need for materials with switchable optical properties, i.e., materials exhibiting controllable complex refractive indices [148].

In this context, SCO (nano)materials may constitute an attractive family of switchable molecular compounds for use as active elements in tunable photonic devices. Although this aspect has not been extensively explored until now, it could see significant development in the coming years, supported by recent advancements in the processability and integration of SCO nano-objects into devices, alongside widespread access to nanotechnology tools. In the present section, we review the current state of the art in the development of SCO-based tunable photonic devices used to manipulate light propagation. The overall performance of SCO materials for optical modulation will be discussed and compared with those of commonly used phase-change materials (PCMs). Notably, it will be shown that, for certain applications, SCO nanomaterials emerge as promising candidates for implementing optical tunability in the visible spectral range, where most conventionally used PCMs present severe limitations. Finally, we will see that original light-

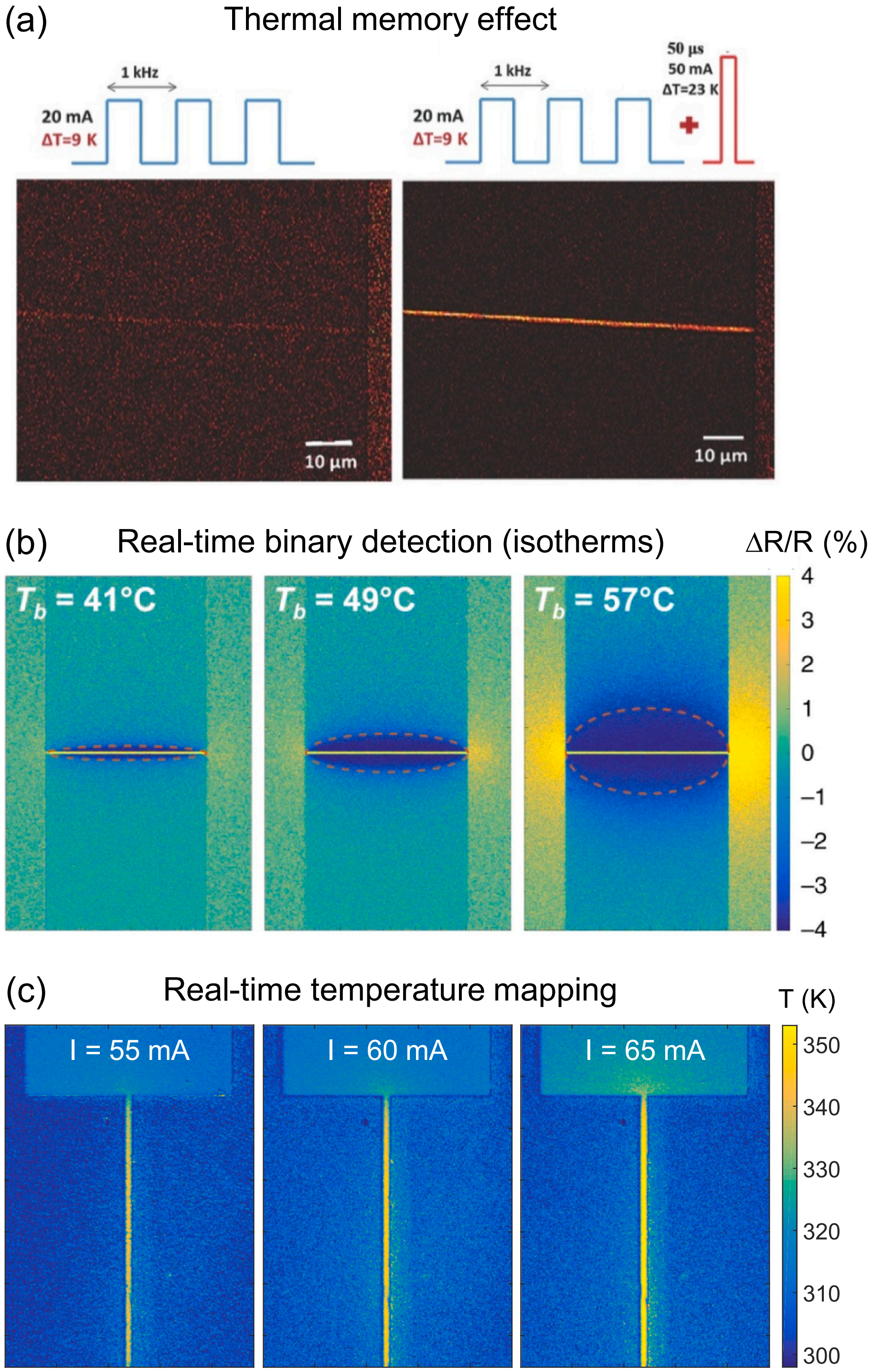

Fig. 15. Surface temperature mapping of Joule-heated microwires using SCO-enhanced thermoreflectance microscopy. (a) Optical reflectivity images of a microwire coated with a thin film of the SCO complex [Fe(Htrz)$_2$(trz)](BF$_4$) displaying a large thermal hysteresis loop, (*left*) after normal operation of the device (applied AC current of 20 mA) and (*right*) when a single current spike (50 µs, 50 mA) was added to the AC current to mimic an erratic heating event. A clear change in optical reflectivity on the wire is observed in the latter case, indicating overheating. Reproduced with permission from Ref. [141]. (b) Contour maps of the surface temperature acquired in real-time by optical reflectivity using a thin film of the SCO complex [Fe(HB(1,2,4-triazol-1-yl)$_3$)$_2$] at different base temperatures T_b of the device. As the complex exhibits an abrupt spin transition at 64 °C, sharp variations in optical reflectivity are observed at the transition temperature, delineating well-defined isotherms (indicated by red dotted lines). Reproduced with permission from Ref. [114]. (c) Temperature maps of the microwire for various applied electrical currents, recorded using a thin film of [Fe(HB(1,2,3-triazol-1-yl)$_3$)$_2$], which undergoes a gradual thermal SCO, enabling continuous real-time mapping of the surface temperature. Reproduced with permission from Ref. [97]. (For interpretation of the references to color in this figure legend, the reader is referred to the web version of this article.)

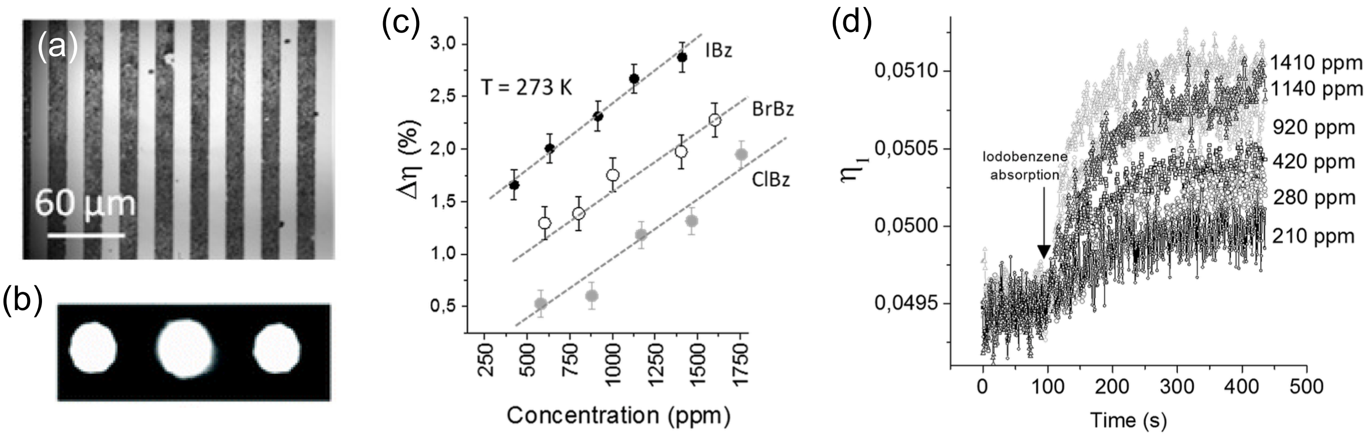

Fig. 16. (a) Optical microscopy image of a surface-relief grating of the SCO compound {Fe(bpac)[Pt(CN)$_4$]} (grating period: 30 μm, line width: 15 μm, line thickness: 80 nm). (b) Typical diffraction pattern of the grating showing the zero-order and first-order diffracted spots. (c) Variation of the diffraction efficiency (η) as a function of the concentration of chloro-, bromo-, and iodo-benzene molecules in the atmosphere. (d) Time evolution of η under different concentrations of iodobenzene (the black arrow indicates the moment when the gas was injected into the sample chamber). Reproduced with permission from Ref. [146].

matter coupling phenomena can also be exploited when SCO molecules are integrated into specifically designed resonant optical cavities, opening new and promising prospects – still largely unknown and unexplored – for manipulating molecular properties (including possibly the SCO properties) through the electromagnetic environment surrounding the molecules.

4.1. Spin-crossover-based photonic switch-type devices

The first optical switching device based on SCO compounds was developed by Kahn and co-workers [38,39] more than 30 years ago for data storage and display applications. The fabricated device used a layer of a SCO compound from the Fe-triazole family, known for its wide (60 K) thermal hysteresis loop, deposited on top of an alumina plate on which addressable resistive dots and connecting electrodes were screen-printed (Fig. 17a). When electrically addressed, the dots act as localized heat sources, enabling the molecular spin state to switch from LS to HS, accordingly changing the color of the SCO layer from violet to white. The information is stored as long as the temperature of the system remains within the hysteresis loop. To erase the information, the temperature must be reduced below the HS-to-LS switching point, which can be achieved using an integrated Peltier element. As shown in Fig. 17b, other related displays were developed based on the same principle [151]. Moreover, building on the same idea, it is worth mentioning that the color change of SCO materials has also been exploited for the development of commercially available display solutions, such as smart inks, pigments, and paints [152], as well as for the design of tunable floor coatings (for applications in the construction sector, for example) [153]. Many of these applications have been patented.

These pioneering macroscopic devices and applications, which primarily used microcrystalline powder samples, relied on optical absorbance detection and thermal addressing. However, these two principles are conceptually incompatible when it comes to device size. At larger scales, slow heat dissipation becomes a limiting factor, while the typically low absorption coefficients of SCO materials in the vis-NIR spectral regions pose significant challenges at reduced scales. This apparent incompatibility between optical contrast and nanometric size makes it difficult, if not impossible, to develop technological devices based on the color change. Alternative approaches are therefore needed at the nanometric scale. In this context, much efforts have recently been deployed towards the development of micro- and nanoscale SCO devices based rather on the refractive index change (for manipulating light

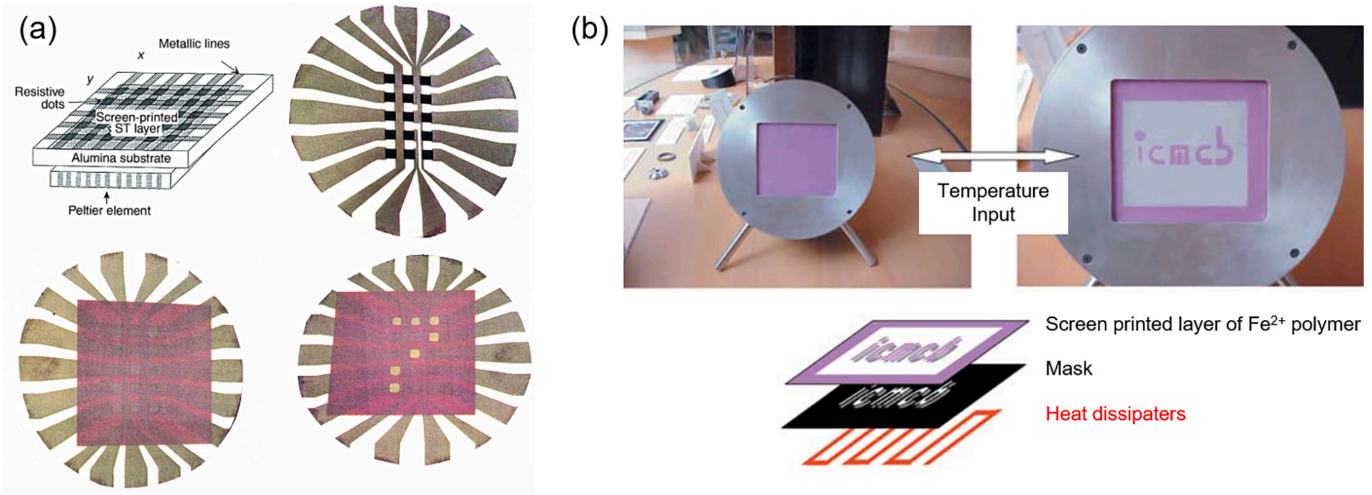

Fig. 17. (a) Principle of a display device using a SCO compound as active element. The device consists of a SCO layer deposited on top of a substrate made of an alumina plate, onto which resistive dots and connecting electrodes were previously screen-printed. The dots, which serve as heat dissipators, are electrically addressed through columns and rows. Reproduced with permission from Ref. [39]. (b) Another SCO-based display device, shown before (*left*) and after (*right*) thermal writing. Reproduced with permission from Ref. [151].

propagation), and requiring high transparency in both spin states.

The first photonic switch-type device, based on the SCO-induced change in the refractive index, was reported in 2006 by the Freysz group [59]. The device is a one-dimensional (1D) photonic crystal (Bragg grating) operating in the sub-millimeter wavelength (THz frequency) range. It consists of a periodic structure of alternating layers of glass (170 μm) and air (350 μm), with the SCO material $[Fe(NH_2\text{-}trz)_3](Br_2)\bullet H_2O$, in the form of microcrystalline powder, inserted as a defect layer (Fig. 18a). By switching the molecular spin state, a 15-GHz shift in the defect mode frequency (around 0.255 THz) was observed in this device (Fig. 18b), which thus operates as a tunable SCO-based THz filter.

In this last example, the use of a SCO microcrystalline powder is not problematic, as it does not cause significant scattering losses (because the wavelength of light in the millimeter range is much larger than the average size of the microcrystallites). By contrast, the design of photonic switching devices operating in the vis-NIR ranges requires high-quality, low-loss (i.e., minimal absorption and scattering) SCO nano-objects. In this context, recent advancements in the development of SCO nanomaterials in a variety of forms, such as nanoparticles, thin films, nanopatterns, and nanoheterostructures [8,154,155], have significantly enlarged the scope of their integration into different types of devices (e.g., optical resonators, gratings, waveguides), thereby expanding their spectral range of application.

Among recent major advances, an attractive approach aims at synthesizing (nano)composite materials consisting of SCO (nano)particles embedded in a polymer matrix [156]. Based on this strategy, polymer optical waveguides incorporating SCO nanomaterials were recently implemented [157] with the aim of modulating the transmitted optical signal. As an example, microparticles of the SCO complex $[Fe(NH_2\text{-}trz)_3](Br_2)$ were integrated into multi-mode and single-mode optical waveguides, either by mixing the particles with the epoxy core of the guides or by depositing them onto the surface of the core [158]. Following this approach, the authors demonstrated noticeable variations in the transmitted optical signal of the waveguides upon the SCO. In these types of waveguide structures, the modulation of the optical signal can occur due to changes in the absorption spectrum of the SCO particles, as well as due to changes in their refractive index when the particles are in close contact with the waveguide core and interact with the evanescent field of the propagating light. However, it is important to emphasize that this approach, which relies on the use of nanocomposite materials, may encounter inherent limitations due to scattering losses caused by the presence of the particles. Therefore, a compromise must be achieved between the size and concentration of active particles to enable significant signal modulation while minimizing scattering losses. Still, the actual magnitude of the effective refractive index change in nanocomposite materials upon the SCO remains largely unexplored so far.

Based on recent progress in nanofabrication, another strategy involves incorporating SCO nanometric thin films into nanocavities to tune optical resonances in the visible spectral range. In this view, an active plasmonic device was fabricated, consisting of lithographically patterned gold nanorod arrays coated with a 60-nm-thick film of the SCO compound $[Fe(hptrz)_3](OTs)_2$ (Fig. 19a) [115]. In this device, a reversible blueshift of the LSPR wavelength by 2–3 nm was recorded in the visible domain (around 700 nm) upon the thermally induced LS-to-HS transition, in response to the refractive index change of the SCO film. Interestingly, the plasmonic resonance can also be tuned via a photothermal effect (plasmonic heating), by turning ON/OFF a laser beam incident on the nanorods (Fig. 19b). This device represents the first example of a photonic switch-type structure displaying wavelength-tunable resonances in the visible spectrum driven by the SCO phenomenon.

Pursuing this strategy, thin films of sublimable SCO complexes, deposited by thermal evaporation under vacuum [159], have also emerged as promising switchable elements for integration into photonic devices due to their high purity, low surface roughness, and tightly controllable nanometric thickness. For instance, thin films of the evaporable complex $[Fe(HB(1,2,4\text{-triazol-1-yl})_3)_2]$ have been utilized in metal-based Fabry-Pérot cavities, where the molecular SCO film is inserted between two parallel reflecting Ag mirrors [Ag (50 nm)/SCO (115 nm)/Ag (50 nm)] (Fig. 20a) [55]. Such Fabry-Pérot cavities are widely used in various optical devices, including spectrometers, lasers, and filters, among others [160]. Within this structure, incident light undergoes multiple reflections between the two metal mirrors, leading to constructive interference between the reflected beams, which results in the formation of optical standing waves (i.e., resonance modes) within the SCO layer at well-defined wavelengths. For these specific wavelengths, the device behaves as an optical resonator, characterized by distinct resonance peaks in both the transmission and reflection spectra. The corresponding resonance wavelengths, λ_{res}, at normal incidence, depend on the distance L between the two mirrors and the refractive index n of the dielectric medium between them, as described by the formula:

$$\lambda_{res} = \frac{2nL}{m} \tag{27}$$

where m is an integer. The cavities in Ref. [55] were designed with resonances in the green part of the visible spectrum (at normal incidence) and quality factors Q of ca. 30. As displayed in Fig. 20b and c, the reflectance spectra reveal that the LS-to-HS state switching of the SCO film gives rise to a reversible blueshift of the cavity resonance (by ~4 nm, excluding the contribution of ordinary thermal expansion) in response to the refractive index change of the SCO material in this spectral region ($\Delta n_{\text{HL}} = -0.05$). As a result of this resonance spectral shift, a maximum change in optical reflectance of $\Delta R = 25$ % between the LS and HS states was achieved in this device. Importantly, the quality factor (i.e., the resonance linewidth) of the cavity remains unchanged

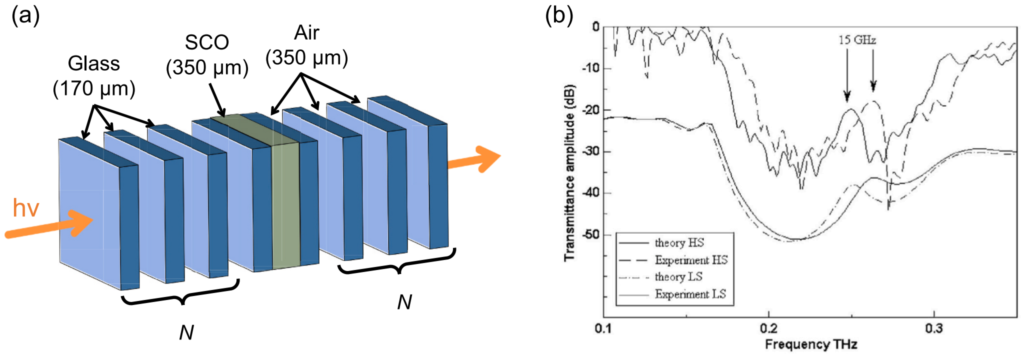

Fig. 18. (a) Schematic of a SCO-based one-dimensional photonic crystal operating in the THz frequency range, with the SCO compound inserted as a defect layer. (b) Experimental transmission spectra of the device in the two spin states, showing a 15-GHz shift in the defect mode frequency upon the spin-state switching. Solid lines show the result of theoretical calculations (shifted by 20 dB for clarity). Reproduced with permission from Ref. [59].

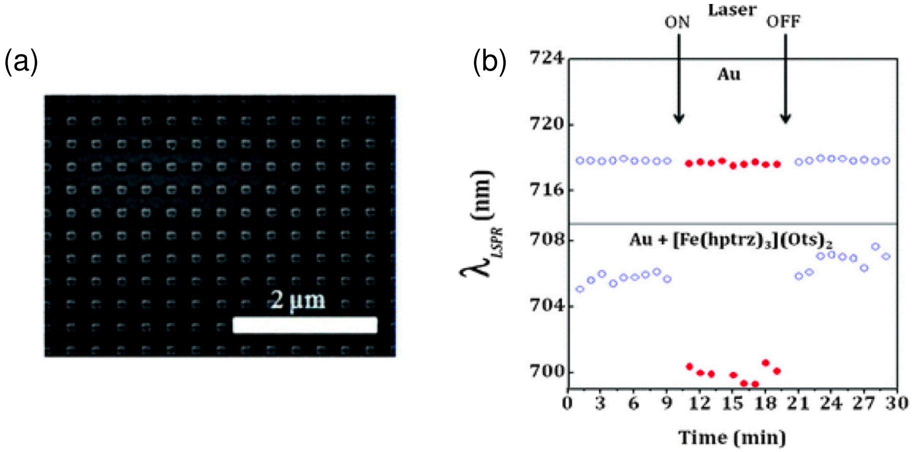

Fig. 19. (a) SEM image of a gold nanorod array fabricated by electron beam lithography, displaying plasmonic resonance (LSPR) in the visible spectrum (around 700 nm). (b) Variation of the plasmonic resonance wavelength when turning ON/OFF a 633-nm laser beam (spectrally overlapping the plasmon resonance) on (*top panel*) a pristine gold nanorod array and (*bottom panel*) an array covered with a 60-nm-thick SCO layer. No effect is observed on the pristine gold array, while a reversible blueshift of the resonance wavelength is evidenced under laser irradiation in response to the refractive index change of the SCO film induced by the photothermal spin transition. Reproduced with permission from Ref. [115].

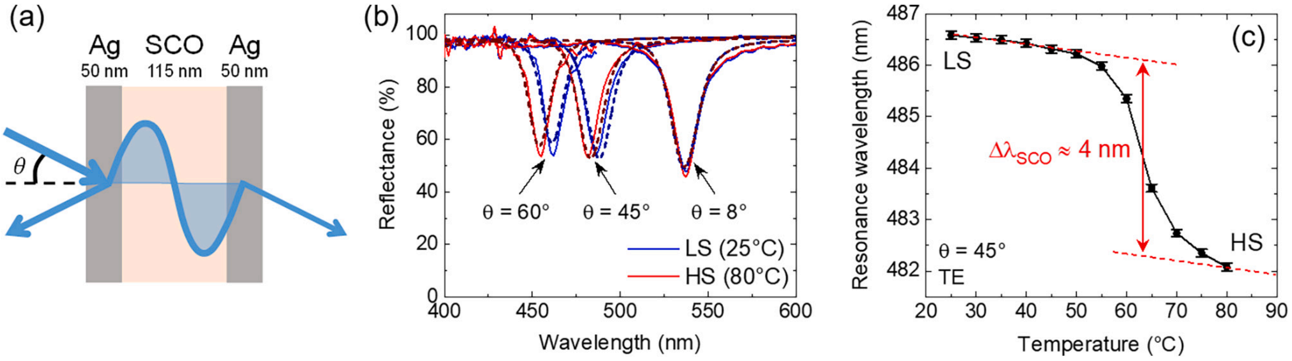

Fig. 20. (a) Schematic of a SCO-based Fabry-Pérot cavity consisting of a thin film of the SCO complex [Fe(HB(1,2,4-triazol-1-yl)$_3$)$_2$] incorporated between two parallel Ag mirrors. (b) Reflectance spectra of the cavity at selected angles of incidence (θ) in the two spin states. (c) Temperature evolution of the cavity resonance wavelength at a fixed angle of incidence ($\theta = 45°$), revealing a blueshift of the resonance peak by approximately 4 nm upon the LS-to-HS transition. Adapted with permission from Ref. [55].

during the spin transition due to negligible absorption losses in the SCO layer in both spin states.

It is important to mention, however, that the volume expansion of the SCO material during the transition inevitably leads to a variation in the sample thickness as well. From Eq. (27), it can be observed that the increase in the SCO layer thickness, L, will compensate for the drop in the refractive index to some extent. In fact, for the compound [Fe(HB(1,2,4-triazol-1-yl)$_3$)$_2$], it appears that the relative change in the refractive index during the LS-to-HS transition, $\Delta n_{\mathrm{HL}} / n_{\mathrm{LS}} = -3.9$ %, is fully counterbalanced by the concomitant expansion of the film thickness, $\Delta L_{\mathrm{HL}} / L_{\mathrm{LS}} = 4.6$ %, resulting in no discernible spectral shift of the cavity resonance at normal incidence along the SCO process (see Fig. 20b) [55]. However, as the angle of incidence, θ, is increased, the cavity mode progressively acquires a non-zero in-plane wavevector component, $k_{\parallel} = (2\pi/\lambda_0) \times \sin(\theta) \neq 0$, making it less 'sensitive' to the (out-of-plane) volume change. As a consequence, the largest spectral shifts of the resonance peak are observed at large incident angles (see Fig. 20b).

Bearing in mind this effect, another tunable optical resonator was designed using the same SCO compound, which consists of a Ag (35 nm)/SCO (162 nm) bilayer structure deposited on a glass prism (Fig. 21a) [56]. Although this structure resembles a conventional SPR setup, the use of a relatively thick SCO layer allows for the excitation of electromagnetic modes in the visible domain (with either transverse magnetic (TM) or transverse electric (TE) polarized light), which are not of plasmonic origin, but correspond to the formation of resonant standing waves within the SCO film (similar to a Fabry-Pérot cavity). Due to the use of the coupling prism, optical modes with large in-plane wavevectors can be excited, resulting in an increased sensitivity, $d\lambda_{res}/dn$, of the resonance wavelength to refractive index changes in the SCO layer. As depicted in Fig. 21b and c, a large reversible spectral shift of the resonance of up to 30 nm was reported, associated with a reflectance contrast between the LS and HS states as large as $\Delta R = 70$ %. Interestingly, the tuning of the resonance wavelength was also demonstrated through photothermal effects at $\lambda_0 = 532$ nm. In particular, the large spectral shift of the resonance at the transition was found to give rise to a photothermal nonlinearity that could be leveraged for achieving an optical (self-)limiting application (Fig. 21d). Such optical limiting devices are typically used for protection of equipment and humans against hazardous high-power light beams, for example [161].

In the different photonic switching devices presented above, the modulation of the optical signal is based on the SCO-induced tunability of an optical resonance at a well-defined wavelength, which limits the spectral bandwidth of the devices to only a few nanometers. Therefore, to enhance the applicability of SCO compounds, other devices with different geometries and operating principles will have to be considered in order to enlarge the operating spectral bandwidth, while maintaining good performance in terms of optical modulation depth. In this regard,

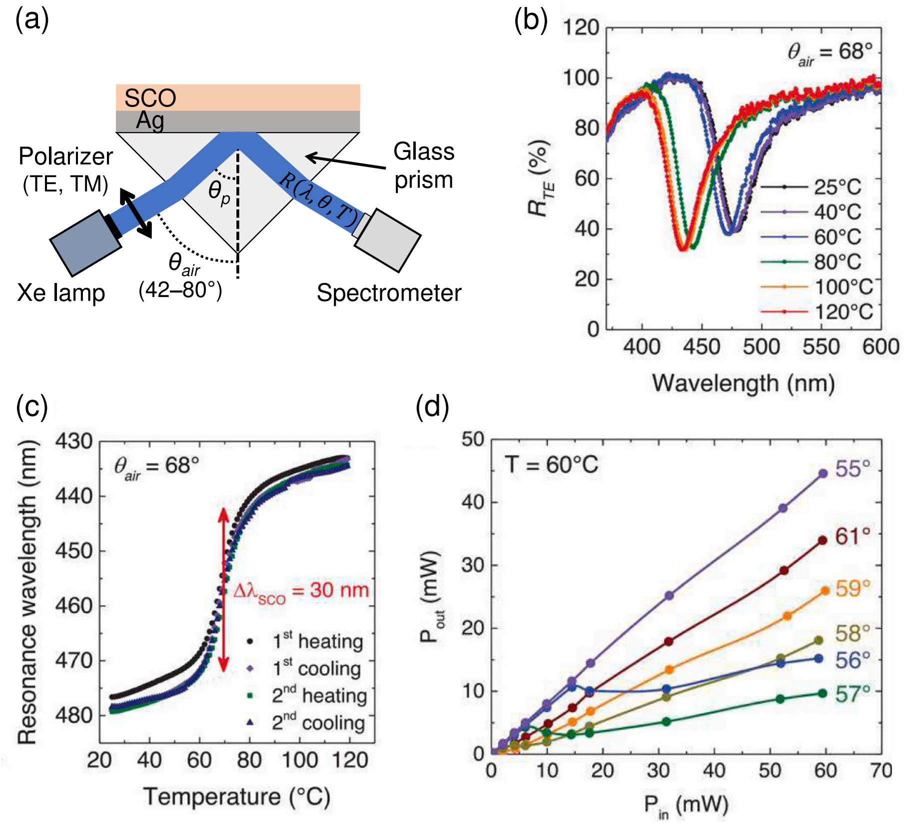

Fig. 21. (a) Schematic of an optical resonator consisting of a Ag (35 nm)/SCO (162 nm) bilayer deposited on a glass prism, excited using the Kretschmann method. (b) Reflectance spectra of the resonator acquired at selected temperatures (TE polarization, $\theta_{\text{air}} = 68^\circ$), showing a blueshift of the resonance peak upon the LS-to-HS transition. (c) Temperature dependence of the resonance wavelength over two heating-cooling cycles at a fixed angle of incidence (68°). (d) Laser ($\lambda_0 = 532$ nm) power reflected by the device as a function of the incident power, measured at different angles of incidence, revealing a nonlinear optical limiting behavior (for an appropriate choice of incidence angle and laser power) induced by the photothermal shift of the resonance peak. Reproduced with permission from Ref. [56].

recent numerical simulations have demonstrated the potential to develop SCO-based modulators by exploiting changes in total internal reflection conditions at interfaces, which could enable broadband, high-contrast switching operations [162].

4.2. Can spin-crossover nanomaterials be really competitive? Comparison with other phase-change materials (PCMs)

Recently, in the 'active photonics' context, considerable research has been devoted to so-called phase-change materials (PCMs), which exhibit reversible and significant changes in their optical properties as they undergo solid-solid electronic and/or structural phase transitions [163–170]. The most widely used solid-solid PCMs are chalcogenide alloys (e.g., $Ge_2Sb_2Te_5$ (GST)), which undergo amorphous-crystalline phase transitions, and whose main application has been in rewritable optical storage technology [171–173], and transition metal oxides (e.g., VO_2), which exhibit metal-insulator transitions [164,174,175]. These materials have been pivotal in the development of reconfigurable photonic devices (mainly operating in the NIR spectral domain) such as optical memories, spatial light modulators, and photonic integrated circuits [148,176,177].

It is important to recognize that the requirements for a PCM are not the same depending on the targeted application, and a single material cannot meet all specific needs and constraints. Besides the obvious requirement for a large refractive index modulation, Δn, other potentially important assets include fast switching speeds in both directions and good reversibility over a large number of switching cycles (see Table 4). While most of these requirements can be readily fulfilled by existing PCMs, an important bottleneck arises due to high transmission losses [178]. Indeed, one of the key factors in integrated optics is minimizing absorption and/or scattering losses. While thin films can exhibit low absorption losses due to short propagation lengths (< μm), integrated optics typically involves much longer propagation lengths (~ cm), so that an excellent transmittance of the employed materials becomes mandatory. Most of the known PCMs, such as VO_2 or GST, exhibit high extinction coefficients ($k_{min} > 0.5$–1) within the vis-NIR ranges in at

Table 4
Comparison of key requirements for optical tunability in the visible spectral domain (at 500 nm) among different classes of all-solid PCMs, including metal-insulator transition materials (e.g., VO_2) and chalcogenide alloys (e.g., GST), with those of SCO materials (e.g., [Fe(HB(1,2,4-triazol-1-yl)$_3$)$_2$]).

Main requirements	Transition metal oxide (VO_2)	Chalcogenide alloy (GST)	SCO material [Fe(HB(1,2,4-triazol-1-yl)$_3$)$_2$]
Large refractive index change $\lvert\Delta n\rvert$	0.5 [179]	0.6 [180]	0.05 [56]
Fast switching speed	≈ 1 ns [181]	≈ 20–50 ns [182]	≈ 10 ns [46]
High switching endurance	10^7 cycles [175]	10^4 cycles [183]	> 10^7 cycles [114]
Low extinction coefficient k_{min}	0.6 [179]	1.9 [180]	< 10^{-3} [56]
FOM_2	0.83	0.32	50

least one of their two phases (implying large attenuation losses), and thus remain unsuitable for operation in these spectral domains [178]. Therefore, the development of new PCMs with high transparency in the vis-NIR regions is crucial for a broad range of applications.

In this regard, as summarized in Table 4, although the refractive index change of SCO materials is relatively modest in comparison with other conventionally used PCMs, some SCO materials appear to be fully competitive in terms of switching speed (around 10 ns [46]) and switching endurance ($> 10^7$ cycles [114]), as is the case for the SCO compound [Fe(HB(1,2,4-triazol-1-yl)$_3$)$_2$]. Notably, many SCO materials offer a significant advantage which is the low propagation losses in the vis-NIR spectral ranges, due to their low absorption coefficients ($\alpha < 200\ \text{cm}^{-1}$, i.e., $k < 10^{-3}$).

In optical switching devices incorporating conventional PCMs, it is important to emphasize that the modulation of the optical signal relies on both the switching of the real part of the PCM refractive index, Δn (phase modulation), and the variation of the extinction coefficient, Δk (amplitude modulation). In general terms, the performance of an active PCM used for optical modulation can be quantified using the following, generic figure-of-merit (FOM):

$$FOM_1 = \frac{\sqrt{(\Delta n)^2 + (\Delta k)^2}}{k_{min}} \tag{28}$$

where Δn and Δk represent the changes in the real and imaginary parts of the refractive index induced by the phase transition, while k_{min} denotes the extinction coefficient of the active material in its low-absorbing phase. A large value of k_{min} necessarily implies high transmission losses, which thus restrain the achievable optical modulation depth of the device. In the case of specific applications that require only phase modulation in optical switches/modulators without amplitude modulation (i.e., with low attenuation losses), the relevant FOM becomes [184]:

$$FOM_2 = \frac{\Delta n}{k_{min}} \tag{29}$$

While the FOM$_2$ values are around 25 and 10 in the NIR (at 1550 nm) for GST and VO$_2$, respectively, they drop to less than 1 in the visible domain for both materials, due to the high values of k in both phases ($k_{min} > 0.5$). In comparison, some SCO materials, such as [Fe(HB(1,2,4-triazol-1-yl)$_3$)$_2$], exhibit a FOM$_2$ of around 50 over the whole visible spectrum, indicating that they can surpass commonly used PCMs in terms of phase modulation capabilities in low-loss devices. It is worth mentioning that the compound Ge$_2$Sb$_2$Se$_4$Te$_1$ (GSST), which has been recently proposed as a low-loss alternative to GST (where Te is partly substituted by Se), still suffers from a poor FOM$_2$ (< 3) in the visible domain [184,185]. Interestingly, the large optical bandgap sulfide-based chalcogenide, Sb$_2$S$_3$, shows an improved FOM$_2$ compared to [Fe(HB(1,2,4-triazol-1-yl)$_3$)$_2$] (due to negligible absorption in its amorphous phase and a large Δn of the order of unity), but only for wavelengths above 600 nm [186,187]. Although this FOM$_2$ does not reflect the universal applicability of PCMs in tunable photonic devices, it nevertheless suggests that certain SCO materials, owing to their low optical absorption in both phases, can outperform well-established PCMs in specific applications (e.g., phase modulation) that require broadband transparency in the visible spectral domain [56]. As a matter of fact, it has been demonstrated [56] that the figures-of-merit of the fabricated SCO-based optical resonators, in terms of tunability (resonance spectral shift, optical modulation depth, etc.) in the visible range, are fully comparable to those reported for resonators incorporating conventional PCMs operating in the NIR ($\lambda_0 \approx 1550$ nm) [164,165].

Most of the SCO-based tunable photonic devices fabricated so far are based on thermal addressing, and can therefore be considered as implementations of thermo-optic switches. Thermo-optic switching utilizes the temperature dependence of the refractive index of a material, quantified by the so-called thermo-optic coefficient (TOC), dn/dT, to realize optical switching functionality [188–190]. The most widely considered materials for fabricating thermo-optic devices include polymers (e.g., poly(methyl methacrylate), polyurethane, polyimide, etc.), perovskite oxides (e.g., LiTaO$_3$, BaTiO$_3$, etc.), and silicon-based materials (e.g., Si$_3$N$_4$, SiO$_x$, 4H-SiC, etc.) [189]. Compared to these materials, SCO compounds generally exhibit high TOCs across wide spectral domains, but over a limited temperature range around the spin-transition temperature. In fact, the thermo-optic response can vary significantly from one SCO compound to another, depending on the abruptness of the thermal spin transition. As an example, thin films of the complex [Fe(HB(1,2,4-triazol-1-yl)$_3$)$_2$], which undergo a relatively abrupt transition around 64 °C, exhibit an average TOC of $dn/dT \approx -2 \times 10^{-3}\ \text{K}^{-1}$ in the visible range, i.e., one to two orders of magnitude greater than that of materials usually considered [56], but over a narrow temperature range of ~ 20 °C centered around the transition temperature. As discussed in a recent paper [56], beyond their high TOC near the switching temperature, SCO materials compare favorably to other materials commonly used in thermo-optic switches, as they offer high heating efficiency (power × time constant) for optical modulation [191] and, thus, relatively low power consumption.

Overall, all the features discussed here suggest that the use of SCO nanomaterials in the field of tunable photonics has a promising future, provided that they can be adapted to enter the realm of integrated photonics fabrication platforms and enable energy-efficient switching at ultrafast frequencies.

4.3. Towards intriguing strong light-matter coupling effects

In the SCO-based optical resonators presented in section 4.1, the resonance peaks were located in the visible spectral range, where the SCO compounds under study are virtually transparent in both spin states. Therefore, aside from the phase modulation of the propagating optical waves within the cavity induced by the change in n, no other interaction occurred between the resonant cavity and the SCO material. The situation is different, however, when one optical mode of the cavity is tuned to be in resonance (i.e., at the same frequency) with a transition between two quantum states of the molecules, characterized by its transition dipole moment $\boldsymbol{d}$. In this case, the optical field and the molecular transition can be regarded as two oscillators in resonance, which can interact with each other by exchanging energy. Such interaction with light can profoundly modify the properties of materials when it occurs inside an optical cavity, wherein the electromagnetic field is confined. Indeed, the light-matter interaction term, g, which is given (in the dipole approximation) by:

$$g = -\boldsymbol{d}\cdot\boldsymbol{E} \tag{30}$$

where $\boldsymbol{E}$ is the confined optical field, can be particularly large in optical cavities due to the enhanced electric field density associated with resonant modes.

If the light-matter interaction term, g, remains moderate, the system undergoes only weak perturbations: transitions (absorption/emission) between energy levels can be promoted, but the energy levels themselves of the material remain essentially unchanged beyond their original linewidths. This is defined as the *weak-coupling regime* [192]. This regime is characterized by an enhancement of the quantum spontaneous emission rate of the molecule, which is also referred to as the Purcell effect [193]. On the other hand, when the interaction term, g, is large enough, then coherent and fast oscillatory exchange of energy can occur between light and matter, through the rapid exchange of virtual photons. The molecule can indeed absorb and emit a virtual photon that remains trapped within the cavity, so that it can be re-absorbed by the same or another molecule. If the rate of energy exchange exceeds the rate of any dissipation (e.g., cavity-photon leakage, non-radiative relaxation) or decoherence (e.g., molecular dephasing) processes, then the so-called *strong-coupling regime* arises between matter and the

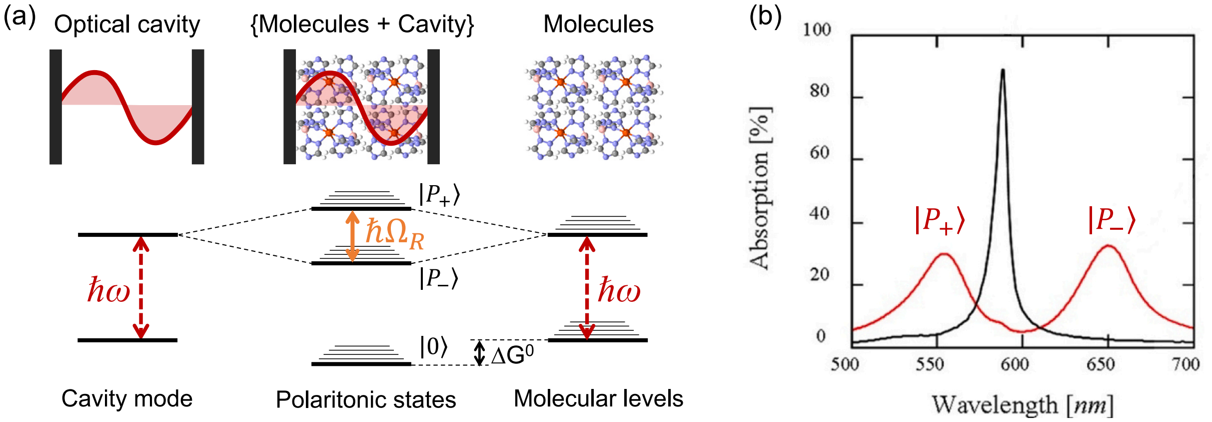

Fig. 22. (a) Simplified energy landscape of a {molecules + cavity} system in the strong-coupling regime. The resonance between the molecular excitation (electronic or vibrational) and the cavity mode of energy $\hbar\omega$ leads to the formation of two hybrid light-matter (polaritonic) states, $|P_+\rangle$ and $|P_-\rangle$, separated by the so-called Rabi splitting energy $\hbar\Omega_R$. Interestingly, the absolute energy of the ground-state level of the coupled system may also be modified (ΔG^0) due to strong coupling. (b) Experimental ground-state absorption spectrum of cyanine dye molecules before (*black curve*) and after (*red curve*) undergoing strong light-matter coupling with a cavity mode. Adapted with permission from Ref. [194]. (For interpretation of the references to color in this figure legend, the reader is referred to the web version of this article.)

surrounding electromagnetic field [194–200]. In this regime, new hybrid light-matter eigenstates (with both molecular and photonic characteristics) – known as polaritons – are formed, with an energy separation called Rabi splitting ($\hbar\Omega_R$), which is proportional to the coupling strength (see Fig. 22a). In the quantum electrodynamics picture, the uncoupled system formed by a molecule and a cavity can exist in two quantum states: $|e\rangle_{mol}|0\rangle_{cav}$, where the molecule is in the excited state with 0 photon in the cavity, and $|g\rangle_{mol}|1\rangle_{cav}$, where the molecule is in the ground state with 1 (virtual) photon in the cavity. Exactly like two atomic orbitals can hybridize to form new (molecular) orbitals (with different energies and shapes than the component atomic orbitals), the states $|e\rangle_{mol}|0\rangle_{cav}$ and $|g\rangle_{mol}|1\rangle_{cav}$ can mix under the effect of the light-matter interaction term to form new hybrid states, $|P_+\rangle$ and $|P_-\rangle$, which correspond to the eigenstates of the coupled system {molecules + cavity}. These so-called polaritonic states can thus be written as a quantum superposition of their excitonic (molecular) and photonic components [192]:

$$|P_+\rangle = \frac{1}{\sqrt{2}}\left(|e\rangle_{mol}|0\rangle_{cav} + |g\rangle_{mol}|1\rangle_{cav}\right) \tag{31}$$

$$|P_-\rangle = \frac{1}{\sqrt{2}}\left(|e\rangle_{mol}|0\rangle_{cav} - |g\rangle_{mol}|1\rangle_{cav}\right) \tag{32}$$

Consequently, the coupled system {molecules + cavity} must be considered as a single entity with new energy levels, and exhibiting unique physicochemical properties.

An intriguing feature is that this light-matter hybridization occurs even in the absence of real photons inside the cavity, since the coupling can arise from the vacuum fluctuations, i.e., the finite zero-point energy of the quantized electromagnetic field within the cavity [198]. In other words, the coupling is mediated by the exchange of virtual photons (which arise from the vacuum fluctuations in the electromagnetic field) and does not require real photons (light) to be applied on the cavity. The vacuum Rabi splitting energy between the polaritonic states for a single molecule in strong light-matter interaction with a cavity mode is given by [194]:

$$\hbar\Omega_R^{(1)} = 2\sqrt{g^2 - \frac{1}{4}(\Gamma_{cav} - \Gamma_{ex})^2} \tag{33}$$

where Γ_{cav} and Γ_{ex} are the resonance linewidths of the cavity mode and the molecular excitation, respectively. The associated Rabi frequency, Ω_R, is a measure of the energy exchange rate between the molecule and the cavity, i.e., a measure of the coupling strength.

Another fascinating aspect of strong coupling is its collective nature when a large number N of molecules are coupled to the same cavity mode. In fact, molecules in high concentration within a cavity can couple collectively to an effective mode of the electromagnetic field, meaning that all these molecules – even if they are far apart – can exchange energy coherently (via emission/re-absorption of virtual photons) with the same optical mode [192]. Such an in-phase behavior of all coupled molecules gives rise to the formation of a collective dipole, which leads to an enhancement of the vacuum Rabi splitting, $\hbar\Omega_R^{(N)}$, such as:

$$\hbar\Omega_R^{(N)} = \sqrt{N} \times \hbar\Omega_R^{(1)} \tag{34}$$

where $\hbar\Omega_R^{(1)}$ is the single-molecule Rabi splitting as given in Eq. (33). From a spectroscopic point of view, the strong-coupling regime is said to be achieved when the splitting energy between the two polaritonic states is larger than the spectral linewidths of both the cavity mode and the molecular excitation, i.e., $\hbar\Omega_R^{(N)} > \Gamma_{\text{cav}}, \Gamma_{\text{ex}}$ (Fig. 22b) [201]. This condition indicates that the energy exchange (emission/re-absorption) rate between the cavity and the molecules is faster than the loss rates, which can result from both the finite lifetime of photons inside the cavity (given by Γ_{cav}) and/or the finite lifetime of the molecular exciton (given by Γ_{ex}).

Two decades ago, studies on light-matter interactions and their implications using optical cavity fields were primarily conducted by physicists, with a major focus on inorganic materials (such as inorganic quantum wells) that required cryogenic temperatures and the fabrication of high-quality optical cavities [202,203]. Over the past decade, however, this topic has gradually expanded into the fields of molecular chemistry and materials science. Organic molecular systems, in particular, have garnered significant interest because exceptionally large vacuum Rabi splitting energies (of up to ≈ 1 eV) [204–206] can be achieved at room temperature, even in highly lossy, metal mirror-based optical cavities. This arises due to the large transition dipole moments and oscillator strengths of excitons (with relatively narrow allowed energy bands) in organic molecular materials, as well as the high densities at which molecules can be integrated within the cavities.

As such, the field of ‘polaritonic chemistry’, which focuses on the study of organic molecular systems under the regime of strong light-matter coupling, has gained significant attention in both experimental and theoretical research over the last decade [194–200]. In particular, this field has emerged in recent years as a powerful means to modify the chemical and physical properties of molecules incorporated into purposefully designed optical cavities, through the formation of polaritons. Indeed, as strong coupling to electronic excitations directly alters the excited-state potential energy surface of molecules (due to the large excited-state splitting), substantial effects on the photochemistry and photophysics of coupled photochromic molecules and organic polymers/dyes have been reported [207–210], thus providing a means to manipulate the photoreaction and relaxation pathways in the coupled molecules. More interestingly, not only is the energy of the excited states modified by the formation of polaritonic states, but many theoretical studies [211,212] have pointed out that the energy of the molecular electronic ground state might also be altered due to strong coupling, especially when the perturbation of the excited states is sufficiently large – i.e., when the Rabi splitting becomes a sizeable fraction ($> 10\,\%$) of the unperturbed material excitation energy. In this so-called ultrastrong-coupling regime, theoretical considerations indeed predict that, in addition to the large excited-state splitting, a lowering of the ground-state energy level must occur as the latter also acquires a non-zero photonic contribution [211,212], which suggests appealing perspectives for manipulating the thermodynamic (ground-state) properties of molecules placed inside an optical cavity.

In the case of molecular SCO materials, achieving a strong-coupling regime from ligand-field *d–d* absorption bands seems unfeasible due to their weak absorption coefficient (i.e., weak transition dipole moment). However, in a recent study [213], the first observation of strong light-matter coupling involving SCO molecules was reported by coupling a cavity mode to the intense charge-transfer bands of two isomeric complexes, [Fe(HB(1,2,4-triazol-1-yl)$_3$)$_2$] and [Fe(HB(1,2,3-triazol-1-yl)$_3$)$_2$], in the UV spectral range. The coupling was achieved by fabricating optical resonators consisting of a bilayer of Al (16 nm) and SCO complexes (~150 nm), deposited by thermal evaporation onto a prism (Fig. 23a). The choice of metal layer (Al instead of Ag) and the thickness of the SCO film allowed an optical mode of the structure to be resonant with the intense UV charge-transfer absorption bands of the SCO compounds in their LS state. In the angular dispersion map of the cavity (Fig. 23b), distinct splittings of the photon mode can be observed at wavelengths corresponding to the main absorption bands of the SCO molecules in the LS state. These splittings are the signature of strong light-matter coupling between the molecules and the optical modes. Due to the strong absorption and high concentration of SCO molecules within the cavity, Rabi splittings of up to 550 meV were reported, even suggesting the achievement of an ultrastrong-coupling regime. As the UV absorption bands are completely bleached when heating the SCO film above the spin-transition temperature, unsplit resonance peaks are recovered in the HS state (Fig. 23b). Thus, owing to the SCO phenomenon, reversible switching between (ultra)strong- and weak-coupling regimes can be achieved within a single cavity, as demonstrated by the temperature-dependent evolution of the measured Rabi splittings (Fig. 23c).

This study [213] demonstrates that SCO molecules can be successfully used as active elements to control (e.g., activate/deactivate) the strong-coupling regime in photonic nanostructures and, in turn, tune cavity resonances. As such, this phenomenon opens up considerable

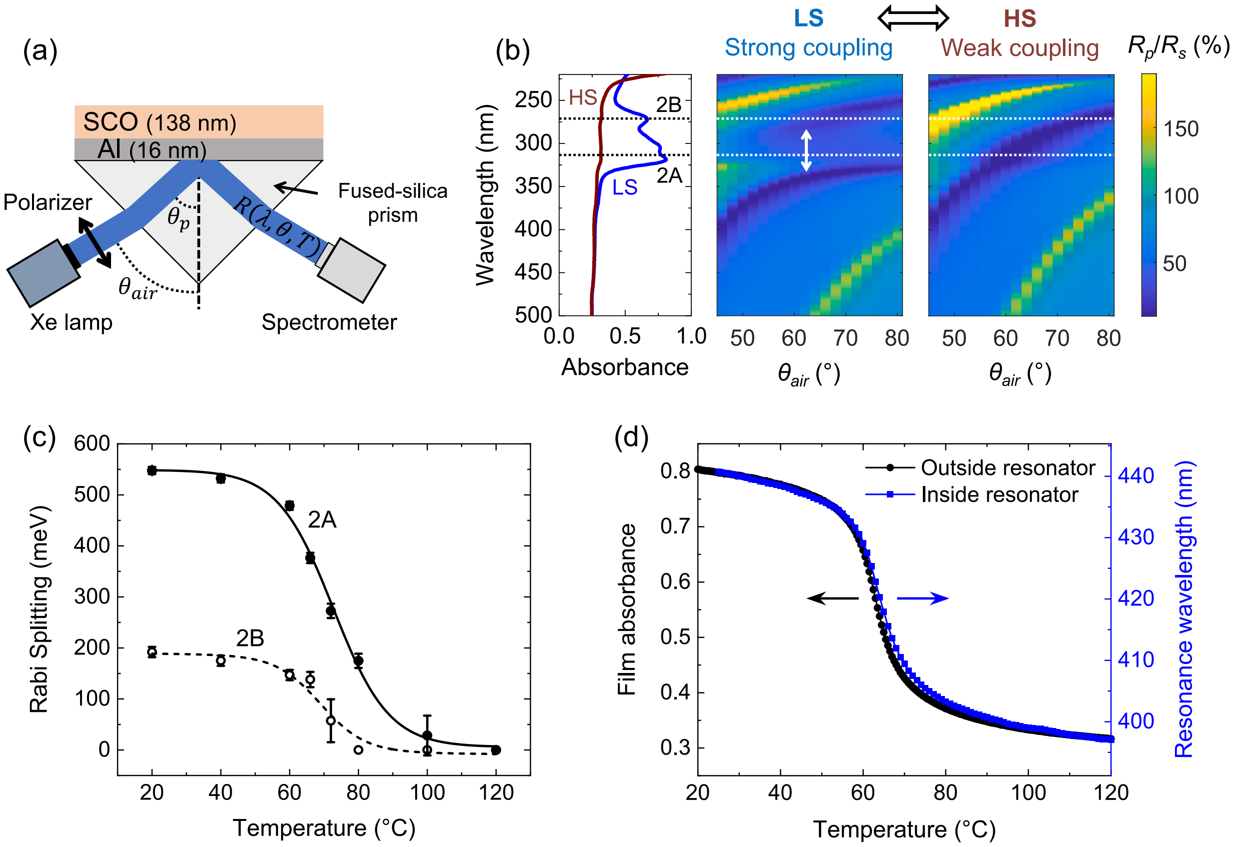

Fig. 23. (a) Schematic of a SCO-based optical resonator, consisting of an Al (16 nm)/[Fe(HB(1,2,4-triazol-1-yl)$_3$)$_2$] (138 nm) bilayer deposited on a prism, used to achieve the strong light-matter coupling regime. (b) Angular dispersion map of the resonator obtained by acquiring angle-dependent reflectance spectra in the LS and HS states. The panel on the left shows absorbance spectra of the SCO film in both spin states. The absorption maxima of the SCO complex in the LS state are indicated by horizontal dashed lines. A clear splitting (indicated by a white arrow) of the optical mode is observed in the LS state, revealing the strong-coupling regime, while unsplit resonances are evidenced in the HS state. (c) Temperature evolution of the Rabi splitting energies associated with the two main absorption bands, denoted as 2A and 2B. (d) Comparison of the thermal spin-transition curves of a bare SCO film of [Fe(HB(1,2,4-triazol-1-yl)$_3$)$_2$] and the coupled film within the optical resonator. This comparison shows that the SCO properties (i.e., abruptness and switching temperature) of the film strongly coupled to the optical resonator remain essentially unchanged within experimental uncertainties. Adapted with permission from Ref. [213].

prospects for modulating light propagation in original switchable polaritonic nanocavities – instead of using conventional refractive index switching. On the other way around, another appealing perspective is to use the strong-coupling phenomenon to tune the properties of coupled SCO molecules inside the resonant cavities. First, since light-matter coupling directly affects the excited-state energy levels of molecules, substantial effects are expected on the photoswitching pathway involved in the light-induced spin transition upon photoexcitation into the coupled polaritonic states. This could potentially lead to a modification of the overall dynamics and/or the quantum efficiency of the photoinduced transition, as has been observed, for example, in certain photochromic molecules [207,210]. Second, if the coupling strength is sufficiently large, a lowering of the molecular ground-state energy level might also be achieved, opening the fascinating perspective of modifying the thermodynamic equilibrium between the LS and HS states of the coupled molecules. However, the magnitude of this effect remains highly controversial in the field of polaritonic chemistry, even at the theoretical level [200], especially in the case where the coupling collectively involves a large number of molecules [214,215].

In this context, the fact that SCO molecules can be coupled to a cavity mode, a priori, in only one spin state provides a means to finely investigate the potential effect of strong coupling on the ground-state energy level, i.e., on the spin-state equilibrium temperature. Our first investigation [213] shows that the SCO properties of the film coupled to the optical resonator remain essentially unaltered (Fig. 23d), indicating that no noticeable change in the energy gap between the LS and HS ground states could be detected under the experimental conditions used. Very recently, a more detailed investigation [216], carried out in Fabry-Pérot cavities, revealed that the shift in the spin-transition temperature due to strong coupling remains below 1 °C (i.e., within experimental uncertainties), confirming that the ground state remains largely unaffected by the formation of polaritons. Undeniably, further work is needed to shed light on this phenomenon, which will require the study of ultrasmall systems composed of a reduced number of molecules in the ultrastrong-coupling regime, within nanocavities with more tightly confined electromagnetic fields.

Interestingly, light-matter hybridization is not limited to electronic excitations, as molecular vibrations can also strongly couple to IR electromagnetic fields in microcavities, leading to the formation of vibrational or phonon polaritons [199,217]. This so-called vibrational strong coupling (VSC) offers exciting possibilities for the selective modification of chemical bond energies, which has been recently much investigated for tuning the ground-state chemical reactivity of molecules [218–223]. In the specific case of SCO complexes, VSC offers appealing perspectives for tuning the spin-transition properties in optical cavities, since the SCO phenomenon is intrinsically linked to intramolecular vibrations. In addition, it is worth mentioning that other effects, which differ from strong coupling, might also be observed in optical cavities. Notably, theoretical calculations have suggested that the interaction between the permanent dipole moment ($\boldsymbol{\mu}$) of SCO molecules and the confined electromagnetic field in plasmonic nanocavities could lead to a significant shift in the spin-state equilibrium temperature – provided that $\boldsymbol{\mu}$ is aligned with the cavity mode polarization and undergoes a sizeable change during the spin transition [224]. For this reason, particular attention should be paid to SCO compounds that exhibit a large (change of) dipole moment, which might typically be observed in low-symmetry complexes formed from hetero-ligands.

Overall, investigating the physicochemical behavior of molecules within optical cavities, whose properties can be tuned through light-matter interactions with confined electromagnetic fields, opens the door to a variety of fascinating perspectives that have yet to be discovered [200]. To this end, the precise mechanisms underpinning polaritonic chemistry still need to be elucidated.

5. Light-induced spin crossover: Towards all-optical devices?

All the SCO-based optical switches investigated so far (see section 4.1 and 4.3) are based on thermal (or photothermal) addressing, which is an intrinsically slow process, unsuitable for many technological applications. In this context, an important asset of SCO materials is the possibility to trigger the molecular spin-state switching by ultrashort light irradiation. This property opens up appealing prospects for the development of ultrafast, all-optical SCO-based switching devices.

The process by which the molecular spin state can be switched from the LS to the HS state upon photoexcitation into specific metal-centered absorption bands (either ligand-field or charge-transfer bands) of the LS species is referred to as the LIESST effect [25,26]. Importantly, this photoswitching process is known to be ultrafast (sub-picosecond) at the molecular scale. The mechanistic details of this molecular photoconversion process have been largely discussed, particularly in the case of Fe^{2+} SCO complexes, in terms of the energy diagram shown in Fig. 24, which displays the potential energy surface of the well-known Fe^{2+} SCO complex $[Fe(ptz)_6](BF_4)_2$, as determined through detailed optical absorption spectroscopy (Fig. 2a) [27,28,42,225,226]. As a direct transition from the LS singlet state ($S = 0$) to the HS quintet state ($S = 2$) is forbidden by selection rules, the photoswitching pathway is known to involve intermediate, short-lived excited states. In brief, upon irradiation of the sample at specific wavelengths in the UV–vis ranges, transient excited states of the molecules, $^1T_{1g}$ (~540 nm) or ^1MLCT (~305 nm),

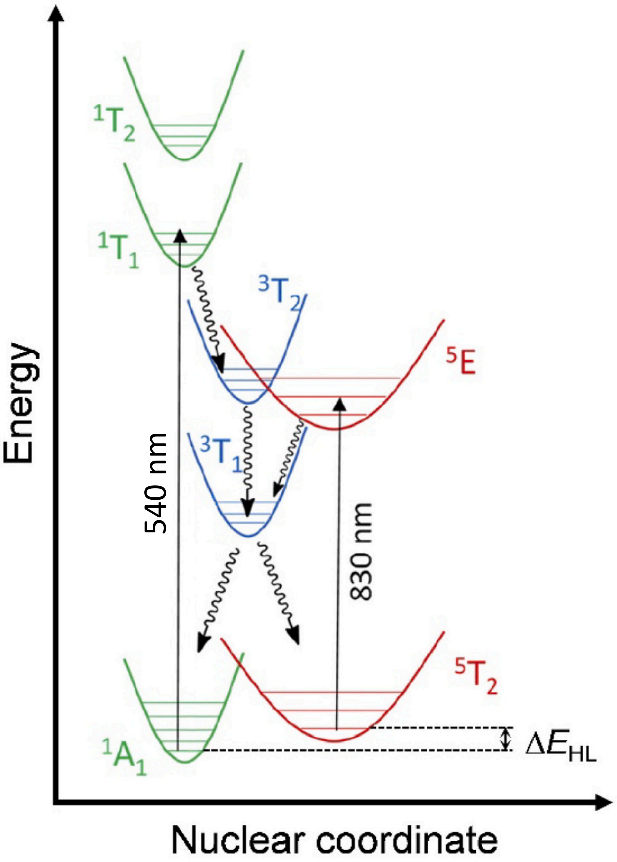

Fig. 24. Energy diagram depicting the electronic potential wells of the Fe^{2+} SCO complex $[Fe(ptz)_6](BF_4)_2$ and their spectroscopic assignment, showing the LIESST and reverse-LIESST pathways. The vertical straight lines represent light-induced transitions (via Franck-Condon processes, i.e., unchanged nuclear coordinates), whereas the wavy lines represent non-radiative relaxations. Adapted with permission from Ref. [226].

are populated from the $^1A_{1g}$ LS ground state via a Franck-Condon process (vertical transition on the potential energy surface). Subsequently, the excited molecules relax non-radiatively to the $^5T_{2g}$ HS state through cascading intersystem crossings, involving successive changes in spin multiplicity ($\Delta S = 1$) via the population of intermediate short-lived state (s), as illustrated in Fig. 24 [226,227]. Importantly, as revealed by femtosecond time-resolved experiments, the photoexcited molecules reach the HS potential well within 100–200 fs [228–231]. In addition, precise spectroscopic measurements have shown that the quantum efficiency for the light-induced population of the metastable HS state is close to unity, meaning that each absorbed photon virtually results in one photoswitched molecule [42,232].

As highlighted by several theoretical studies [233,234], the exceptional speed and efficiency of the LIESST effect may be attributed to the instantaneous activation of key molecular vibrations influencing the main reaction coordinate (metal-ligand stretching modes) after photoexcitation – favoring ultrafast cascading intersystem crossings – followed by their fast damping, which enables efficient structural trapping of the photoinduced HS molecules. As shown in Fig. 24, it is important to note that the reverse process (known as the reverse-LIESST effect), which consists in pumping the system back to the LS state, is also possible by selectively irradiating into the $^5T_{2g} \rightarrow {}^5E_g$ ligand-field band of HS molecules (at ~830 nm in the case of $[Fe(ptz)_6](BF_4)_2$) [235]. However, this molecular photoconversion process exhibits slower dynamics compared to the LIESST effect [236] and a low quantum efficiency of only about 10 %.

In solid-state SCO systems, however, it appears that only a small fraction (typically a few percent) of molecules can be photoconverted into the HS state on an ultrashort timescale [46,93,237–240]; otherwise, degradation of the compound is generally observed upon increasing pulse energies. This aspect constitutes a severe limitation in the perspective of achieving large optical modulation depths in SCO-based devices driven by short light pulses. However, on longer timescales, time-resolved X-ray diffraction and optical spectroscopy studies [89,91,241,242] have revealed a significant amplification of the fraction of switched HS molecules, due to the subsequent activation of so-called thermo-elastic effects within the material, driven by the active role of the crystal lattice (see Fig. 25). In short, following the ultrafast molecular photoswitching process, significant photoinduced stresses (internal pressure) are generated within the material, due to the structural rearrangement (volume swelling) of the photoswitched molecules and the transient increase in lattice temperature. Indeed, since the photon energy of the excitation laser (~1–4 eV) is much larger than the zero-point energy difference between the LS and HS states (~50–200 meV), a large part of the excitation energy is transferred to the lattice and converted to heat [243,244]. In response to these photoinduced stresses, mechanical equilibrium with the external environment is restored through the propagation of coherent acoustic phonons, resulting in a global structural expansion of the crystal lattice on the so-called acoustic timescale, which is determined by the typical length scale of the sample and the speed of sound in the SCO material [89,91,241,242].

Subsequently, this new lattice conformation (with expanded volume and elevated temperature) induces, in turn, a second increase of the fraction of HS molecules, which is usually referred to as a “thermo-elastic” switching step [46,238,239,245]. This delayed molecular conversion corresponds to a stage of thermodynamic equilibration between the spin state of molecules and the lattice conformation. Importantly, this thermo-elastic switching step can involve the conversion of a significant fraction of molecules (typically between 10 % and 30 % [46,237,238], though it can be as high as 50 %, as demonstrated in a recent study [240], depending on experimental conditions), which is obviously an important asset for achieving large modulation amplitudes in optical switching devices. However, despite the fact that the temperature rise and lattice expansion are completed within ~100 ps in SCO nanomaterials, recent experimental studies [46,238,239] have revealed that this thermo-elastic conversion step actually takes place on a timescale of tens of nanoseconds (see Fig. 25), thus demonstrating a clear temporal separation between electronic and lattice degrees of freedom [239]. This significant delay was imputed to the intramolecular energy barrier between the LS and HS states, which requires an Arrhenius-like activation process to switch the molecules into the HS state. Therefore, these recent studies suggest that this intramolecular energy barrier inherently acts as a dynamical bottleneck in the phototransformation process of SCO compounds. However, it was also demonstrated in another recent work [246] that very high excitation of SCO nanoparticles can mitigate the effects of such local energy barriers, allowing the system to relax directly towards the HS state without incubation time.

Importantly, the LS-to-HS photoswitching process is said to be *volatile* since the final HS state has a finite lifetime after photoexcitation. The recovery to the LS ground state appears to be primarily governed by the rate of heat dissipation to the external medium. Notably, the back-relaxation dynamics critically depends on the size of the sample and the nature of its external environment. For Fe^{2+} SCO nanometric thin films (on glass substrates), the relaxation back to the LS state was typically found to occur within 0.1–1 μs at room temperature (see Fig. 25) [46,239]. These results demonstrate the feasibility of modulating the molecular spin state under ambient conditions in the 1–10 MHz frequency range using ultrashort laser excitations. Although promising, these initial results are still insufficient, as the

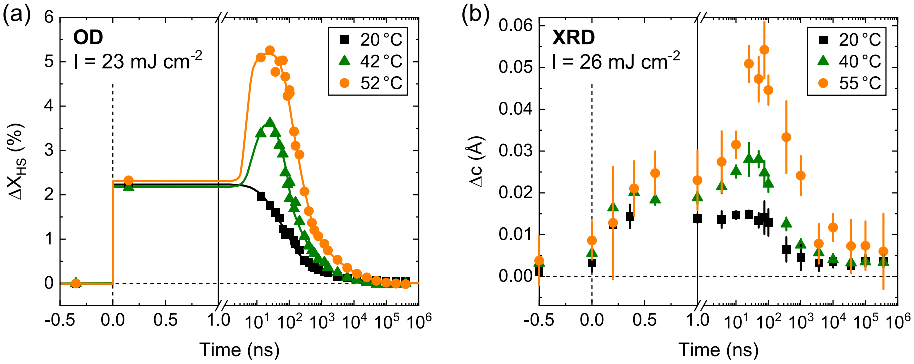

Fig. 25. (a) Time evolution of the fraction of photoswitched HS molecules, ΔX_{HS}, in a 175-nm-thick film of $[Fe(HB(1,2,4\text{-triazol-1-yl})_3)_2]$, recorded at selected temperatures by transient absorption spectroscopy, following a laser pulse with an energy density of 23 mJ cm^{-2}. After the ultrafast (sub-picosecond) photoswitching process, a second thermo-elastic conversion step is observed on a timescale of tens of nanoseconds, before relaxation back to the LS state takes place (~1 μs). (b) Dynamics of the lattice volume change in the same film, quantified by the time evolution of the orthorhombic *c*-lattice parameter variation, Δc, recorded by X-ray diffraction. The lattice volume expansion occurs within 100 ps (acoustic timescale) following the laser pulse. As with ΔX_{HS}, a delayed increase in the lattice volume is observed on a timescale of tens of nanoseconds in response to the thermo-elastic switching step. Reproduced with permission from Ref. [239].

technologically relevant frequencies for optical switches are rather in the GHz range.

To increase the accessible modulation frequency of SCO devices, it appears essential to fine-tune the photoresponse of the crystal lattice of SCO nanomaterials by engineering the thermomechanical coupling with the external environment (e.g., by incorporating the SCO elements in close contact with a heat sink to accelerate heat dissipation and back relaxation). At the same time, it is also crucial to tune the intramolecular energy barrier of SCO molecules, which governs the LS-to-HS thermoelastic amplification step. From this perspective, an important bottleneck arises in Fe^{2+} SCO compounds, as their local energy barrier is relatively high due to the large variation in metal-ligand bond lengths ($\Delta r_{HL} \approx 0.2$ Å) between the LS and HS states. This critical limitation highlights the potential advantages of using SCO compounds with different *d*-electron configurations, such as Fe^{3+} ($3d^5$) and Co^{2+} ($3d^7$) complexes, which exhibit lower intramolecular energy barriers due to smaller metal-ligand bond length changes ($\Delta r_{HL} \approx 0.15$ and 0.10 Å, respectively), enabling sub-nanosecond switching times at room temperature [28]. However, for these complexes, the price to pay will certainly be a reduced refractive index change in the visible spectrum, owing to their relatively small volume changes during the SCO transition.

Finally, beyond the switching speed of the molecular spin state, another fundamental (yet still unexplored) question concerns the dynamics of refractive index changes in SCO nano-objects following the molecular photoconversion. Since the main contribution to refractive index modulation in the visible spectral range arises from the volume change of the crystal lattice, it can be expected from the available experimental data that the photoinduced change in n may typically occur on the acoustic timescale, i.e., within 10–100 ps in nanometer-sized objects. Interestingly, in other spectral ranges (e.g., THz), where refractive index modulation is predominantly governed by variations in the ionic polarizability of molecules between the LS and HS states (see section 2.3), this change in n could potentially be faster, occurring on the timescale of intramolecular reorganization processes (picoseconds). Obviously, these rough estimates still need experimental validation. From this point of view, it is worth noting that polaritonic SCO-based devices (section 4.3), as well as any other device relying on optical modulation induced by electronic transition changes, hold significant promise for achieving all-optical, high-speed switching applications.

Interestingly, a *non-volatile* photoswitching response – a property essential for many optical memory applications – can also be achieved when photoexciting within the hysteretic region of certain SCO solids. Such a hysteresis loop arises in some SCO materials due to the formation of a free energy barrier between the LS and HS phases, which stems from the existence of strong, long-range elastic interactions between the metal centers. In such cases, the photoexcited state can be efficiently trapped – with virtually infinite lifetime – due to the high free energy barrier between the two phases [35]. Such a non-volatile photoconversion process within the thermal hysteresis loop of SCO materials, driven by pulsed-laser excitation, has been experimentally reported in numerous studies [79,86,243,244,246–253]. However, the mechanisms and underlying dynamics of this laser-induced switching – particularly how the hysteretic free energy barrier is overcome to efficiently trap the HS state – remain a subject of ongoing debate [35]. While a typical activation time on the millisecond timescale was reported in bulk crystals of the compound $[Fe(HB(1,2,4\text{-triazol-1-yl})_3)_2]$ [86], the LS-to-HS transition was found to be completed within ~50 ps in nanometer-sized (10–15 nm) particles of $[Fe(Htrz)_2(trz)](BF_4)$ dispersed in solution (Fig. 26) [246]. Although the mechanism at the origin of this fast switching process remains to be investigated, these recently obtained results [246] support the feasibility of all-optical memory applications based on SCO nanomaterials with ultrafast (tens of picoseconds) encoding times.

Finally, beyond the LIESST effect, it should also be noted that other *non-volatile* photoswitching processes of the molecular spin state rather involve photochemical reactions of the coordinating ligands. Specifically, for some SCO complexes, the selective photoexcitation of ligand-centered absorption bands can induce conformational changes in the ligands (such as photoisomerization or cyclization) or in guest molecules [255], which lead to modifications in the ligand field strength and, consequently, a change of the molecular spin state. This is the case of the so-called ligand-driven light-induced spin change (LD-LISC) effect, whereby the ligand is photochemically transformed from one isomeric

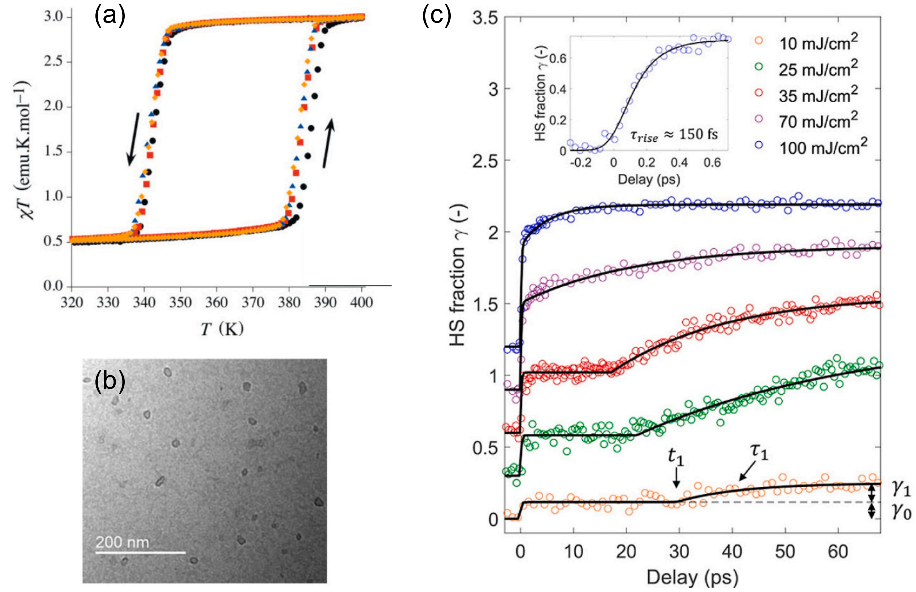

Fig. 26. (a) Typical thermal hysteresis loop between the LS and HS states in 10–15 nm sized nanoparticles of the SCO compound $[Fe(Htrz)_2(trz)](BF_4)$. Reproduced with permission from Ref. [254]. (b) Transmission electron microscopy (TEM) image of the $[Fe(Htrz)_2(trz)](BF_4)$ nanoparticles used for the time-resolved photoswitching study. (c) Time evolution of the fraction of photoswitched HS molecules, extracted from X-ray emission spectroscopy (XES), following a 266-nm laser pulse at different excitation fluences. The inset shows the sub-picosecond timescale evolution of the HS fraction, collected for an excitation fluence of 100 mJ cm^{-2}. Reproduced with permission from Ref. [246].

form to another [256–258]. Similarly, another effect, known as light-driven coordination-induced spin-state switching (LD-CISSS), involves a change in the coordination number of the metal ion as a result of the photoisomerization reaction, affecting the ligand field and orbital occupancy [259–262]. Interestingly, such ligand-driven photoswitching processes, which can operate in a reversible way at room temperature, are non-volatile, since the transformation occurs between two stable, long-lived isomeric forms. However, due to the significant structural rearrangement during photoisomerization, these photoconversion processes are difficult to achieve in bulk solids and often require relatively long irradiation times [263,264], which greatly limits their suitability for practical applications.

6. Summary and outlook

Undeniably, molecular spin-crossover complexes possess a unique combination of optical properties. They display large differences in extinction coefficient and refractive index between their low-spin and high-spin forms, which arise from both electronic and structural factors. The most characteristic structural difference is the increase in mass density in the LS state, which gives rise to a broadband enhancement of the refractive index in the vis-NIR spectral ranges, seemingly violating the Kramers-Kronig relations between n and k. Although thermochromism and thermoreflectance are ubiquitous in SCO materials, somewhat surprisingly, the literature with properly assigned optical spectra and refractive index data remains meager and mostly limited to ferrous (Fe^{2+}) triazole and tetrazole complexes. Researchers should therefore be advised to systematically report these figures for novel SCO compounds, in particular for non-ferrous systems. Theoretical studies going beyond crystal field theory – for example, using density functional theory – could also provide valuable insights in this context. Further fundamental work is also needed to elucidate the link between the electronic spin state of molecules and the refractive index of the material, which is a particularly intriguing question at ultrafast timescales wherein the electronic and lattice degrees of freedom are known to evolve separately in time [239].

Somewhat less recognized is the fact that the spin-state dependence of the complex refractive index is not limited to the optical frequencies, but also embraces the terahertz and microwave domains, with significant application potential in a variety of technologies (e.g., terahertz switches, reconfigurable antennas). However, to enable progress towards these applications, the fundamental physics governing the changes in dielectric properties in these spectral ranges still needs to be uncovered.

The first and currently most important practical use of optical property changes at the SCO is the detection of the phenomenon itself. Indeed, optical detection provides an extremely cost-effective and versatile means of monitoring the SCO phenomenon both in bulk and, importantly, in nanoscale materials, including single nanoparticles. Optical detection can not only afford high sensitivity, but also high spatial (< µm) and temporal (< ps) resolutions, which allowed to obtain precious insights into the spatiotemporal dynamics of the spin-state switching process. Besides fundamental research, optical detection has also been employed to develop sensors for monitoring changes in the environment (e.g., temperature, pressure, and concentration of chemical species). Among these, importantly, surface temperature microsensors based on SCO coatings, as well as thermochromic SCO inks, have reached such an advanced stage of development that they can be considered commercially relevant. As such, they provide a first tangible proof of the technological applicability of SCO materials. This can encourage engineers to go beyond proofs of concept and construct fully-fledged devices in order to explore the full technological potential of SCO-based sensors.

The ability to incorporate high-quality SCO materials with precise geometries into photonic and nanophotonic devices has also enabled the development of new concepts such as tuneability, adaptability, and reconfigurability, which can be advantageously used in a variety of active photonic applications. Specifically, the unique optical properties of SCO materials provide scope to realize integrated active photonic devices with a broad optical bandwidth and low transmission losses in the visible spectral range, wherein other families of phase-change materials usually underperform. However, further improvements in optical contrast are needed to reduce footprint and energy consumption. This will require smart designs that account for the most desirable modal interaction between the SCO material and the optical fields within the photonic device.

Regardless of the intended optical applications (sensing or switching), a great advantage of molecular SCO materials is their intrinsic versatility, which implies different spin-state switching behaviors and various optical properties, depending on the specific transition metal ion complex selected from the vast and flexible family of SCO compounds. The response can be either transient or non-volatile (memory effect), depending on the compound used and the experimental conditions, which allows for a wide range of functionalities. This versatility and multifunctionality mean that SCO systems provide an excellent platform for synergistically combining optical properties with other physicochemical phenomena, such as sorption, chirality, catalytic activity, ferroelectricity, mechanical damping, and so forth [265,266]. Working towards the design of such diversely functionalized SCO materials is expected to gain increasing importance in the near future. In this context, it is worth noting the strong conceptual connections between SCO molecules and other types of molecular magnetic switches, such as valence tautomeric complexes, bistable organic radicals, Jahn-Teller switches, Prussian blue analogues, and other cyanometalate assemblies [267,268]. As such, the application ideas, design concepts, and challenges discussed in the present review on SCO materials can, in many cases, be directly extended to these systems. These various compounds can thus broaden the possibilities for synthetic chemists in designing switchable optical properties and may also give rise to functionalities that are not conceivable using SCO complexes.

Undeniably, the SCO field has also reached a certain degree of maturity due to significant progress made over the last decade in the fabrication and design of SCO nanomaterials (thin films, nanopatterns, gratings, etc.), with notable gains in terms of cycling endurance, switching speed, and long-term stability, which may qualify them as viable technological solutions for demanding photonic applications. The switching speed can be further improved in modulation-type devices using Fe^{3+} and Co^{2+} complexes, which exhibit smaller intramolecular energy barriers in comparison with Fe^{2+} compounds. As for non-volatile switch-type devices, there is a real promise for achieving ultrafast switching through size reduction effects, which could lead to a drastic decrease in the hysteretic free energy barrier between the HS and LS phases, enabling fast (picosecond) activation times.

Finally, recent studies have demonstrated (ultra)strong light-matter coupling between molecular electronic excitations and electromagnetic modes for SCO molecules embedded within resonant optical cavities. In this strong interaction regime, light and matter couple to form new hybrid polaritonic states, which modify the molecular energy landscape. This raises a fascinating question: Can one tune the (switching) properties of SCO molecules through light-matter hybridization?

Declaration of competing interest

The authors declare that they have no known competing financial interests or personal relationships that could have appeared to influence the work reported in this paper.

Acknowledgement

K.R. acknowledges financial support from the Agence Nationale de la Recherche (project SCOPOL, ANR-22-CE09-0019).

Appendix A. Supplementary data

Supplementary data to this article can be found online at https://doi.org/10.1016/j.ccr.2025.216628.

Data availability

Data will be made available on request.

References

[1] P. Gütlich, A. Hauser, H. Spiering, Thermal and optical switching of iron(II) complexes, Angew. Chem. Int. Ed. Eng. 33 (1994) 2024–2054, https://doi.org/10.1002/anie.199420241.

[2] P. Gütlich, Y. Garcia, H.A. Goodwin, Spin crossover phenomena in Fe(II) complexes, Chem. Soc. Rev. 29 (2000) 419–427, https://doi.org/10.1039/B003504L.

[3] L. Cambi, L. Szegö, Über die magnetische Susceptibilität der komplexen Verbindungen, Ber. Dtsch. Chem. Ges. A/B 64 (1931) 2591–2598, https://doi.org/10.1002/cber.19310641002.

[4] L. Cambi, L. Szegö, Über die magnetische Susceptibilität der komplexen Verbindungen (II. Mitteil.), Ber. Dtsch. Chem. Ges. A/B 66 (1933) 656–661, https://doi.org/10.1002/cber.19330660508.

[5] A. Bousseksou, G. Molnár, L. Salmon, W. Nicolazzi, Molecular spin crossover phenomenon: recent achievements and prospects, Chem. Soc. Rev. 40 (2011) 3313–3335, https://doi.org/10.1039/C1CS15042A.

[6] P. Gütlich, Spin crossover – quo Vadis? Eur. J. Inorg. Chem. 2013 (2013) 581–591, https://doi.org/10.1002/ejic.201300092.

[7] K. Senthil Kumar, M. Ruben, Emerging trends in spin crossover (SCO) based functional materials and devices, Coord. Chem. Rev. 346 (2017) 176–205, https://doi.org/10.1016/j.ccr.2017.03.024.

[8] G. Molnár, S. Rat, L. Salmon, W. Nicolazzi, A. Bousseksou, Spin crossover nanomaterials: from fundamental concepts to devices, Adv. Mater. 30 (2018) 1703862, https://doi.org/10.1002/adma.201703862.

[9] A. Bousseksou (Ed.), Spin Crossover Phenomenon, C. R. Chim. 21, 2018, pp. 1055–1300.

[10] P. Gütlich, H.A. Goodwin, Spin Crossover in Transition Metal Compounds I-III, Springer, Berlin, Heidelberg, 2004.

[11] M.A. Halcrow, Spin-Crossover Materials: Properties and Applications, John Wiley & Sons, Ltd., Leeds, 2013.

[12] A. Hauser, Ligand field theoretical considerations, in: P. Gütlich, H.A. Goodwin (Eds.), Spin Crossover in Transition Metal Compounds I, Springer, Berlin, Heidelberg, 2004, pp. 49–58, https://doi.org/10.1007/b13528.

[13] M. Sorai, S. Seki, Phonon coupled cooperative low-spin $^1A_1$ high-spin $^5T_2$ transition in [Fe(phen)$_2$(NCS)$_2$] and [Fe(phen)$_2$(NCSe)$_2$] crystals, J. Phys. Chem. Solids 35 (1974) 555–570, https://doi.org/10.1016/S0022-3697(74)80010-7.

[14] S.K. Kulshreshtha, R.M. Iyer, E. König, G. Ritter, The nature of spin-state transitions in Fe(II) complexes, Chem. Phys. Lett. 110 (1984) 201–204, https://doi.org/10.1016/0009-2614(84)80175-X.

[15] E. König, G. Ritter, S.K. Kulshreshtha, The nature of spin-state transitions in solid complexes of iron(II) and the interpretation of some associated phenomena, Chem. Rev. 85 (1985) 219–234, https://doi.org/10.1021/cr00067a003.

[16] M. Sorai, Heat capacity studies of spin crossover systems, in: P. Gütlich, H. A. Goodwin (Eds.), Spin Crossover in Transition Metal Compounds III, Springer, Berlin, Heidelberg, 2004, pp. 153–170, https://doi.org/10.1007/b95426.

[17] P. Guionneau, M. Marchivie, G. Bravic, J.-F. Létard, D. Chasseau, Structural aspects of spin crossover. Example of the [Fe^{II}L$_n$(NCS)$_2$] complexes, in: P. Gütlich, H.A. Goodwin (Eds.), Spin Crossover in Transition Metal Compounds II, Springer, Berlin, Heidelberg, 2004, pp. 97–128, https://doi.org/10.1007/b95414.

[18] P. Gütlich, H.A. Goodwin, D.N. Hendrickson, Bond-stretch isomers: fact not fiction, Angew. Chem. Int. Ed. Eng. 33 (1994) 425–427, https://doi.org/10.1002/anie.199404251.

[19] P. Guionneau, Crystallography and spin-crossover. a view of breathing materials, Dalton Trans. 43 (2013) 382–393, https://doi.org/10.1039/C3DT52520A.

[20] E. Collet, P. Guionneau, Structural analysis of spin-crossover materials: from molecules to materials, C. R. Chim. 21 (2018) 1133–1151, https://doi.org/10.1016/j.crci.2018.02.003.

[21] S. Pillet, Spin-crossover materials: getting the most from X-ray crystallography, J. Appl. Phys. 129 (2021) 181101, https://doi.org/10.1063/5.0047681.

[22] M. Grzywa, R. Röß-Ohlenroth, C. Muschielok, H. Oberhofer, A. Błachowski, J. Żukrowski, D. Vieweg, H.-A.K. von Nidda, D. Volkmer, Cooperative large-hysteresis spin-crossover transition in the iron(II) triazolate [Fe(ta)$_2$] metal–organic framework, Inorg. Chem. 59 (2020) 10501–10511, https://doi.org/10.1021/acs.inorgchem.0c00814.

[23] W. Nicolazzi, A. Bousseksou, Thermodynamical aspects of the spin crossover phenomenon, C. R. Chim. 21 (2018) 1060–1074, https://doi.org/10.1016/j.crci.2018.10.003.

[24] A. Hauser, C. Enachescu, M.L. Daku, A. Vargas, N. Amstutz, Low-temperature lifetimes of metastable high-spin states in spin-crossover and in low-spin iron(II) compounds: the rule and exceptions to the rule, Coord. Chem. Rev. 250 (2006) 1642–1652, https://doi.org/10.1016/j.ccr.2005.12.006.

[25] J.J. McGravey, I. Lawthers, Photochemically-induced perturbation of the ^{1}A $\rightleftharpoons$ ^{5}T equilibrium in Fe^{II} complexes by pulsed laser irradiation in the metal-to-ligand charge-transfer absorption band, J. Chem. Soc. Chem. Commun. (1982) 906–907, https://doi.org/10.1039/C39820000906.

[26] S. Decurtins, P. Gütlich, C.P. Köhler, H. Spiering, A. Hauser, Light-induced excited spin state trapping in a transition-metal complex: the hexa-1-propyltetrazole-iron (II) tetrafluoroborate spin-crossover system, Chem. Phys. Lett. 105 (1984) 1–4, https://doi.org/10.1016/0009-2614(84)80403-0.

[27] A. Hauser, Cooperative effects on the HS→LS relaxation in the [Fe(ptz)$_6$](BF$_4$)$_2$ spin-crossover system, Chem. Phys. Lett. 192 (1992) 65–70, https://doi.org/10.1016/0009-2614(92)85429-E.

[28] A. Hauser, Light-induced spin crossover and the high-spin→low-spin relaxation, in: P. Gütlich, H.A. Goodwin (Eds.), Spin Crossover in Transition Metal Compounds II, Springer, Berlin, Heidelberg, 2004, pp. 155–198, https://doi.org/10.1007/b95416.

[29] G. Molnár, M. Mikolasek, K. Ridier, A. Fahs, W. Nicolazzi, A. Bousseksou, Molecular spin crossover materials: review of the lattice dynamical properties, Ann. Phys. (Berlin) 531 (2019) 1900076, https://doi.org/10.1002/andp.201900076.

[30] H. Spiering, Elastic interaction in spin-crossover compounds, in: P. Gütlich, H. A. Goodwin (Eds.), Spin Crossover in Transition Metal Compounds III, Springer, Berlin, Heidelberg, 2004, pp. 171–195, https://doi.org/10.1007/b95427.

[31] H. Spiering, E. Meissner, H. Köppen, E.W. Müller, P. Gütlich, The effect of the lattice expansion on high spin $\rightleftharpoons$ low spin transitions, Chem. Phys. 68 (1982) 65–71, https://doi.org/10.1016/0301-0104(82)85080-5.

[32] N. Willenbacher, H. Spiering, The elastic interaction of high-spin and low-spin complex molecules in spin-crossover compounds, J. Phys. C Solid State Phys. 21 (1988) 1423, https://doi.org/10.1088/0022-3719/21/8/017.

[33] C. Enachescu, W. Nicolazzi, Elastic models, lattice dynamics and finite size effects in molecular spin crossover systems, C. R. Chim. 21 (2018) 1179–1195, https://doi.org/10.1016/j.crci.2018.02.004.

[34] M. Mikolasek, G. Félix, W. Nicolazzi, G. Molnár, L. Salmon, A. Bousseksou, Finite size effects in molecular spin crossover materials, New J. Chem. 38 (2014) 1834–1839, https://doi.org/10.1039/C3NJ01268A.

[35] K. Ridier, G. Molnár, L. Salmon, W. Nicolazzi, A. Bousseksou, Hysteresis, nucleation and growth phenomena in spin-crossover solids, Solid State Sci. 74 (2017) A1–A22, https://doi.org/10.1016/j.solidstatesciences.2017.10.014.

[36] Y. Zhang, R. Torres-Cavanillas, X. Yan, Y. Zeng, M. Jiang, M. Clemente-León, E. Coronado, S. Shi, Spin crossover iron complexes with spin transition near room temperature based on nitrogen ligands containing aromatic rings: from molecular design to functional devices, Chem. Soc. Rev. 53 (2024) 8764–8789, https://doi.org/10.1039/D3CS00688C.

[37] N.A.A.M. Amin, S.M. Said, M.F.M. Salleh, A.M. Afifi, N.M.J.N. Ibrahim, M.M.I. M. Hasnan, M. Tahir, N.Z.I. Hashim, Review of Fe-based spin crossover metal complexes in multiscale device architectures, Inorg. Chim. Acta 544 (2023) 121168, https://doi.org/10.1016/j.ica.2022.121168.

[38] O. Kahn, J. Kröber, C. Jay, Spin transition molecular materials for displays and data recording, Adv. Mater. 4 (1992) 718–728, https://doi.org/10.1002/adma.19920041103.

[39] O. Kahn, C.J. Martinez, Spin-transition polymers: from molecular materials toward memory devices, Science 279 (1998) 44–48, https://doi.org/10.1126/science.279.5347.44.

[40] R.L. de Kronig, On the theory of dispersion of X-rays, J. Opt. Soc. Am. 12 (1926) 547–557, https://doi.org/10.1364/JOSA.12.000547.

[41] A. Hauser, Intersystem crossing in Fe(II) coordination compounds, Coord. Chem. Rev. 111 (1991) 275–290, https://doi.org/10.1016/0010-8545(91)84034-3.

[42] A. Hauser, Intersystem crossing in the [Fe(ptz)$_6$](BF$_4$)$_2$ spin crossover system (ptz=1-propyltetrazole), J. Chem. Phys. 94 (1991) 2741–2748, https://doi.org/10.1063/1.459851.

[43] Y. Tanabe, S. Sugano, On the absorption spectra of complex ions. I, J. Phys. Soc. Jpn. 9 (1954) 753–766, https://doi.org/10.1143/JPSJ.9.753.

[44] Y. Tanabe, S. Sugano, On the absorption spectra of complex ions II, J. Phys. Soc. Jpn. 9 (1954) 766–779, https://doi.org/10.1143/JPSJ.9.766.

[45] J. Ribas Gispert, Coordination Chemistry, Wiley-VCH, Weinheim, 2008.

[46] K. Ridier, A.-C. Bas, V. Shalabaeva, W. Nicolazzi, L. Salmon, G. Molnár, A. Bousseksou, M. Lorenc, R. Bertoni, E. Collet, H. Cailleau, Finite size effects on the switching dynamics of spin-crossover thin films photoexcited by a femtosecond laser pulse, Adv. Mater. 31 (2019) 1901361, https://doi.org/10.1002/adma.201901361.

[47] T. Delgado, A. Tissot, C. Besnard, L. Guénée, P. Pattison, A. Hauser, Structural investigation of the high spin→low spin relaxation dynamics of the porous coordination network [Fe(pz)Pt(CN)$_4$]·2.6 H$_2$O, Chem. Eur. J. 21 (2015) 3664–3670, https://doi.org/10.1002/chem.201405405.

[48] A. Hauser, Four-wave-mixing in the Fe(II) spin-crossover system [Zn$_{1-x}$Fe$_x$(ptz)$_6$](BF$_4$)$_2$ (ptz = 1-propyltetrazole), Chem. Phys. Lett. 202 (1993) 173–178, https://doi.org/10.1016/0009-2614(93)85368-X.

[49] E.D. Loutete-Dangui, F. Varret, E. Codjovi, P.R. Dahoo, H. Tokoro, S. Ohkoshi, C. Eypert, J.F. Létard, J.M. Coanga, K. Boukheddaden, Thermal spin transition in [Fe(NH$_2$-trz)$_3$]Br$_2$ investigated by spectroscopic ellipsometry, Phys. Rev. B 75 (2007) 184425, https://doi.org/10.1103/PhysRevB.75.184425.

[50] G. Félix, K. Abdul-Kader, T. Mahfoud, I.A. Gural'skiy, W. Nicolazzi, L. Salmon, G. Molnár, A. Bousseksou, Surface plasmons reveal spin crossover in nanometric layers, J. Am. Chem. Soc. 133 (2011) 15342–15345, https://doi.org/10.1021/ja207196b.

[51] A. Akou, I.A. Gural'skiy, L. Salmon, C. Bartual-Murgui, C. Thibault, C. Vieu, G. Molnár, A. Bousseksou, Soft lithographic patterning of spin crossover complexes. Part 2: stimuli-responsive diffraction grating properties, J. Mater. Chem. 22 (2012) 3752–3757, https://doi.org/10.1039/C2JM15663F.

[52] A. Akou, C. Bartual-Murgui, K. Abdul-Kader, M. Lopes, G. Molnár, C. Thibault, C. Vieu, L. Salmon, A. Bousseksou, Photonic gratings of the metal–organic framework $\{Fe(bpac)[Pt(CN)_4]\}$ with synergetic spin transition and host–guest properties, Dalton Trans. 42 (2013) 16021–16028, https://doi.org/10.1039/C3DT51687C.

[53] A. Iazzolino, G. Galle, J. Degert, J.F. Létard, E. Freysz, Impact of the spin state switching on the dielectric constant of iron (II) spin crossover nanoparticles, Chem. Phys. Lett. 641 (2015) 14–19, https://doi.org/10.1016/j.cplett.2015.10.038.

[54] M. Palluel, N.M. Tran, N. Daro, S. Buffière, S. Mornet, E. Freysz, G. Chastanet, The interplay between surface plasmon resonance and switching properties in gold@spin crossover nanocomposites, Adv. Funct. Mater. 30 (2020) 2000447, https://doi.org/10.1002/adfm.202000447.

[55] Y. Zhang, K. Ridier, V. Shalabaeva, I. Séguy, S. Pelloquin, H. Camon, S. Calvez, L. Routaboul, L. Salmon, G. Molnár, A. Bousseksou, A molecular spin-crossover film allows for wavelength tuning of the resonance of a Fabry–Perot cavity, J. Mater. Chem. C 8 (2020) 8007–8011, https://doi.org/10.1039/D0TC02094J.

[56] L. Zhang, J.A. Capo Chichi, S. Calvez, Y. Zhang, L. Salmon, G. Molnár, K. Ridier, A. Bousseksou, Thermo-optical switches based on spin-crossover molecules with wideband transparency, Adv. Opt. Mater. 12 (2024) 2303252, https://doi.org/10.1002/adom.202303252.

[57] J.H. Gladstone, T.P. Dale, XIV., Researches on the refraction, dispersion, and sensitiveness of liquids, Philos. Trans. R. Soc. 153 (1863) 317–343, https://doi.org/10.1098/rstl.1863.0014.

[58] P. Mounaix, N. Lascoux, J. Degert, E. Freysz, A. Kobayashi, N. Daro, J.-F. Létard, Dielectric characterization of $[Fe(NH_2{-}trz)_3]Br_2{\bullet}H_2O$ thermal spin crossover compound by terahertz time domain spectroscopy, Appl. Phys. Lett. 87 (2005) 244103, https://doi.org/10.1063/1.2143123.

[59] P. Mounaix, E. Freysz, J. Degert, N. Daro, J.-F. Létard, P. Kužel, V. Vigneras, L. Oyenhart, One-dimensional tunable photonic crystals with spin crossover material for the terahertz range, Appl. Phys. Lett. 89 (2006) 174105, https://doi.org/10.1063/1.2369535.

[60] B. Viquerat, J. Degert, M. Tondusson, E. Freysz, C. Mauriac, J.F. Létard, Time-domain terahertz spectroscopy of spin state transition in $[Fe(NH_2\text{-}trz)_3]^{2+}$ spin crossover compounds, Appl. Phys. Lett. 99 (2011) 061908, https://doi.org/10.1063/1.3624600.

[61] O.I. Kucheriv, V.V. Oliynyk, V.V. Zagorodnii, V.L. Launets, I.A. Gural'skiy, Spin-crossover materials towards microwave radiation switches, Sci. Rep. 6 (2016) 38334, https://doi.org/10.1038/srep38334.

[62] O.I. Kucheriv, V.V. Oliynyk, V.V. Zagorodnii, V.L. Launets, O.V. Penkivska, I. O. Fritsky, I.A. Gural'skiy, Tunable microwave absorption of switchable complexes operating near room temperature, RSC Adv. 10 (2020) 21621–21628, https://doi.org/10.1039/D0RA02236E.

[63] M. Nakano, G. Matsubayashi, T. Matsuo, Dielectric behavior of manganese(III) spin-crossover complex [Mn(taa)], Phys. Rev. B 66 (2002) 212412, https://doi.org/10.1103/PhysRevB.66.212412.

[64] A. Bousseksou, G. Molnár, P. Demont, J. Menegotto, Observation of a thermal hysteresis loop in the dielectric constant of spin crossover complexes: towards molecular memory devices, J. Mater. Chem. 13 (2003) 2069–2071, https://doi.org/10.1039/B306638J.

[65] S. Bonhommeau, T. Guillon, L.M. Lawson Daku, P. Demont, J. Sanchez Costa, J.-F. Létard, G. Molnár, A. Bousseksou, Photoswitching of the dielectric constant of the spin-crossover complex $[Fe(L)(CN)_2]{\cdot}H_2O$, Angew. Chem. Int. Ed. 45 (2006) 1625–1629, https://doi.org/10.1002/anie.200503252.

[66] T. Guillon, S. Bonhommeau, J.S. Costa, A. Zwick, J.-F. Létard, P. Demont, G. Molnár, A. Bousseksou, On the dielectric properties of the spin crossover complex $[Fe(bpp)_2]\ [BF_4]_2$, Phys. Status Solidi A 203 (2006) 2974–2980, https://doi.org/10.1002/pssa.200567103.

[67] C. Lefter, I.A. Gural'skiy, H. Peng, G. Molnár, L. Salmon, A. Rotaru, A. Bousseksou, P. Demont, Dielectric and charge transport properties of the spin crossover complex $[Fe(Htrz)_2(trz)](BF_4)$, Phys. Status Solidi (RRL) 8 (2014) 191–193, https://doi.org/10.1002/pssr.201308256.

[68] J.-L. Wang, Q. Liu, Y.-S. Meng, H. Zheng, H.-L. Zhu, Q. Shi, T. Liu, Synergic on/off photoswitching spin state and magnetic coupling between spin crossover centers, Inorg. Chem. 56 (2017) 10674–10680, https://doi.org/10.1021/acs.inorgchem.7b01633.

[69] H. Zheng, Y.-S. Meng, G.-L. Zhou, C.-Y. Duan, O. Sato, S. Hayami, Y. Luo, T. Liu, Simultaneous modulation of magnetic and dielectric transition via spin-crossover-tuned spin arrangement and charge distribution, Angew. Chem. Int. Ed. 57 (2018) 8468–8472, https://doi.org/10.1002/ange.201802774.

[70] I. Soroceanu, A. Graur, E. Coca, L. Salmon, G. Molnar, P. Demont, A. Bousseksou, A. Rotaru, Broad-band dielectric spectroscopy reveals peak values of conductivity and permittivity switching upon spin crossover, J. Phys. Chem. Lett. 10 (2019) 7391–7396, https://doi.org/10.1021/acs.jpclett.9b02678.

[71] Y.-R. Qiu, L. Cui, P.-Y. Cai, F. Yu, M. Kurmoo, C.F. Leong, D.M. D'Alessandro, J.-L. Zuo, Enhanced dielectricity coupled to spin-crossover in a one-dimensional polymer iron(II) incorporating tetrathiafulvalene, Chem. Sci. 11 (2020) 6229–6235, https://doi.org/10.1039/D0SC02388D.

[72] N.-T. Yao, L. Zhao, H.-Y. Sun, C. Yi, Y.-H. Guan, Y.-M. Li, H. Oshio, Y.-S. Meng, T. Liu, Simultaneous photo-induced magnetic and dielectric switching in an iron (II)-based spin-crossover Hofmann-type metal-organic framework, Angew. Chem. Int. Ed. 61 (2022) e202208208, https://doi.org/10.1002/anie.202208208.

[73] X.-R. Wu, S.-Q. Wu, Z.-K. Liu, M.-X. Chen, J. Tao, O. Sato, H.-Z. Kou, Integrating spin-dependent emission and dielectric switching in Fe^{II} catenated metal-organic frameworks, Nat. Commun. 15 (2024) 3961, https://doi.org/10.1038/s41467-024-48425-8.

[74] W. Cochran, The Dynamics of Atoms in Crystals, Edward Arnold Publishers Ltd., London, 1973.

[75] C. Lefter, V. Davesne, L. Salmon, G. Molnár, P. Demont, A. Rotaru, A. Bousseksou, Charge transport and electrical properties of spin crossover materials: towards nanoelectronic and spintronic devices, Magnetochemistry 2 (2016) 18, https://doi.org/10.3390/magnetochemistry2010018.

[76] A. Rotaru, I.A. Gural'skiy, G. Molnár, L. Salmon, P. Demont, A. Bousseksou, Spin state dependence of electrical conductivity of spin crossover materials, Chem. Commun. 48 (2012) 4163–4165, https://doi.org/10.1039/C2CC30528C.

[77] A. Goujon, F. Varret, K. Boukheddaden, C. Chong, J. Jeftić, Y. Garcia, A.D. Naik, J.C. Ameline, E. Collet, An optical microscope study of photo-switching and relaxation in single crystals of the spin transition solid $[Fe(ptz)_6](BF_4)_2$, with image processing, Inorg. Chim. Acta 361 (2008) 4055–4064, https://doi.org/10.1016/j.ica.2008.03.094.

[78] C. Chong, H. Mishra, K. Boukheddaden, S. Denise, G. Bouchez, E. Collet, J.-C. Ameline, A.D. Naik, Y. Garcia, F. Varret, Electronic and structural aspects of spin transitions observed by optical microscopy. The case of $[Fe(ptz)_6](BF_4)_2$, J. Phys. Chem. B 114 (2010) 1975–1984, https://doi.org/10.1021/jp910999y.

[79] S. Bedoui, M. Lopes, W. Nicolazzi, S. Bonnet, S. Zheng, G. Molnár, A. Bousseksou, Triggering a phase transition by a spatially localized laser pulse: role of strain, Phys. Rev. Lett. 109 (2012) 135702, https://doi.org/10.1103/PhysRevLett.109.135702.

[80] S. Bedoui, M. Lopes, S. Zheng, S. Bonnet, G. Molnár, A. Bousseksou, Laser-induced artificial defects (LIADs): towards the control of the spatiotemporal dynamics in spin transition materials, Adv. Mater. 24 (2012) 2475–2478, https://doi.org/10.1002/adma.201200386.

[81] A. Slimani, F. Varret, K. Boukheddaden, D. Garrot, H. Oubouchou, S. Kaizaki, Velocity of the high-spin low-spin interface inside the thermal hysteresis loop of a spin-crossover crystal, via photothermal control of the interface motion, Phys. Rev. Lett. 110 (2013) 087208, https://doi.org/10.1103/PhysRevLett.110.087208.

[82] M. Sy, D. Garrot, A. Slimani, M. Páez-Espejo, F. Varret, K. Boukheddaden, Reversible control by light of the high-spin low-spin elastic interface inside the bistable region of a robust spin-transition single crystal, Angew. Chem. Int. Ed. 55 (2016) 1755–1759, https://doi.org/10.1002/anie.201509294.

[83] K. Ridier, S. Rat, H.J. Shepherd, L. Salmon, W. Nicolazzi, G. Molnár, A. Bousseksou, Spatiotemporal dynamics of the spin transition in $[Fe(HB(tz)_3)_2]$ single crystals, Phys. Rev. B 96 (2017) 134106, https://doi.org/10.1103/PhysRevB.96.134106.

[84] H. Fourati, E. Milin, A. Slimani, G. Chastanet, Y. Abid, S. Triki, K. Boukheddaden, Interplay between a crystal's shape and spatiotemporal dynamics in a spin transition material, Phys. Chem. Chem. Phys. 20 (2018) 10142–10154, https://doi.org/10.1039/C8CP00868J.

[85] H. Fourati, K. Boukheddaden, Experimental evidence for the elastic long-range character of the spin crossover transition in cooperative single crystals, Phys. Rev. B 101 (2020) 224101, https://doi.org/10.1103/PhysRevB.101.224101.

[86] K. Ridier, W. Nicolazzi, L. Salmon, G. Molnár, A. Bousseksou, Sequential activation of molecular and macroscopic spin-state switching within the hysteretic region following pulsed light excitation, Adv. Mater. 34 (2022) 2105468, https://doi.org/10.1002/adma.202105468.

[87] W. Gawelda, A. Cannizzo, V.-T. Pham, F. van Mourik, C. Bressler, M. Chergui, Ultrafast nonadiabatic dynamics of $[Fe^{II}(bpy)_3]^{2+}$ in solution, J. Am. Chem. Soc. 129 (2007) 8199–8206, https://doi.org/10.1021/ja070454x.

[88] A.L. Smeigh, M. Creelman, R.A. Mathies, J.K. McCusker, Femtosecond time-resolved optical and Raman spectroscopy of photoinduced spin crossover: temporal resolution of low-to-high spin optical switching, J. Am. Chem. Soc. 130 (2008) 14105–14107, https://doi.org/10.1021/ja805949s.

[89] M. Lorenc, J. Hébert, N. Moisan, E. Trzop, M. Servol, M. Buron-Le Cointe, H. Cailleau, M.L. Boillot, E. Pontecorvo, M. Wulff, S. Koshihara, E. Collet, Successive dynamical steps of photoinduced switching of a molecular Fe(III) spin-crossover material by time-resolved X-ray diffraction, Phys. Rev. Lett. 103 (2009) 028301, https://doi.org/10.1103/PhysRevLett.103.028301.

[90] A. Cannizzo, C.J. Milne, C. Consani, W. Gawelda, Ch. Bressler, F. van Mourik, M. Chergui, Light-induced spin crossover in Fe(II)-based complexes: the full photocycle unraveled by ultrafast optical and X-ray spectroscopies, Coord. Chem. Rev. 254 (2010) 2677–2686, https://doi.org/10.1016/j.ccr.2009.12.007.

[91] M. Lorenc, Ch. Balde, W. Kaszub, A. Tissot, N. Moisan, M. Servol, M. Buron-Le Cointe, H. Cailleau, P. Chasle, P. Czarnecki, M.L. Boillot, E. Collet, Cascading photoinduced, elastic, and thermal switching of spin states triggered by a femtosecond laser pulse in an Fe(III) molecular crystal, Phys. Rev. B 85 (2012) 054302, https://doi.org/10.1103/PhysRevB.85.054302.

[92] R. Bertoni, M. Lorenc, A. Tissot, M. Servol, M.-L. Boillot, E. Collet, Femtosecond spin-state photoswitching of molecular nanocrystals evidenced by optical spectroscopy, Angew. Chem. Int. Ed. 51 (2012) 7485–7489, https://doi.org/10.1002/anie.201202215.

[93] R. Bertoni, M. Lorenc, T. Graber, R. Henning, K. Moffat, J.-F. Létard, E. Collet, Cooperative elastic switching vs. laser heating in $[Fe(phen)_2(NCS)_2]$ spin-crossover crystals excited by a laser pulse, CrystEngComm 18 (2016) 7269–7275, https://doi.org/10.1039/C6CE00659K.

[94] S. Shi, G. Schmerber, J. Arabski, J.-B. Beaufrand, D.J. Kim, S. Boukari, M. Bowen, N.T. Kemp, N. Viart, G. Rogez, E. Beaurepaire, H. Aubriet, J. Petersen, C. Becker, D. Ruch, Study of molecular spin-crossover complex $Fe(phen)_2(NCS)_2$ thin films, Appl. Phys. Lett. 95 (2009) 043303, https://doi.org/10.1063/1.3192355.

[95] H. Naggert, A. Bannwarth, S. Chemnitz, T. von Hofe, E. Quandt, F. Tuczek, First observation of light-induced spin change in vacuum deposited thin films of iron

spin crossover complexes, Dalton Trans. 40 (2011) 6364–6366, https://doi.org/10.1039/C1DT10651A.

[96] V. Shalabaeva, M. Mikolasek, M.D. Manrique-Juarez, A.-C. Bas, S. Rat, L. Salmon, W. Nicolazzi, G. Molnár, A. Bousseksou, Unprecedented size effect on the phase stability of molecular thin films displaying a spin transition, J. Phys. Chem. C 121 (2017) 25617–25621, https://doi.org/10.1021/acs.jpcc.7b10124.

[97] O.Ye. Horniichuk, K. Ridier, L. Zhang, Y. Zhang, G. Molnár, L. Salmon, A. Bousseksou, High-sensitivity microthermometry method based on vacuum-deposited thin films exhibiting gradual spin crossover above room temperature, ACS Appl. Mater. Interfaces 14 (2022) 52140–52148, https://doi.org/10.1021/acsami.2c13834.

[98] O. Iasco, M.-L. Boillot, A. Bellec, R. Guillot, E. Rivière, S. Mazerat, S. Nowak, D. Morineau, A. Brosseau, F. Miserque, V. Repain, T. Mallah, The disentangling of hysteretic spin transition, polymorphism and metastability in bistable thin films formed by sublimation of bis(scorpionate) Fe(II) molecules, J. Mater. Chem. C 5 (2017) 11067–11075, https://doi.org/10.1039/C7TC03276E.

[99] H.J. Shepherd, C.M. Quintero, G. Molnár, L. Salmon, A. Bousseksou, Luminescent spin-crossover materials, in: M.A. Halcrow (Ed.), Spin-Crossover Materials: Properties and Applications, John Wiley & Sons, Ltd., Leeds, 2013, pp. 347–373, https://doi.org/10.1002/9781118519301.ch13.

[100] M.K. Javed, A. Sulaiman, M. Yamashita, Z.-Y. Li, Shedding light on bifunctional luminescent spin crossover materials, Coord. Chem. Rev. 467 (2022) 214625, https://doi.org/10.1016/j.ccr.2022.214625.

[101] L. Salmon, G. Molnár, D. Zitouni, C. Quintero, C. Bergaud, J.-C. Micheau, A. Bousseksou, A novel approach for fluorescent thermometry and thermal imaging purposes using spin crossover nanoparticles, J. Mater. Chem. 20 (2010) 5499–5503, https://doi.org/10.1039/C0JM00631A.

[102] S. Titos-Padilla, J.M. Herrera, X.-W. Chen, J.J. Delgado, E. Colacio, Bifunctional hybrid SiO_2 nanoparticles showing synergy between core spin crossover and shell luminescence properties, Angew. Chem. Int. Ed. 50 (2011) 3290–3293, https://doi.org/10.1002/anie.201007847.

[103] I. Suleimanov, O. Kraieva, J.S. Costa, I.O. Fritsky, G. Molnár, L. Salmon, A. Bousseksou, Electronic communication between fluorescent pyrene excimers and spin crossover complexes in nanocomposite particles, J. Mater. Chem. C 3 (2015) 5026–5032, https://doi.org/10.1039/C5TC00667H.

[104] C.M. Quintero, I.A. Gural'skiy, L. Salmon, G. Molnár, C. Bergaud, A. Bousseksou, Soft lithographic patterning of spin crossover complexes. Part 1: fluorescent detection of the spin transition in single nano-objects, J. Mater. Chem. 22 (2012) 3745–3751, https://doi.org/10.1039/C2JM15662H.

[105] C.-F. Wang, R.-F. Li, X.-Y. Chen, R.-J. Wei, L.-S. Zheng, J. Tao, Synergetic spin crossover and fluorescence in one-dimensional hybrid complexes, Angew. Chem. Int. Ed. 54 (2015) 1574–1577, https://doi.org/10.1002/anie.201410454.

[106] Y. Jiao, J. Zhu, Y. Guo, W. He, Z. Guo, Synergetic effect between spin crossover and luminescence in the $[Fe(bpp)_2][BF_4]_2$ (bpp = 2,6-bis(pyrazol-1-yl)pyridine) complex, J. Mater. Chem. C 5 (2017) 5214–5222, https://doi.org/10.1039/C7TC00507E.

[107] C. Lochenie, K. Schötz, F. Panzer, H. Kurz, B. Maier, F. Puchtler, S. Agarwal, A. Köhler, B. Weber, Spin-crossover iron(II) coordination polymer with fluorescent properties: correlation between emission properties and spin state, J. Am. Chem. Soc. 140 (2018) 700–709, https://doi.org/10.1021/jacs.7b10571.

[108] R. Turo-Cortés, M. Meneses-Sánchez, T. Delgado, C. Bartual-Murgui, M.C. Muñoz, J.A. Real, Coexistence of luminescence and spin-crossover in 2D iron(II) Hofmann clathrates modulated through guest encapsulation, J. Mater. Chem. C 10 (2022) 10686–10698, https://doi.org/10.1039/D2TC02039D.

[109] J.-L. Wang, Q. Liu, Y.-S. Meng, X. Liu, H. Zheng, Q. Shi, C.-Y. Duan, T. Liu, Fluorescence modulation via photoinduced spin crossover switched energy transfer from fluorophores to Fe^{II} ions, Chem. Sci. 9 (2018) 2892–2897, https://doi.org/10.1039/C7SC05221A.

[110] F.-F. Yan, W.-J. Jiang, N.-T. Yao, P.-D. Mao, L. Zhao, H.-Y. Sun, Y.-S. Meng, T. Liu, Manipulating fluorescence by photo-switched spin-state conversions in an iron (II)-based SCO-MOF, Chem. Sci. 14 (2023) 6936–6942, https://doi.org/10.1039/D3SC01217D.

[111] N. Deorukhkar, C. Egger, A. Rosspeintner, C. Piguet, Unravelling kinetics of intramolecular $Nd^{III} \rightarrow Fe^{II}$ energy transfer in spin crossover single molecules: dotting the i's and crossing the t's, J. Am. Chem. Soc. 146 (2024) 19386–19396, https://doi.org/10.1021/jacs.4c05546.

[112] Y. Garcia, F. Robert, A.D. Naik, G. Zhou, B. Tinant, K. Robeyns, S. Michotte, L. Piraux, Spin transition charted in a fluorophore-tagged thermochromic dinuclear iron(II) complex, J. Am. Chem. Soc. 133 (2011) 15850–15853, https://doi.org/10.1021/ja205974q.

[113] T. Lathion, A. Fürstenberg, C. Besnard, A. Hauser, A. Bousseksou, C. Piguet, Monitoring Fe(II) spin-state equilibria via Eu(III) luminescence in molecular complexes: dream or reality? Inorg. Chem. 59 (2020) 1091–1103, https://doi.org/10.1021/acs.inorgchem.9b02713.

[114] K. Ridier, A.-C. Bas, Y. Zhang, L. Routaboul, L. Salmon, G. Molnár, C. Bergaud, A. Bousseksou, Unprecedented switching endurance affords for high-resolution surface temperature mapping using a spin-crossover film, Nat. Commun. 11 (2020) 3611, https://doi.org/10.1038/s41467-020-17362-7.

[115] K. Abdul-Kader, M. Lopes, C. Bartual-Murgui, O. Kraieva, E.M. Hernández, L. Salmon, W. Nicolazzi, F. Carcenac, C. Thibault, G. Molnár, A. Bousseksou, Synergistic switching of plasmonic resonances and molecular spin states, Nanoscale 5 (2013) 5288–5293, https://doi.org/10.1039/C3NR01337E.

[116] E. Kretschmann, H. Raether, Radiative decay of non radiative surface plasmons excited by light, Z. Naturforsch. A 23 (1968) 2135–2136, https://doi.org/10.1515/zna-1968-1247.

[117] I. Suleimanov, J.S. Costa, G. Molnár, L. Salmon, A. Bousseksou, The photo-thermal plasmonic effect in spin crossover@silica–gold nanocomposites, Chem. Commun. 50 (2014) 13015–13018, https://doi.org/10.1039/C4CC02652G.

[118] R. Sanchis-Gual, R. Torres-Cavanillas, M. Coronado-Puchau, M. Giménez-Marqués, E. Coronado, Plasmon-assisted spin transition in gold nanostar@spin crossover heterostructures, J. Mater. Chem. C 9 (2021) 10811–10818, https://doi.org/10.1039/D1TC01943K.

[119] Y. Hu, M. Picher, N.M. Tran, M. Palluel, L. Stoleriu, N. Daro, S. Mornet, C. Enachescu, E. Freysz, F. Banhart, G. Chastanet, Photo-thermal switching of individual plasmonically activated spin crossover nanoparticle imaged by ultrafast transmission electron microscopy, Adv. Mater. 33 (2021) 2105586, https://doi.org/10.1002/adma.202105586.

[120] C. Arnaud, T. Forestier, N. Daro, E. Freysz, J.-F. Létard, G. Pauliat, G. Roosen, Observation of an asymmetry in the thermal hysteresis loop at the scale of a single spin-crossover particle, Chem. Phys. Lett. 470 (2009) 131–135, https://doi.org/10.1016/j.cplett.2009.01.014.

[121] S. Liu, K. Zhou, T. Yuan, W. Lei, H.-Y. Chen, X. Wang, W. Wang, Imaging the thermal hysteresis of single spin-crossover nanoparticles, J. Am. Chem. Soc. 142 (2020) 15852–15859, https://doi.org/10.1021/jacs.0c05951.

[122] S. Liu, W. Wang, Optical imaging of the stochastic nucleation kinetics and intrinsic activation energy of single spin-crossover nanoparticles, Proc. Natl. Acad. Sci. USA 121 (2024) e2415379121, https://doi.org/10.1073/pnas.2415379121.

[123] J.C. Maxwell Garnett, XII., Colours in metal glasses and in metallic films, Philos. Trans. R. Soc. A 203 (1904) 385–420, https://doi.org/10.1098/rsta.1904.0024.

[124] V.A. Markel, Introduction to the Maxwell Garnett approximation: tutorial, J. Opt. Soc. Am. A 33 (2016) 1244–1256, https://doi.org/10.1364/JOSAA.33.001244.

[125] J.A. Wolny, V. Schünemann, Z. Németh, G. Vankó, Spectroscopic techniques to characterize the spin state: vibrational, optical, Mössbauer, NMR, and X-ray spectroscopy, C. R. Chim. 21 (2018) 1152–1169, https://doi.org/10.1016/j.crci.2018.10.001.

[126] G. Molnár, V. Niel, A.B. Gaspar, J.-A. Real, A. Zwick, A. Bousseksou, J. J. McGarvey, Vibrational spectroscopy of cyanide-bridged, iron(II) spin-crossover coordination polymers: estimation of vibrational contributions to the entropy change associated with the spin transition, J. Phys. Chem. B 106 (2002) 9701–9707, https://doi.org/10.1021/jp025678a.

[127] C. Bartual-Murgui, A. Cerf, C. Thibault, C. Vieu, L. Salmon, G. Molnár, A. Bousseksou, SERS-active substrates for investigating ultrathin spin-crossover films, Microelectron. Eng. 111 (2013) 365–368, https://doi.org/10.1016/j.mee.2013.02.102.

[128] M. Lopes, C.M. Quintero, E.M. Hernández, V. Velázquez, C. Bartual-Murgui, W. Nicolazzi, L. Salmon, G. Molnár, A. Bousseksou, Atomic force microscopy and near-field optical imaging of a spin transition, Nanoscale 5 (2013) 7762–7767, https://doi.org/10.1039/C3NR03030J.

[129] Y. Garcia, V. Ksenofontov, P. Gütlich, Spin transition molecular materials: new sensors, Hyperfine Interact. 139 (2002) 543–551, https://doi.org/10.1023/A:1021287115124.

[130] J. Linares, E. Codjovi, Y. Garcia, Pressure and temperature spin crossover sensors with optical detection, Sensors 12 (2012) 4479–4492, https://doi.org/10.3390/s120404479.

[131] M. Cavallini, M. Melucci, Organic materials for time–temperature integrator devices, ACS Appl. Mater. Interfaces 7 (2015) 16897–16906, https://doi.org/10.1021/acsami.5b03931.

[132] K. Boukheddaden, M.H. Ritti, G. Bouchez, M. Sy, M.M. Dîrtu, M. Parlier, J. Linares, Y. Garcia, Quantitative contact pressure sensor based on spin crossover mechanism for civil security applications, J. Phys. Chem. C 122 (2018) 7597–7604, https://doi.org/10.1021/acs.jpcc.8b00778.

[133] A. Lapresta-Fernández, M.P. Cuéllar, J.M. Herrera, A. Salinas-Castillo, M.C. del Pegalajar, S. Titos-Padilla, E. Colacio, L.F. Capitán-Vallvey, Particle tuning and modulation of the magnetic/colour synergy in Fe(II) spin crossover-polymer nanocomposites in a thermochromic sensor array, J. Mater. Chem. C 2 (2014) 7292–7303, https://doi.org/10.1039/C4TC00969J.

[134] A.D. Naik, K. Robeyns, C.F. Meunier, A.F. Léonard, A. Rotaru, B. Tinant, Y. Filinchuk, B.L. Su, Y. Garcia, Selective and reusable iron(II)-based molecular sensor for the vapor-phase detection of alcohols, Inorg. Chem. 53 (2014) 1263–1265, https://doi.org/10.1021/ic402816a.

[135] Y. Guo, S. Xue, M.M. Dîrtu, Y. Garcia, A versatile iron(II)-based colorimetric sensor for the vapor-phase detection of alcohols and toxic gases, J. Mater. Chem. C 6 (2018) 3895–3900, https://doi.org/10.1039/C8TC00375K.

[136] L. Sun, A. Rotaru, K. Robeyns, Y. Garcia, A colorimetric sensor for the highly selective, ultra-sensitive, and rapid detection of volatile organic compounds and hazardous gases, Ind. Eng. Chem. Res. 60 (2021) 8788–8798, https://doi.org/10.1021/acs.iecr.1c01389.

[137] E. Resines-Urien, E. Fernandez-Bartolome, A. Martinez-Martinez, A. Gamonal, L. Piñeiro-López, J.S. Costa, Vapochromic effect in switchable molecular-based spin crossover compounds, Chem. Soc. Rev. 52 (2023) 705–727, https://doi.org/10.1039/D2CS00790H.

[138] L. Sun, A. Rotaru, Y. Garcia, A non-porous Fe(II) complex for the colorimetric detection of hazardous gases and the monitoring of meat freshness, J. Hazard. Mater. 437 (2022) 129364, https://doi.org/10.1016/j.jhazmat.2022.129364.

[139] D. Gentili, N. Demitri, B. Schäfer, F. Liscio, I. Bergenti, G. Ruani, M. Ruben, M. Cavallini, Multi-modal sensing in spin crossover compounds, J. Mater. Chem. C 3 (2015) 7836–7844, https://doi.org/10.1039/C5TC00845J.

[140] C.M. Jureschi, J. Linares, A. Rotaru, M.H. Ritti, M. Parlier, M.M. Dîrtu, M. Wolff, Y. Garcia, Pressure sensor via optical detection based on a 1D spin transition

coordination polymer, Sensors 15 (2015) 2388–2398, https://doi.org/10.3390/s150202388.

[141] O. Kraieva, C.M. Quintero, I. Suleimanov, E.M. Hernandez, D. Lagrange, L. Salmon, W. Nicolazzi, G. Molnár, C. Bergaud, A. Bousseksou, High spatial resolution imaging of transient thermal events using materials with thermal memory, Small 12 (2016) 6325–6331, https://doi.org/10.1002/smll.201601766.

[142] Y. Eom, K. Kim, H.-J. Lee, S.R. Torati, C. Kim, Development of a temperature sensor using spin-crossover Fe(pyrazine)[Pt(CN)$_4$I] nanoparticles, IEEE Magn. Lett. 13 (2022) 1–5, https://doi.org/10.1109/LMAG.2022.3189274.

[143] G. Molnár, I.A. Gural'skyi, L. Salmon, W. Nicolazzi, C. Quintero, A. Akou, K. Abdul-kader, G. Félix, T. Mahfoud, C. Bergaud, C. Bartual-Murgui, C. Thibault, C. Vieu, A. Bousseksou, Bistable photonic nanostructures based on molecular spin crossover complexes, Proc. SPIE 8425 (2012) 842513, https://doi.org/10.1117/12.921849.

[144] M. Ohba, K. Yoneda, G. Agustí, M.C. Muñoz, A.B. Gaspar, J.A. Real, M. Yamasaki, H. Ando, Y. Nakao, S. Sakaki, S. Kitagawa, Bidirectional chemo-switching of spin state in a microporous framework, Angew. Chem. Int. Ed. 48 (2009) 4767–4771, https://doi.org/10.1002/anie.200806039.

[145] P.D. Southon, L. Liu, E.A. Fellows, D.J. Price, G.J. Halder, K.W. Chapman, B. Moubaraki, K.S. Murray, J.-F. Létard, C.J. Kepert, Dynamic interplay between spin-crossover and host−guest function in a nanoporous metal−organic framework material, J. Am. Chem. Soc. 131 (2009) 10998–11009, https://doi.org/10.1021/ja902187d.

[146] C. Bartual-Murgui, A. Akou, C. Thibault, G. Molnár, C. Vieu, L. Salmon, A. Bousseksou, Spin-crossover metal–organic frameworks: promising materials for designing gas sensors, J. Mater. Chem. C 3 (2015) 1277–1285, https://doi.org/10.1039/C4TC02441A.

[147] L. Kang, R.P. Jenkins, D.H. Werner, Recent progress in active optical metasurfaces, Adv. Opt. Mater. 7 (2019) 1801813, https://doi.org/10.1002/adom.201801813.

[148] J.H. Ko, Y.J. Yoo, Y. Lee, H.-H. Jeong, Y.M. Song, A review of tunable photonics: optically active materials and applications from visible to terahertz, iScience 25 (2022) 104727, https://doi.org/10.1016/j.isci.2022.104727.

[149] U. Efron, Spatial Light Modulator Technology: Materials, Devices and Applications, Marcel Dekker, Inc., New York, 1995.

[150] L.A. Coldren, S.W. Corzine, M.L. Mašanović, Diode Lasers and Photonic Integrated Circuits, John Wiley & Sons, Inc., Hoboken, 2012.

[151] J.-F. Létard, P. Guionneau, L. Goux-Capes, Towards spin crossover applications, in: P. Gütlich, H.A. Goodwin (Eds.), Spin Crossover in Transition Metal Compounds III, Springer, Berlin, Heidelberg, 2004, pp. 221–249, https://doi.org/10.1007/b95429.

[152] OliKrom. https://www.olikrom.com, 2025. (Accessed March 2025).

[153] Gerflor. https://www.gerflor.fr, 2025. (Accessed March 2025).

[154] L. Salmon, L. Catala, Spin-crossover nanoparticles and nanocomposite materials, C. R. Chim. 21 (2018) 1230–1269, https://doi.org/10.1016/j.crci.2018.07.009.

[155] T. Mallah, M. Cavallini, Surfaces, thin films and patterning of spin crossover compounds, C. R. Chim. 21 (2018) 1270–1286, https://doi.org/10.1016/j.crci.2018.02.007.

[156] A. Enriquez-Cabrera, A. Rapakousiou, M. Piedrahita Bello, G. Molnár, L. Salmon, A. Bousseksou, Spin crossover polymer composites, polymers and related soft materials, Coord. Chem. Rev. 419 (2020) 213396, https://doi.org/10.1016/j.ccr.2020.213396.

[157] M.S. Kilic, J. Brehme, J. Pawlak, K. Tran, F.W. Bauer, T. Shiga, T. Suzuki, M. Nihei, R.F. Sindelar, F. Renz, Incorporation and deposition of spin crossover materials into and onto electrospun nanofibers, Polymers 15 (2023) 2365, https://doi.org/10.3390/polym15102365.

[158] A. Günther, Y. Deja, M. Kilic, K. Tran, P. Kotra, F. Renz, W. Kowalsky, B. Roth, Investigation of the molecular switching process between spin crossover states of triazole complexes as basis for optical sensing applications, Sci. Rep. 14 (2024) 5897, https://doi.org/10.1038/s41598-024-56427-1.

[159] K.S. Kumar, M. Ruben, Sublimable spin-crossover complexes: from spin-state switching to molecular devices, Angew. Chem. Int. Ed. 60 (2021) 7502–7521, https://doi.org/10.1002/anie.201911256.

[160] M. Born, E. Wolf, Principles of Optics: Electromagnetic Theory of Propagation, Interference and Diffraction of Light, 7th ed, Cambridge University Press, Cambridge, 1999, https://doi.org/10.1017/CBO9781139644181.

[161] J. Parra, J. Navarro-Arenas, M. Menghini, M. Recaman, J. Pierre-Locquet, P. Sanchis, Low-threshold power and tunable integrated optical limiter based on an ultracompact VO$_2$/Si waveguide, APL Photonics 6 (2021) 121301, https://doi.org/10.1063/5.0071395.

[162] S. Calvez, H. Camon, K. Ridier, G. Molnar, O. Gauthier-Lafaye, Broadband high-contrast visible optical switches based on a spin-crossover material, Appl. Opt. 61 (2022) 9562–9568, https://doi.org/10.1364/AO.473176.

[163] Z. Yang, C. Ko, S. Ramanathan, Oxide electronics utilizing ultrafast metal-insulator transitions, Annu. Rev. Mater. Res. 41 (2011) 337–367, https://doi.org/10.1146/annurev-matsci-062910-100347.

[164] J.D. Ryckman, V. Diez-Blanco, J. Nag, R.E. Marvel, B.K. Choi, R.F. Haglund, S. M. Weiss, Photothermal optical modulation of ultra-compact hybrid Si-VO$_2$ ring resonators, Opt. Express 20 (2012) 13215–13225, https://doi.org/10.1364/OE.20.013215.

[165] M. Rudé, J. Pello, R.E. Simpson, J. Osmond, G. Roelkens, J.J.G.M. van der Tol, V. Pruneri, Optical switching at 1.55 μm in silicon racetrack resonators using phase change materials, Appl. Phys. Lett. 103 (2013) 141119, https://doi.org/10.1063/1.4824714.

[166] A. Karvounis, B. Gholipour, K.F. MacDonald, N.I. Zheludev, All-dielectric phase-change reconfigurable metasurface, Appl. Phys. Lett. 109 (2016) 051103, https://doi.org/10.1063/1.4959272.

[167] M. Stegmaier, C. Rios, H. Bhaskaran, W.H.P. Pernice, Thermo-optical effect in phase-change nanophotonics, ACS Photonics 3 (2016) 828–835, https://doi.org/10.1021/acsphotonics.6b00032.

[168] K.J. Miller, K.A. Hallman, R.F. Haglund, S.M. Weiss, Silicon waveguide optical switch with embedded phase change material, Opt. Express 25 (2017) 26527–26536, https://doi.org/10.1364/OE.25.026527.

[169] K.J. Miller, R.F. Haglund, S.M. Weiss, Optical phase change materials in integrated silicon photonic devices: review, Opt. Mater. Express 8 (2018) 2415–2429, https://doi.org/10.1364/OME.8.002415.

[170] C. Williams, N. Hong, M. Julian, S. Borg, H.J. Kim, Tunable mid-wave infrared Fabry-Perot bandpass filters using phase-change GeSbTe, Opt. Express 28 (2020) 10583–10594, https://doi.org/10.1364/OE.390538.

[171] P. Zuliani, E. Palumbo, M. Borghi, G.D. Libera, R. Annunziata, Engineering of chalcogenide materials for embedded applications of phase change memory, Solid State Electron. 111 (2015) 27–31, https://doi.org/10.1016/j.sse.2015.04.009.

[172] M. Wuttig, H. Bhaskaran, T. Taubner, Phase-change materials for non-volatile photonic applications, Nat. Photonics 11 (2017) 465–476, https://doi.org/10.1038/nphoton.2017.126.

[173] P. Noé, C. Vallée, F. Hippert, F. Fillot, J.-Y. Raty, Phase-change materials for non-volatile memory devices: from technological challenges to materials science issues, Semicond. Sci. Technol. 33 (2018) 013002, https://doi.org/10.1088/1361-6641/aa7c25.

[174] H. Liu, J. Lu, X.R. Wang, Metamaterials based on the phase transition of VO$_2$, Nanotechnology 29 (2018) 024002, https://doi.org/10.1088/1361-6528/aa9cb1.

[175] J.J. Seoane, J. Parra, J. Navarro-Arenas, M. Recaman, K. Schouteden, J. P. Locquet, P. Sanchis, Ultra-high endurance silicon photonic memory using vanadium dioxide, npj Nanophotonics 1 (2024) 37, https://doi.org/10.1038/s44310-024-00038-1.

[176] Z. Gong, F. Yang, L. Wang, R. Chen, J. Wu, C.P. Grigoropoulos, J. Yao, Phase change materials in photonic devices, J. Appl. Phys. 129 (2021) 030902, https://doi.org/10.1063/5.0027868.

[177] P. Prabhathan, K.V. Sreekanth, J. Teng, J.H. Ko, Y.J. Yoo, H.-H. Jeong, Y. Lee, S. Zhang, T. Cao, C.-C. Popescu, B. Mills, T. Gu, Z. Fang, R. Chen, H. Tong, Y. Wang, Q. He, Y. Lu, Z. Liu, H. Yu, A. Mandal, Y. Cui, A.S. Ansari, V. Bhingardive, M. Kang, C.K. Lai, M. Merklein, M.J. Müller, Y.M. Song, Z. Tian, J. Hu, M. Losurdo, A. Majumdar, X. Miao, X. Chen, B. Gholipour, K.A. Richardson, B.J. Eggleton, M. Wuttig, R. Singh, Roadmap for phase change materials in photonics and beyond, iScience 26 (2023) 107946, https://doi.org/10.1016/j.isci.2023.107946.

[178] R.E. Simpson, J.K.W. Yang, J. Hu, Are phase change materials ideal for programmable photonics?: opinion, Opt. Mater. Express 12 (2022) 2368–2373, https://doi.org/10.1364/OME.456895.

[179] J.B. Kana Kana, J.M. Ndjaka, G. Vignaud, A. Gibaud, M. Maaza, Thermally tunable optical constants of vanadium dioxide thin films measured by spectroscopic ellipsometry, Opt. Commun. 284 (2011) 807–812, https://doi.org/10.1016/j.optcom.2010.10.009.

[180] J. Zheng, A. Khanolkar, P. Xu, S. Colburn, S. Deshmukh, J. Myers, J. Frantz, E. Pop, J. Hendrickson, J. Doylend, N. Boechler, A. Majumdar, GST-on-silicon hybrid nanophotonic integrated circuits: a non-volatile quasi-continuously reprogrammable platform, Opt. Mater. Express 8 (2018) 1551–1561, https://doi.org/10.1364/OME.8.001551.

[181] J. Leroy, A. Crunteanu, A. Bessaudou, F. Cosset, C. Champeaux, J.-C. Orlianges, High-speed metal-insulator transition in vanadium dioxide films induced by an electrical pulsed voltage over nano-gap electrodes, Appl. Phys. Lett. 100 (2012) 213507, https://doi.org/10.1063/1.4721520.

[182] P. Guo, J.A. Burrow, G.A. Sevison, H. Kwon, C. Perez, J.R. Hendrickson, E. M. Smith, M. Asheghi, K.E. Goodson, I. Agha, A.M. Sarangan, Tungsten-doped Ge$_2$Sb$_2$Te$_5$ phase change material for high-speed optical switching devices, Appl. Phys. Lett. 116 (2020) 131901, https://doi.org/10.1063/1.5142552.

[183] J. Sarkar, B. Gleixner, Evolution of phase change memory characteristics with operating cycles: electrical characterization and physical modeling, Appl. Phys. Lett. 91 (2007) 233506, https://doi.org/10.1063/1.2821845.

[184] Q. Zhang, Y. Zhang, J. Li, R. Soref, T. Gu, J. Hu, Broadband nonvolatile photonic switching based on optical phase change materials: beyond the classical figure-of-merit, Opt. Lett. 43 (2018) 94–97, https://doi.org/10.1364/OL.43.000094.

[185] Y. Zhang, J.B. Chou, J. Li, H. Li, Q. Du, A. Yadav, S. Zhou, M.Y. Shalaginov, Z. Fang, H. Zhong, C. Roberts, P. Robinson, B. Bohlin, C. Ríos, H. Lin, M. Kang, T. Gu, J. Warner, V. Liberman, K. Richardson, J. Hu, Broadband transparent optical phase change materials for high-performance nonvolatile photonics, Nat. Commun. 10 (2019) 4279, https://doi.org/10.1038/s41467-019-12196-4.

[186] W. Dong, H. Liu, J.K. Behera, L. Lu, R.J.H. Ng, K.V. Sreekanth, X. Zhou, J.K. W. Yang, R.E. Simpson, Wide bandgap phase change material tuned visible photonics, Adv. Funct. Mater. 29 (2019) 1806181, https://doi.org/10.1002/adfm.201806181.

[187] M. Delaney, I. Zeimpekis, D. Lawson, D.W. Hewak, O.L. Muskens, A new family of ultralow loss reversible phase-change materials for photonic integrated circuits: Sb$_2$S$_3$ and Sb$_2$Se$_3$, Adv. Funct. Mater. 30 (2020) 2002447, https://doi.org/10.1002/adfm.202002447.

[188] R. Hauffe, K. Petermann, Thermo-optic switching, in: T.S. El-Bawab (Ed.), Optical Switching, Springer, Boston, 2006, pp. 111–139, https://doi.org/10.1007/0-387-29159-8_4.

[189] G. Coppola, L. Sirleto, I. Rendina, M. Iodice, Advance in thermo-optical switches: principles, materials, design, and device structure, Opt. Eng. 50 (2011) 071112, https://doi.org/10.1117/1.3574378.

[190] J. Parra, J. Navarro-Arenas, P. Sanchis, Silicon thermo-optic phase shifters: a review of configurations and optimization strategies, Adv. Photonics Nexus 3 (2024) 044001, https://doi.org/10.1117/1.APN.3.4.044001.

[191] N.C. Harris, Y. Ma, J. Mower, T. Baehr-Jones, D. Englund, M. Hochberg, C. Galland, Efficient, compact and low loss thermo-optic phase shifter in silicon, Opt. Express 22 (2014) 10487–10493, https://doi.org/10.1364/OE.22.010487.

[192] K. Hirai, J.A. Hutchison, H. Uji-i, Molecular chemistry in cavity strong coupling, Chem. Rev. 123 (2023) 8099–8126, https://doi.org/10.1021/acs.chemrev.2c00748.

[193] E.M. Purcell, Spontaneous emission probabilities at radio frequencies, Phys. Rev. 69 (1946) 681, https://doi.org/10.1103/PhysRev.69.674.2.

[194] T.W. Ebbesen, Hybrid light–matter states in a molecular and material science perspective, Acc. Chem. Res. 49 (2016) 2403–2412, https://doi.org/10.1021/acs.accounts.6b00295.

[195] R.F. Ribeiro, L.A. Martínez-Martínez, M. Du, J. Campos-Gonzalez-Angulo, J. Yuen-Zhou, Polariton chemistry: controlling molecular dynamics with optical cavities, Chem. Sci. 9 (2018) 6325–6339, https://doi.org/10.1039/C8SC01043A.

[196] D.S. Dovzhenko, S.V. Ryabchuk, Y.P. Rakovich, I.R. Nabiev, Light–matter interaction in the strong coupling regime: configurations, conditions, and applications, Nanoscale 10 (2018) 3589–3605, https://doi.org/10.1039/C7NR06917K.

[197] M. Hertzog, M. Wang, J. Mony, K. Börjesson, Strong light–matter interactions: a new direction within chemistry, Chem. Soc. Rev. 48 (2019) 937–961, https://doi.org/10.1039/C8CS00193F.

[198] F.J. Garcia-Vidal, C. Ciuti, T.W. Ebbesen, Manipulating matter by strong coupling to vacuum fields, Science 373 (2021) eabd0336, https://doi.org/10.1126/science.abd0336.

[199] K. Nagarajan, A. Thomas, T.W. Ebbesen, Chemistry under vibrational strong coupling, J. Am. Chem. Soc. 143 (2021) 16877–16889, https://doi.org/10.1021/jacs.1c07420.

[200] T.W. Ebbesen, A. Rubio, G.D. Scholes, Introduction: polaritonic chemistry, Chem. Rev. 123 (2023) 12037–12038, https://doi.org/10.1021/acs.chemrev.3c00637.

[201] P.A. Thomas, W.J. Tan, H.A. Fernandez, W.L. Barnes, A new signature for strong light–matter coupling using spectroscopic ellipsometry, Nano Lett. 20 (2020) 6412–6419, https://doi.org/10.1021/acs.nanolett.0c01963.

[202] C. Weisbuch, M. Nishioka, A. Ishikawa, Y. Arakawa, Observation of the coupled exciton-photon mode splitting in a semiconductor quantum microcavity, Phys. Rev. Lett. 69 (1992) 3314–3317, https://doi.org/10.1103/PhysRevLett.69.3314.

[203] R. Houdré, C. Weisbuch, R.P. Stanley, U. Oesterle, P. Pellandini, M. Ilegems, Measurement of cavity-polariton dispersion curve from angle resolved photoluminescence experiments, Phys. Rev. Lett. 73 (1994) 2043–2046, https://doi.org/10.1103/physrevlett.73.2043.

[204] T. Schwartz, J.A. Hutchison, C. Genet, T.W. Ebbesen, Reversible switching of ultrastrong light-molecule coupling, Phys. Rev. Lett. 106 (2011) 196405, https://doi.org/10.1103/PhysRevLett.106.196405.

[205] S. Kéna-Cohen, S.A. Maier, D.D.C. Bradley, Ultrastrongly coupled exciton–polaritons in metal-clad organic semiconductor microcavities, Adv. Opt. Mater. 1 (2013) 827–833, https://doi.org/10.1002/adom.201300256.

[206] S. Gambino, M. Mazzeo, A. Genco, O. Di Stefano, S. Savasta, S. Patanè, D. Ballarini, F. Mangione, G. Lerario, D. Sanvitto, G. Gigli, Exploring light–matter interaction phenomena under ultrastrong coupling regime, ACS Photonics 1 (2014) 1042–1048, https://doi.org/10.1021/ph500266d.

[207] J.A. Hutchison, T. Schwartz, C. Genet, E. Devaux, T.W. Ebbesen, Modifying chemical landscapes by coupling to vacuum fields, Angew. Chem. Int. Ed. 51 (2012) 1592–1596, https://doi.org/10.1002/anie.201107033.

[208] B. Munkhbat, M. Wersäll, D.G. Baranov, T.J. Antosiewicz, T. Shegai, Suppression of photo-oxidation of organic chromophores by strong coupling to plasmonic nanoantennas, Sci. Adv. 4 (2018) eaas9552, https://doi.org/10.1126/sciadv.aas9552.

[209] V.N. Peters, M.O. Faruk, J. Asane, R. Alexander, D.A. Peters, S. Prayakarao, S. Rout, M.A. Noginov, Effect of strong coupling on photodegradation of the semiconducting polymer P3HT, Optica 6 (2019) 318–325, https://doi.org/10.1364/OPTICA.6.000318.

[210] J. Mony, C. Climent, A.U. Petersen, K. Moth-Poulsen, J. Feist, K. Börjesson, Photoisomerization efficiency of a solar thermal fuel in the strong coupling regime, Adv. Funct. Mater. 31 (2021) 2010737, https://doi.org/10.1002/adfm.202010737.

[211] C. Ciuti, G. Bastard, I. Carusotto, Quantum vacuum properties of the intersubband cavity polariton field, Phys. Rev. B 72 (2005) 115303, https://doi.org/10.1103/PhysRevB.72.115303.

[212] J. Galego, F.J. Garcia-Vidal, J. Feist, Cavity-induced modifications of molecular structure in the strong-coupling regime, Phys. Rev. X 5 (2015) 041022, https://doi.org/10.1103/PhysRevX.5.041022.

[213] L. Zhang, K. Ridier, O.Ye. Horniichuk, S. Calvez, L. Salmon, G. Molnár, A. Bousseksou, Reversible switching of strong light–matter coupling using spin-crossover molecular materials, J. Phys. Chem. Lett. 14 (2023) 6840–6849, https://doi.org/10.1021/acs.jpclett.3c01136.

[214] J.A. Ćwik, P. Kirton, S. De Liberato, J. Keeling, Excitonic spectral features in strongly coupled organic polaritons, Phys. Rev. A 93 (2016) 033840, https://doi.org/10.1103/PhysRevA.93.033840.

[215] L.A. Martínez-Martínez, R.F. Ribeiro, J. Campos-González-Angulo, J. Yuen-Zhou, Can ultrastrong coupling change ground-state chemical reactions? ACS Photonics 5 (2018) 167–176, https://doi.org/10.1021/acsphotonics.7b00610.

[216] A. Hoblos, S. Calvez, L. Salmon, G. Molnár, K. Ridier, A. Bousseksou, Does electronic strong light-matter coupling affect the ground-state energy landscape? An experimental study using spin-crossover molecules, J. Phys. Chem. C 129 (2025) 3107–3117, https://doi.org/10.1021/acs.jpcc.4c08198.

[217] B.S. Simpkins, A.D. Dunkelberger, I. Vurgaftman, Control, modulation, and analytical descriptions of vibrational strong coupling, Chem. Rev. 123 (2023) 5020–5048, https://doi.org/10.1021/acs.chemrev.2c00774.

[218] A. Thomas, J. George, A. Shalabney, M. Dryzhakov, S.J. Varma, J. Moran, T. Chervy, X. Zhong, E. Devaux, C. Genet, J.A. Hutchison, T.W. Ebbesen, Ground-state chemical reactivity under vibrational coupling to the vacuum electromagnetic field, Angew. Chem. Int. Ed. 55 (2016) 11462–11466, https://doi.org/10.1002/anie.201605504.

[219] A. Thomas, L. Lethuillier-Karl, K. Nagarajan, R.M.A. Vergauwe, J. George, T. Chervy, A. Shalabney, E. Devaux, C. Genet, J. Moran, T.W. Ebbesen, Tilting a ground-state reactivity landscape by vibrational strong coupling, Science 363 (2019) 615–619, https://doi.org/10.1126/science.aau7742.

[220] J. Lather, P. Bhatt, A. Thomas, T.W. Ebbesen, J. George, Cavity catalysis by cooperative vibrational strong coupling of reactant and solvent molecules, Angew. Chem. Int. Ed. 58 (2019) 10635–10638, https://doi.org/10.1002/anie.201905407.

[221] R.M.A. Vergauwe, A. Thomas, K. Nagarajan, A. Shalabney, J. George, T. Chervy, M. Seidel, E. Devaux, V. Torbeev, T.W. Ebbesen, Modification of enzyme activity by vibrational strong coupling of water, Angew. Chem. Int. Ed. 58 (2019) 15324–15328, https://doi.org/10.1002/anie.201908876.

[222] B.S. Simpkins, A.D. Dunkelberger, J.C. Owrutsky, Mode-specific chemistry through vibrational strong coupling (or a wish come true), J. Phys. Chem. C 125 (2021) 19081–19087, https://doi.org/10.1021/acs.jpcc.1c05362.

[223] W. Ahn, J.F. Triana, F. Recabal, F. Herrera, B.S. Simpkins, Modification of ground-state chemical reactivity via light–matter coherence in infrared cavities, Science 380 (2023) 1165–1168, https://doi.org/10.1126/science.ade7147.

[224] C. Climent, J. Galego, F.J. Garcia-Vidal, J. Feist, Plasmonic nanocavities enable self-induced electrostatic catalysis, Angew. Chem. Int. Ed. 58 (2019) 8698–8702, https://doi.org/10.1002/anie.201901926.

[225] S. Decurtins, P. Gütlich, K.M. Hasselbach, A. Hauser, H. Spiering, Light-induced excited-spin-state trapping in iron(II) spin-crossover systems. Optical spectroscopic and magnetic susceptibility study, Inorg. Chem. 24 (1985) 2174–2178, https://doi.org/10.1021/ic00208a013.

[226] G. Chastanet, M. Lorenc, R. Bertoni, C. Desplanches, Light-induced spin crossover—solution and solid-state processes, C. R. Chim. 21 (2018) 1075–1094, https://doi.org/10.1016/j.crci.2018.02.011.

[227] M. Chergui, E. Collet, Photoinduced structural dynamics of molecular systems mapped by time-resolved X-ray methods, Chem. Rev. 117 (2017) 11025–11065, https://doi.org/10.1021/acs.chemrev.6b00831.

[228] J.E. Monat, J.K. McCusker, Femtosecond excited-state dynamics of an iron(II) polypyridyl solar cell sensitizer model, J. Am. Chem. Soc. 122 (2000) 4092–4097, https://doi.org/10.1021/ja992436o.

[229] Ch. Bressler, C. Milne, V.-T. Pham, A. ElNahhas, R.M. van der Veen, W. Gawelda, S. Johnson, P. Beaud, D. Grolimund, M. Kaiser, C.N. Borca, G. Ingold, R. Abela, M. Chergui, Femtosecond XANES study of the light-induced spin crossover dynamics in an iron(II) complex, Science 323 (2009) 489–492, https://doi.org/10.1126/science.1165733.

[230] N. Huse, H. Cho, K. Hong, L. Jamula, F.M.F. de Groot, T.K. Kim, J.K. McCusker, R. W. Schoenlein, Femtosecond soft X-ray spectroscopy of solvated transition-metal complexes: deciphering the interplay of electronic and structural dynamics, J. Phys. Chem. Lett. 2 (2011) 880–884, https://doi.org/10.1021/jz200168m.

[231] G. Auböck, M. Chergui, Sub-50-fs photoinduced spin crossover in $[Fe(bpy)_3]^{2+}$, Nat. Chem. 7 (2015) 629–633, https://doi.org/10.1038/nchem.2305.

[232] C. Enachescu, U. Oetliker, A. Hauser, Photoexcitation in the spin-crossover compound $[Fe(pic)_3]Cl_2{\cdot}EtOH$ (pic = 2-picolylamine), J. Phys. Chem. B 106 (2002) 9540–9545, https://doi.org/10.1021/jp020765o.

[233] M. Van Veenendaal, J. Chang, A.J. Fedro, Model of ultrafast intersystem crossing in photoexcited transition-metal organic compounds, Phys. Rev. Lett. 104 (2010) 067401, https://doi.org/10.1103/PhysRevLett.104.067401.

[234] J. Chang, A.J. Fedro, M. Van Veenendaal, Ultrafast cascading theory of intersystem crossings in transition-metal complexes, Phys. Rev. B 82 (2010) 075124, https://doi.org/10.1103/PhysRevB.82.075124.

[235] A. Hauser, Reversibility of light-induced excited spin state trapping in the Fe $(ptz)_6(BF_4)_2$, and the $Zn_{1-x}Fe_x(ptz)_6(BF_4)_2$ spin-crossover systems, Chem. Phys. Lett. 124 (1986) 543–548, https://doi.org/10.1016/0009-2614(86)85073-4.

[236] A. Marino, P. Chakraborty, M. Servol, M. Lorenc, E. Collet, A. Hauser, The role of ligand-field states in the ultrafast photophysical cycle of the prototypical iron(II) spin-crossover compound $[Fe(ptz)_6](BF_4)_2$, Angew. Chem. Int. Ed. 53 (2014) 3863–3867, https://doi.org/10.1002/anie.201310884.

[237] R. Bertoni, E. Collet, H. Cailleau, M.-L. Boillot, A. Tissot, J. Laisney, C. Enachescu, M. Lorenc, Temperature dependence of the cooperative out-of-equilibrium elastic switching in a spin-crossover material, Phys. Chem. Chem. Phys. 21 (2019) 6606–6612, https://doi.org/10.1039/C8CP07074A.

[238] A. Volte, C. Mariette, R. Bertoni, M. Cammarata, X. Dong, E. Trzop, H. Cailleau, E. Collet, M. Levantino, M. Wulff, J. Kubicki, F.-L. Yang, M.-L. Boillot, B. Corraze, L. Stoleriu, C. Enachescu, M. Lorenc, Dynamical limits for the molecular switching in a photoexcited material revealed by X-ray diffraction, Commun. Phys. 5 (2022) 168, https://doi.org/10.1038/s42005-022-00940-0.

[239] K. Ridier, R. Bertoni, R. Mandal, A. Volte, Y. Jiang, E. Trzop, M. Levantino, Y. Watier, J. Frey, Y. Zhang, T. Pezeril, H. Cailleau, G. Molnár, A. Bousseksou, M. Lorenc, C. Mariette, Temporal separation between lattice dynamics and electronic spin-state switching in spin-crossover thin films evidenced by time-

resolved X-ray diffraction, Adv. Funct. Mater. 34 (2024) 2403585, https://doi.org/10.1002/adfm.202403585.

[240] D. Vinci, K. Ridier, F. Qi, F. Ardana-Lamas, P. Zalden, L.C. Liu, T. Eklund, M. S. Jakobsen, R. Schubert, D. Khakhulin, C. Deiter, N. Bottin, H. Yousef, D. von Stetten, P. Łaski, R. Kamiński, K.N. Jarzembska, R.F. Wallick, T. Stensitzki, R. M. van der Veen, H.M. Müller-Werkmeister, G. Molnár, D. Xiang, C. Milne, M. Lorenc, Y. Jiang, Capturing ultrafast molecular motions and lattice dynamics in spin crossover film using femtosecond diffraction methods, Nat. Commun. 16 (2025) 2043, https://doi.org/10.1038/s41467-025-57202-0.

[241] H. Cailleau, M. Lorenc, L. Guérin, M. Servol, E. Collet, M. Buron-Le Cointe, Structural dynamics of photoinduced molecular switching in the solid state, Acta Crystallogr. A66 (2010) 189–197, https://doi.org/10.1107/S0108767309051046.

[242] R. Bertoni, M. Lorenc, H. Cailleau, A. Tissot, J. Laisney, M.-L. Boillot, L. Stoleriu, A. Stancu, C. Enachescu, E. Collet, Elastically driven cooperative response of a molecular material impacted by a laser pulse, Nat. Mater. 15 (2016) 606–610, https://doi.org/10.1038/nmat4606.

[243] G. Galle, J. Degert, C. Mauriac, C. Etrillard, J.F. Letard, E. Freysz, Nanosecond study of spin state transition induced by a single nanosecond laser shot on [Fe(NH_2trz)$_3$] compounds inside and outside their thermal hysteresis loops, Chem. Phys. Lett. 500 (2010) 18–22, https://doi.org/10.1016/j.cplett.2010.09.059.

[244] G. Gallé, D. Deldicque, J. Degert, Th. Forestier, J.-F. Létard, E. Freysz, Room temperature study of the optical switching of a spin crossover compound inside its thermal hysteresis loop, Appl. Phys. Lett. 96 (2010) 041907, https://doi.org/10.1063/1.3294312.

[245] L. Stoleriu, M. Nishino, S. Miyashita, A. Stancu, R. Bertoni, E. Collet, M. Lorenc, C. Enachescu, Multiscale out-of-equilibrium dynamics driven by pulsed laser excitation in spin-crossover materials: a combined thermoelastic and mechanoelastic study, Phys. Rev. B 108 (2023) 014306, https://doi.org/10.1103/PhysRevB.108.014306.

[246] M. Reinhard, K. Kunnus, K. Ledbetter, E. Biasin, D.B. Zederkof, R. Alonso-Mori, T. B. van Driel, S. Nelson, M. Kozina, O.J. Borkiewicz, M. Lorenc, M. Cammarata, E. Collet, D. Sokaras, A.A. Cordones, K.J. Gaffney, Observation of a picosecond light-induced spin transition in polymeric nanorods, ACS Nano 18 (2024) 15468–15476, https://doi.org/10.1021/acsnano.3c10042.

[247] E. Freysz, S. Montant, S. Létard, J.-F. Létard, Single laser pulse induces spin state transition within the hysteresis loop of an iron compound, Chem. Phys. Lett. 394 (2004) 318–323, https://doi.org/10.1016/j.cplett.2004.07.017.

[248] S. Bonhommeau, G. Molnár, A. Galet, A. Zwick, J.-A. Real, J.J. McGarvey, A. Bousseksou, One shot laser pulse induced reversible spin transition in the spin-crossover complex [Fe($C_4H_4N_2$){Pt(CN)$_4$}] at room temperature, Angew. Chem. Int. Ed. 44 (2005) 4069–4073, https://doi.org/10.1002/anie.200500717.

[249] S. Cobo, D. Ostrovskii, S. Bonhommeau, L. Vendier, G. Molnár, L. Salmon, K. Tanaka, A. Bousseksou, Single-laser-shot-induced complete bidirectional spin transition at room temperature in single crystals of (Fe^{II}(pyrazine)(Pt(CN)$_4$)), J. Am. Chem. Soc. 130 (2008) 9019–9024, https://doi.org/10.1021/ja800878f.

[250] O. Fouché, J. Degert, G. Jonusauskas, N. Daro, J.-F. Létard, E. Freysz, Mechanism for optical switching of the spin crossover [Fe(NH_2-trz)$_3$](Br)$_2$·3H_2O compound at room temperature, Phys. Chem. Chem. Phys. 12 (2010) 3044–3052, https://doi.org/10.1039/B921984F.

[251] G. Gallé, C. Etrillard, J. Degert, F. Guillaume, J.-F. Létard, E. Freysz, Study of the fast photoswitching of spin crossover nanoparticles outside and inside their thermal hysteresis loop, Appl. Phys. Lett. 102 (2013) 063302, https://doi.org/10.1063/1.4792527.

[252] M. Castro, O. Roubeau, L. Piñeiro-López, J.A. Real, J.A. Rodríguez-Velamazán, Pulsed-laser switching in the bistability domain of a cooperative spin crossover compound: a critical study through calorimetry, J. Phys. Chem. C 119 (2015) 17334–17343, https://doi.org/10.1021/acs.jpcc.5b05864.

[253] E. Collet, L. Henry, L. Piñeiro-López, L. Toupet, J.A. Real, Single laser shot spin state switching of {Fe^{II}(pz)[Pt(CN)$_4$]} inside thermal hysteresis studied by X-ray diffraction, Curr. Inorg. Chem. 6 (2016) 61–66, https://doi.org/10.2174/1877944105666150910233704.

[254] E. Coronado, J.R. Galán-Mascarós, M. Monrabal-Capilla, J. García-Martínez, P. Pardo-Ibáñez, Bistable spin-crossover nanoparticles showing magnetic thermal hysteresis near room temperature, Adv. Mater. 19 (2007) 1359–1361, https://doi.org/10.1002/adma.200700559.

[255] K.-P. Xie, Z.-Y. Ruan, B.-H. Lyu, X.-X. Chen, X.-W. Zhang, G.-Z. Huang, Y.-C. Chen, Z.-P. Ni, M.-L. Tong, Guest-driven light-induced spin change in an azobenzene loaded metal–organic framework, Angew. Chem. Int. Ed. 60 (2021) 27144–27150, https://doi.org/10.1002/anie.202113294.

[256] C. Roux, J. Zarembowitch, B. Gallois, T. Granier, R. Claude, Toward ligand-driven light-induced spin changing. Influence of the configuration of 4 styrylpyridine (stpy) on the magnetic properties of Fe^{II}(stpy)$_4$(NCS)$_2$ complexes. Crystal structures of the spin-crossover species Fe(trans-stpy)$_4$(NCS)$_2$ and of the high-spin species Fe(cis-stpy)$_4$(NCS)$_2$, Inorg. Chem. 33 (1994) 2273–2279, https://doi.org/10.1021/ic00088a033.

[257] M.-L. Boillot, A. Sour, P. Delhaès, C. Mingotaud, H. Soyer, A photomagnetic effect for controlling spin states of iron(II) complexes in molecular materials, Coord. Chem. Rev. 190–192 (1999) 47–59, https://doi.org/10.1016/S0010-8545(99)00064-8.

[258] M.-L. Boillot, J. Zarembowitch, A. Sour, Ligand-driven light-induced spin change (LD-LISC): a promising photomagnetic effect, in: P. Gütlich, H.A. Goodwin (Eds.), Spin Crossover in Transition Metal Compounds II, Springer, Berlin, Heidelberg, 2004, pp. 261–276, https://doi.org/10.1007/b95419.

[259] S. Thies, C. Bornholdt, F. Köhler, F.D. Sönnichsen, C. Näther, F. Tuczek, R. Herges, Coordination-induced spin crossover (CISCO) through axial bonding of substituted pyridines to nickel–porphyrins: σ-donor versus π-acceptor effects, Chem. Eur. J. 16 (2010) 10074–10083, https://doi.org/10.1002/chem.201000603.

[260] S. Venkataramani, U. Jana, M. Dommaschk, F.D. Sönnichsen, F. Tuczek, R. Herges, Magnetic bistability of molecules in homogeneous solution at room temperature, Science 331 (2011) 445–448, https://doi.org/10.1126/science.1201180.

[261] M. Dommaschk, F. Gutzeit, S. Boretius, R. Haag, R. Herges, Coordination-induced spin-state-switch (CISSS) in water, Chem. Commun. 50 (2014) 12476–12478, https://doi.org/10.1039/C4CC05525J.

[262] A. Köbke, F. Gutzeit, F. Röhricht, A. Schlimm, J. Grunwald, F. Tuczek, M. Studniarek, D. Longo, F. Choueikani, E. Otero, P. Ohresser, S. Rohlf, S. Johannsen, F. Diekmann, K. Rossnagel, A. Weismann, T. Jasper-Toennies, C. Näther, R. Herges, R. Berndt, M. Gruber, Reversible coordination-induced spin-state switching in complexes on metal surfaces, Nat. Nanotechnol. 15 (2020) 18–21, https://doi.org/10.1038/s41565-019-0594-8.

[263] Y. Hasegawa, K. Takahashi, S. Kume, H. Nishihara, Complete solid state photoisomerization of bis(dipyrazolylstyrylpyridine)iron(II) to change magnetic properties, Chem. Commun. 47 (2011) 6846–6848, https://doi.org/10.1039/C1CC11850A.

[264] K. Takahashi, Y. Hasegawa, R. Sakamoto, M. Nishikawa, S. Kume, E. Nishibori, H. Nishihara, Solid-state ligand-driven light-induced spin change at ambient temperatures in bis(dipyrazolylstyrylpyridine)iron(II) complexes, Inorg. Chem. 51 (2012) 5188–5198, https://doi.org/10.1021/ic300030b.

[265] A.B. Gaspar, V. Ksenofontov, M. Seredyuk, P. Gütlich, Multifunctionality in spin crossover materials, Coord. Chem. Rev. 249 (2005) 2661–2676, https://doi.org/10.1016/j.ccr.2005.04.028.

[266] O. Sato, Z.-Y. Li, Z.-S. Yao, S. Kang, S. Kanegawa, Multifunctional materials combining spin-crossover with conductivity and magnetic ordering, in: M. A. Halcrow (Ed.), Spin-Crossover Materials: Properties and Applications, John Wiley & Sons, Ltd., Leeds, 2013, pp. 303–319, https://doi.org/10.1002/9781118519301.ch11.

[267] O. Sato, Optically switchable molecular solids: photoinduced spin-crossover, photochromism, and photoinduced magnetization, Acc. Chem. Res. 36 (2003) 692–700, https://doi.org/10.1021/ar020242z.

[268] J.J. Zakrzewski, M. Liberka, J. Wang, S. Chorazy, S. Ohkoshi, Optical phenomena in molecule-based magnetic materials, Chem. Rev. 124 (2024) 5930–6050, https://doi.org/10.1021/acs.chemrev.3c00840.